PolyPublie
Polytechnique Montréal

POLYTECHNIQUE MONTRÉAL
UNIVERSITÉ D'INGÉNIERIE

Titre: Title:	Two-phase flow pattern identification from fluctuating signals of pressure and void fraction
Auteur: Author:	Yanjie Han
Date:	1999
Type:	Mémoire ou thèse / Dissertation or Thesis
Référence: Citation:	Han, Y. (1999). Two-phase flow pattern identification from fluctuating signals of pressure and void fraction [Mémoire de maîtrise, École Polytechnique de Montréal]. PolyPublie. https://publications.polymtl.ca/8780/

Document en libre accès dans PolyPublie
Open Access document in PolyPublie

URL de PolyPublie: PolyPublie URL:	https://publications.polymtl.ca/8780/
Directeurs de recherche: Advisors:	Alberto Teyssedou
Programme: Program:	Non spécifié

Ce fichier a été téléchargé à partir de PolyPublie, le dépôt institutionnel de Polytechnique Montréal
This file has been downloaded from PolyPublie, the institutional repository of Polytechnique Montréal

https://publications.polymtl.ca

UNIVERSITÉ DE MONTRÉAL

TWO–PHASE FLOW PATTERN IDENTIFICATION FROM FLUCTUATING SIGNALS OF PRESSURE AND VOID FRACTION

YANJIE HAN
DÉPARTEMENT DE GÉNIE MÉCANIQUE
ÉCOLE POLYTECHNIQUE DE MONTRÉAL

MÉMOIRE PRÉSENTÉ EN VUE DE L'OBTENTION
DU DIPLÔME DE MAÎTRISE ÈS SCIENCES APPLIQUÉES
(GÉNIE ÉNERGETIQUE)
AVRIL 1999

© Yanjie Han, 1999.

National Library of Canada
Acquisitions and Bibliographic Services
395 Wellington Street
Ottawa ON K1A 0N4
Canada

Bibliothèque nationale du Canada
Acquisitions et services bibliographiques
395, rue Wellington
Ottawa ON K1A 0N4
Canada

Your file Votre référence

Our file Notre référence

The author has granted a non-exclusive licence allowing the National Library of Canada to reproduce, loan, distribute or sell copies of this thesis in microform, paper or electronic formats.

L'auteur a accordé une licence non exclusive permettant à la Bibliothèque nationale du Canada de reproduire, prêter, distribuer ou vendre des copies de cette thèse sous la forme de microfiche/film, de reproduction sur papier ou sur format électronique.

The author retains ownership of the copyright in this thesis. Neither the thesis nor substantial extracts from it may be printed or otherwise reproduced without the author's permission.

L'auteur conserve la propriété du droit d'auteur qui protège cette thèse. Ni la thèse ni des extraits substantiels de celle-ci ne doivent être imprimés ou autrement reproduits sans son autorisation.

0-612-48853-5

Canada

UNIVERSITÉ DE MONTRÉAL

ÉCOLE POLYTECHNIQUE DE MONTRÉAL

Ce mémoire intitulé:

TWO–PHASE FLOW PATTERN IDENTIFICATION FROM FLUCTUATING SIGNALS OF PRESSURE AND VOID FRACTION

présenté par: HAN Yanjie

en vue de l'obtention du diplôme de: Maîtrise ès sciences appliquées

a été dûment accepté par le jury d'examen constitué de:

M.NGUYEN, Hung, Ph.D., président

M.TEYSSEDOU Alberto, Ph.D., membre et directeur de recherche

M.TAPUCU Altan, D.Sc.A., membre

To my family, for their love, caring and support all these years.

To my future, for what the effort is meant to be.

Acknowledgements

The author is greatly indebted to her research advisor Dr. A. Tesseydou for his professional guidance and insight into the work. This memoire could not have been completed without his encouragement, understanding and patience. Sincere appreciation to the members of my jury, Dr. A. Tapucu and Dr. H. Nguyen, for their interest and review of this thesis. Sincere gratitude to Dr. P. Tye who patiently answered lots of computer related questions and for his work in correcting the English. Special thanks to N. Troche for the help in data acquisition programming and P. Hernu for the assistance in carring out the experiments and in translating the summary of the thesis into French. Special thanks to the technical staff J. C. Juneau and P. Champagne for their efforts to solve the laboratory problems which arose time to time at the experimental stage. Special thanks to Chinese Embassy in Canada for providing the tuition exemption to surpport the author's study.

Résumé

Cette thèse présente les résultats expérimentaux utilisés afin de déterminer les types d'écoulement diphasiques dans une section d'essai carrée contenant un mélange air-eau à des conditions atmosphériques. Les paramètres importants, i.e. débits d'entrée, fractions de vide axiales et pressions, sont mesurés simultanément. Les fractions de vide sont mesurées à l'aide de 10 paires d'électrodes en argent. La différence de pression est mesurée grâce à un transmetteur de pression "Validyne". La pression absolue au centre de la section d'essai est aussi mesurée à l'aide d'un transmetteur de pression "Sensotec" dans le but de déterminer la vitesse superficielle locale de la phase gazeuse. Les lectures de tous les instruments mentionnés précédemment sont prises par un système d'acquisition de données avec un temps d'échantillonnage de 15 ms.

Les composantes fluctuantes des signaux de fraction de vide sont analysées en utilisant leur PDF (Probability Density Functions). Pour les écoulements à bulles et annulaires, les PDF montrent une distribution "unimodale" à maximum unique. Le maximum apparaît à faible fraction de vide pour les écoulements à bulles et à haute fraction de vide pour les

écoulements annulaires. Les distributions "bimodales" à deux maxima dominent les régimes d'écoulement de types "par bouchons" et "par écume", avec les maxima qui s'inversent horizontalement durant la transition de l'écoulement par bouchons à celui par écume. Le fait que la distribution unimodale pour les écoulements à bulles et annulaire peut être facilement distinguée de la distribution bimodale observée pour les autres régimes est utilisé pour construire une nouvelle représentation des types d'écoulements diphasiques.

Les moments statistiques sont utilisés comme outil auxiliaire pour l'identification des types d'écoulement. Pour les deux signaux de fraction de vide et de pression, un changement significatif est observé près des zones de transition d'écoulement de "bulles" à "bouchons" et de "par écume" à "annulaire". L'asymétrie est faible pour les écoulements à bulles et, en général, sa valeur est négative pour les écoulements par bouchons. L'aplatissement de la fraction de vide est presque nulle pour les écoulements à bulles et annulaires. L'aplatissement est négatif pour les écoulements par bouchons et par écume ce qui indique une distribution de PDF plus aplatie que la normale.

Les modes locaux de la PDF sont introduits dans le but de décrire qualitativement les caractéristiques des types d'écoulement. Le premier mode local est défini comme étant le maximum apparaissant à une faible fraction de vide. Le second mode local correspond au maximum apparaissant à haut taux de vide. En traçant le second mode local de la PDF en

fonction du premier mode local de la PDF, nous obtenons une carte pour les types d'écoulement. L'axe des abscisses correspond à des écoulements à bulles alors que l'axe des ordonnées correspond à des écoulements annulaires. Les écoulements par bouchons sont éparpillés sur le demi-plan situé sous la diagonale de la carte alors que les écoulements par écume sont sur le demi-plan supérieur. Cette séparation est due au fait que le premier mode local est toujours plus grand que le second mode local pour les écoulements par bouchons. Cette situation est inversée pour les écoulements par écume. Cette carte permet de décrire qualitativement les transitions entre les types d'écoulement.

Les composantes fluctuantes des signaux du vide et de pression sont analysés en examinant leur PSDF (Power Spectrum Distribution Function). Pour les écoulements à bulles, la PSDF normalisée est composée de larges bandes de fréquence au-dessus de l'intervalle de fréquence allant de 0.2 à 18 Hz, et le spectre total d'énergie est plus faible que ceux pour les autres régimes d'écoulement couverts dans cette étude. Pour les types d'écoulement à bouchons et par écume, la PSDF présente une fréquence dominante avec plusieurs maxima plus petits. Cette observation révèle le comportement hautement oscillant de ces régimes d'écoulement. En outre, nous observons que pour les régimes d'écoulement par bouchons et par écume, le spectre d'énergie atteint les valeurs les plus élevées. Pour le régime annulaire, nous observons qu'une composante à haute fréquence presque unique caractérise les signaux de vide et de pression.

Un nouveau paramètre, le rapport spectre-énergie, a été proposé pour décrire quantitativement les résultats de l'analyse des PSDF pour différents régimes d'écoulement. Le rapport spectre-énergie est défini par le rapport entre le taux moyen de dissipation de l'énergie donné par Kocamustafaogullari et al. (1993, 1994) et les amplitudes normalisées des composantes de fréquence de la PSDF. Notons que ce type de représentation pour différents régimes d'écoulement permet une meilleure identification des transitions entre les régimes d'écoulement. De plus, en utilisant un transmetteur de pression adéquat, il devrait être possible d'étendre l'application de la technique actuelle à des systèmes vapeur-eau à hautes pressions. Grâce à la réponse en fréquence du transmetteur et de la configuration spéciale des lignes de pression, les PSDF pour les signaux de vide et de pression sont en excellent accord pour tous les cas étudiés.

Abstract

This thesis presents experimental results for the identification of two–phase flow patterns, carried out using air–water mixtures close to atmospheric conditions. The test section consisted of a transparent 12.6 x 12.6 mm, 2 m long vertical channel. Important flow values, i.e., inlet flow rates, axial void fractions and pressures were measured simultaneously. The inlet water flow rate was measured using turbine flow meters. The inlet flow rate of the air was measured using "Brooks" rotameters. Further, the axial void fractions were determined using 10 pairs of silver electrodes. The axial pressure difference was measured using a "Validyne" pressure transducer. The connections between the transducer and the pressure taps were made using short lengths of capillary copper tubes. In order to determine the local superficial velocity of the gas phase, the absolute pressure was also measured at the center of the test section using a "Sensotec" pressure transducer. The readings of all the aforementioned instruments were simultaneously handled by a data acquisition system with a sampling time of 15 ms.

The fluctuating components of the void fraction signals were analyzed using their

probability density functions (PDF). For bubbly and annular flows, the PDFs show a one–peak "unimodal" type distribution. The single peak appears at a low void fraction for bubbly flows and at a high void fraction for annular flows. Two–peak "bimodal" type distributions dominate the slug and churn flow regimes, with a maximum peak that flips horizontally during the slug to churn transition. The fact that the unimodal mode distribution for bubbly and annular two–phase flows can be easily distinguished from the bimodal distributions observed for other flow regimes was used to construct a new flow pattern representation.

The statistical moments have been used as an auxiliary tool for flow pattern identification. A significant change of the variance of both the signals of the void fraction and the pressure can be observed near the transition zones of bubbly–to–slug and churn–to–annular flows.The skewness of both the void fraction and pressure is small for bubbly flows and, in general, has negative values for slug flows. The excess is also small for both the void fraction and pressure for bubbly flows. It has negative value for both the slug and churn flows, which indicates a flatter PDF distribution than a normal one. The excess of the void fraction is close to zero for annular flows.

The fluctuating components of both, the void and pressure signals were also analyzed by examining their power spectrum distribution function (PSDF). For bubbly flows, the normalized PSDFs are broadband over the frequency range of 0.2 to 18 Hz and the total spectrum energy is smaller as compared to other flow regimes covered in this study. For slug and churn flows, the PSDFs show one dominant frequency with

several smaller peaks. This observation reveals the strong oscillating behaviour of these types of flow regimes. Furthermore, it has been also observed that for slug and churn flows the spectrum energy reaches the highest values. For the churn–to–annular flow transition, the signals become more random with their spectrum shifting toward higher frequencies. For annular flow it has been observed that an almost unique high frequency component characterize both the void and pressure signals.

An average energy dissipation rate as given in Lopes (1984) and Kocamustafaogullari *et al.* (1993, 1994) and the magnitude of each frequency component determined from the pressure signals are used to define an energy–ratio parameter. A new flow pattern representation that resulted from plotting the energy–ratio parameter, for each type of flow regime, as a function of their frequency components has been developed. It is interesting to note that this kind of flow pattern representation allows different flow regime transitions to be better identified. Furthermore, by using an appropriate pressure transducer it should be possible to extend the application of the present technique to high–pressure steam–water systems. Due to the frequency response of the transducer and the special configuration of the pressure lines, the PSDF of both the void and pressure signals were in excellent agreement for all the cases studied.

Condensé en français

Dans le design et l'opération de systèmes industriels où les écoulements diphasiques interviennent, il est essentiel de connaître les régimes d'écoulement étant donné le fait que les transferts de masse et d'énergie, les pertes de charge, ainsi que les taux de réaction chimique sont fortement influencés par la distribution des phases. Dans le design des centrales nucléaires, la plupart des codes modernes de thermohydraulique utilisés dans le calcul des conditions d'écoulement permanent et transitoire sont basés sur l'utilisation d'équations à écoulements séparés pour les phases gazeuse et liquide. De plus, il est important de pouvoir de prédire les régimes d'écoulement puisque les relations constitutives qui tiennent compte des termes d'interface en sont fortement influencés.

Traditionnellement, les régimes d'écoulement étaient identifiés expérimentalement en utilisant des techniques visuelles et/ou à haute vitesses photographiques. Les systèmes de coordonnées utilisés pour construire les cartes de régimes étaient choisis arbitrairement par différents chercheurs. Par conséquent, le manque de généralité et de précision des cartes de régimes nécessite des méthodes d'identification objectives. Nous avons vu que

les caractéristiques statistiques des mesures de taux de vide local ou de pression différentielle sont fortement reliées aux régimes d'écoulement pour des conditions d'écoulement adiabatique (Jones & Zuber 1975; Costigan & Whalley 1997) et diabatique. Les régimes d'écoulement peuvent être identifiés objectivement par une analyse statistique rigoureuse. L'identification de régimes d'écoulement basée sur l'analyse de PDF sur la fraction de vide a été initialement menée par Jones & Zuber (1975). Pour les écoulements à bulles, la PDF est caractérisée par un maximum prononcé dû aux petites bulles dans l'écoulement. Pour les écoulements annulaires, les auteurs ont trouvé un maximum unique qui correspond au taux de vide élevé. Les écoulements par bouchons sont caractérisés par la présence de deux maxima. Cette distribution de PDF à deux maxima correspond à un régime d'écoulement périodique. Aucune PDF n'a été fournie par les auteurs pour les écoulements par écume. Vince & Lahey (1982) ont recommandé d'utiliser la variance comme indicateur pour l'identification de régime. Ils ont trouvé une discontinuité dans la pente de la variance à environ 0.04 pour les transitions de régimes d'écoulement de "bulles" à "bouchons" ainsi que de "bouchons" à "annulaire". Des études similaires de PDF pour la reconnaissance de régimes sont reportés par Kelessidis & Duckler (1989); Das & Pattanayak (1993) et Costigan & Whalley (1997).

L'analyse statistique utilisant les signaux de pression plutôt que les fractions de vide est considérée comme étant un outil prometteur pour l'identification de régimes d'écoulement. La première tentative de relier les signaux de pression fluctuants avec les

régimes d'écoulement est celle de Hishikawa (1969). Les études des PDF et des PSDF sur les signaux de pression statique furent présentées et nous avons vu que les signaux de pression statique ne sont pas idéaux pour l'analyse statistique pour l'identification de régimes d'écoulement puisque seulement une partie de l'information statistique des signaux est reliée aux caractéristiques des régimes d'écoulement. Akagawa et al. (1971) ont utilisé la pression différentielle dans l'étude des écoulements par bouchons. Ils trouvèrent que la distribution de PDF était sensible à la distance entre les deux prises de pression. Matsui (1984, 1986) a mené une étude sur l'analyse de PDF utilisant la pression différentielle. Il a été montré que la PDF de la pression différentielle mesurée sur une courte distance présente les caractéristiques statistiques des régimes d'écoulement. Pour un écoulement à bulles, les PDF présentent une distribution de type normal avec un unique maximum pointu à faible taux de vide. Pour un écoulement par bouchons, la PDF montre une distribution à deux maxima. Pour les écoulement par écume, les bulles de gaz dégénèrent en bulles plus longues qui se déplacent périodiquement dans la section d'essai. Cependant, les PDF obtenues dans leur étude ne montrent pas la caractéristique typique à deux maxima pour les écoulements par écume. Pour un écoulement annulaire, la PDF présente une distribution de type normal plus large. Matsui (1986) est allé plus loin en suggérant l'identification de régimes d'écoulement à l'aide de parmamètres statistiques tels que la moyenne, la variance, coefficient d'asymétrie, et le coefficient d'aplatissement, plutôt que de calculer la PDF.

Dans ce travail, les régimes d'écoulement diphasiques sont identifiés en utilisant la PDF et la PSDF à la fois sur les signaux de fraction de vide et de pression. Nous avons construit des cartes de régimes basées sur deux descriptions statistiques quantitatives.

Dans cette étude, les expériences sont réalisées sur une section d'essai de 2 m de longueur et de section de passage de 161.3 mm^2. Un mélange air-eau proche des conditions atmosphériques est utilisé pour simuler l'écoulement diphasique. Le débit d'eau d'entrée est contrôlé par des vannes et mesuré à l'aide de débitmètres à turbine. Le débit d'air est mesuré par des rotamètres "Brooks". Quant aux taux de vide, ils sont mesurés à l'aide de la technique par impédance. Chaque paire d'électrode est d'abord calibrée en utilisant un système de vannes à fermeture rapide. La pression différentielle est mesurée grâce à un transmetteur de pression "Validyne" de sensibilité 0.1±0.25% psid. La distance axiale entre les prises de pression est 19 mm. La perte de charge diphasique par frottement est aussi déterminée par des mesures séparées en utilisant des transmetteurs de pression "Sensotec" de sensibilité 10±0.25% psig. Dans le but de déterminer la vitesse superficielle du gaz, la pression absolue est mesurée près du milieu de la section d'essai à l'aide d'un transmetteur de pression "Sensotec" de sensibilité 25±0.25% psig. Les signaux de fraction de vide, de pression différentielle, de pression absolue et de débit de liquide sont lus simultanément par le système d'acquisition de données. Pour couvrir tous les régimes d'écoulement possibles, les expériences sont menées en faisant varier les conditions d'écoulement d'entrée dans l'intervalle suivant:

flux de masse du liquide à l'entrée de 1000 à 2000 kg/m^{2}s, débit d'air à l'entrée de 0.0 à 9.2 m^3/h. Les régimes d'écoulement sont initialement identifiés visuellement à l'oeil nu. La carte de régimes d'écoulement de Taitel et al. (1980) est choisie pour réaliser une représentation préliminaire des données expérimentales.

En guise d'indicateur préalable, nous avons d'abord examiné la PDF du taux de vide à l'aide d'un analyseur "Hewlett Packard". Les données recueillies avec le système d'acquisition de données sont ensuite analysées avec un logiciel de traitement. Nous avons obtenu des résultats typiques dans notre étude. Les PDF des signaux de taux de vide pour les écoulements à bulles sont caractérisés par un unique maximum pointu. En augmentant à la fois les débits de liquide et de gaz à l'entrée, la PDF montre encore un unique maximum distinct suivi d'une queue décroissante pour les fractions de vide plus élevées. Cette queue semble être due à la présence d'un amas de bulles répartie dans un coeur de liquide. De manière générale, les PDF obtenues à partir des signaux de vide pour les écoulements à bulles ont une caractéristique statistique unimodale. Cette observation est caractéristique d'une distribution uniforme de l'écoulement. Lorsque les amas de bulles deviennent assez gros pour occuper la presque totalité de la section de passage, le régime d'écoulement par bouchons commence. Nous avons observé que les bulles de gaz en forme d'obus qui se déplacent vers le haut sont séparées par des bouchons de liquide emprisonnant des petites bulles. Nous avons aussi observé qu'un mince film de liquide se déplace vers le bas dans l'espace situé entre les grosses bulles de gaz et la paroi du canal. Les PDF des signaux de taux de vide pour les écoulements par

bouchons ont une distribution de type bimodale. Le maximum important observé pour de faibles taux de vide est dû aux bouchons de liquide contenant de petites bulles. Un deuxième maximum plus petit à haut taux de vide est relié aux bulles de gaz de forme d'obus. L'existence d'une PDF bimodale pour les écoulements par bouchons donne une indication de la nature oscillante de ce régime d'écoulement. En partant d'un régime d'écoulement par bouchons, une augmentation additionnelle du débit de gaz produit des bouchons de liquide plus aérés qui ne sont pas en mesure de maintenir le lien entre les bulles de forme d'obus. Le bouchon de liquide est donc détruit, puis retombe pour s'unir avec le bouchon de liquide suivant, pour être remonté encore par l'écoulement et détruit à nouveau. Ce comportement chaotique est caractéristique du régime d'écoulement par écume. Ce type d'écoulement produit aussi une PDF bimodale. Une augmentation additionnelle du débit de gaz force la phase gazeuse à s'écouler le long de la ligne de centre de la section d'essai, entraînant ainsi les gouttes de liquide ou des traînées de liquide (petite mèche) dans le coeur de gaz. Un mince film de liquide se déplace vers le haut entre le gaz et la paroi. Sous ces conditions, l'écoulement annulaire ou annulaire avec mèche se met en place. La périodicité observée visuellement des écoulement par bouchons et par écume disparaît dans les écoulements annulaires. Les PDF pour l'écoulement annulaire présentent un maximum unimodal à un taux de vide relativement élevé. Les écoulements annulaires sont caractérisés par une distribution axiale de l'écoulement relativement uniforme.

Les quatre moments statistiques sont utilisés comme outil auxiliaire pour l'identification des types d'écoulement. Pour les écoulement à bulles, l'asymétrie et l'aplatissement pour la fraction de vide et la pression sont faibles. Ceci concorde bien avec une distribution de PDF de type unimodale pour les écoulements à bulles avec des faibles fluctuations d'amplitude. Une forte augmentation de la variance pour le taux de vide et la pression peut être observée près de la transition entre l'écoulement à bulles et par bouchons. Cette forte augmentation de la variance indique le début d'un écoulement violent. Pour les écoulements par bouchons, la plupart des valeurs de l'asymétrie et de l'aplatissement sont négatives. Pour les écoulement par écume, la variance atteint la valeur la plus grande, indiquant ainsi un régime d'écoulement plus violent et chaotique. En général, l'asymétrie de la pression est positive, et l'aplatissement pour le taux de vide ainsi la pression est négatif. Pour les écoulements annulaires, la valeur de la variance est supérieure à celle pour les écoulement à bulles, mais inférieure à celle pour les écoulements par écume. L'asymétrie et l'aplatissement sont tous les deux plus faibles pour les écoulements annulaires.

La PSDF est appliquée aux signaux de taux de vide et de pression. Les écoulements à bulles sont caractérisés par des PSDF à larges bandes de fréquence couvrant une grande échelle de fréquences. Les valeurs de l'amplitude fluctuante des composantes de fréquence pour les écoulements à bulles sont faibles. Pour les écoulements à bulles, les petites bulles de gaz dans le coeur de liquide contribue au caractère aléatoire du procédé avec un spectre d'énergie totale relativement faible. Pour les écoulements par bouchons,

la PSDF présente un maximum dominant accompagné de plusieurs autres maxima plus faibles. La présence d'une fréquence dominante est attribuée aux bulles de gaz de forme d'obus passant périodiquement devant les prises de pression et les prises de taux de vide. La présence de petits maxima est attribuée aux petites bulles se déplaçant plus ou moins de manière aléatoire dans les bouchons de liquide. La présence d'une fréquence dominante indique la nature périodique des écoulements par bouchons. Nous avons aussi observé que la fréquence dominante augmente avec un débit de liquide d'entrée croissant. Ce comportement est dû au fait que les bulles à forme d'obus tendent à se déplacer plus vite avec une vitesse de liquide qui augmente. De plus, le spectre d'énergie des écoulements par bouchons est plus grand que celui des écoulements à bulles. De manière similaire aux écoulements par bouchons, les écoulements par écume sont caractérisés par la présence d'une composante de fréquence dominante. Notons cependant que pour un débit de liquide à l'entrée constant, la fréquence dominante pour les écoulements par écume est plus élevée que celle observée pour les écoulements par bouchons. Une fois de plus, la fréquence dominante augmente avec une vitesse de liquide croissante. Il faut mentionner que le spectre d'énergie totale pour les écoulements par écume atteint des valeurs plus élevées que pour tous les autres régimes d'écoulements étudiés. Bien que la distribution des phases semble être chaotique, la présence d'une fréquence dominante confirme la périodicité du comportement pour ce type d'écoulement. Une augmentation additionnelle du débit de gaz d'entrée permet à la distribution de l'écoulement annulaire de se développer et nous observons l'apparition d'une composante de haute fréquence dominante pointue. Comme déjà mis en évidence pour des écoulements bouillants (Jain &

Roy, 1983) et adiabatiques (Nishikawa et al. 1969), cette haute fréquence est causée par des vagues de surface qui se développent à l'interface gaz-liquide. La valeur du spectre d'énergie totale pour des écoulements annulaires est moyenne et la fréquence dominante se déplace à des valeurs plus élevées pour des vitesses d'écoulement croissantes. Il est importance de noter la forte similarité qui existe entre les PSDF obtenues pour des signaux de pression et de taux de vide. Par conséquent, en utilisant les prises de pression et les transmetteurs appropriés, la mesure de pression différentielle peut fournir une excellente information sur les caractéristiques inhérentes de la structure des écoulements diphasiques.

Les modes locaux de la PDF sont introduits afin de décrire quantitativement les caractéristiques des régimes d'écoulement. Le premier mode local est défini comme étant le maximum apparaissant à faible fraction de vide. Le second mode local correspond au maximum apparaissant à haut taux de vide. En traçant le second mode local de la PDF en fonction du premier mode local de la PDF, nous pouvons construire une carte de régimes d'écoulement. L'axe des abscisses correspond à des écoulements à bulles alors que l'axe des ordonnées correspond à des écoulements annulaires. Les écoulements par bouchons sont éparpillés sur le demi-plan situé sous la diagonale de la carte alors que les écoulements par écume sont sur le demi-plan supérieur. Cette séparation est due au fait que le premier mode local est toujours plus grand que le second mode local pour les écoulements par bouchon. Cette situation se inversée pour les écoulements par écume. Cette carte permet de décrire qualitativement les transitions entre les types d'écoulement.

Un nouveau paramètre, le rapport spectre-énergie, a été proposé pour décrire quantitativement les résultats de l'analyse des PSDF pour différents régimes d'écoulement. Le rapport spectre-énergie est défini par le rapport entre le taux moyen de dissipation de l'énergie donné par Kocamustafaogullari et al. (1993, 1994) et les amplitudes normalisées des composantes de fréquence de la PSDF. Étant donné que les écoulements à bulles sont caractérisés par un large intervalle de composantes de fréquence et de faibles taux moyens de dissipation d'énergie, ils sont représentés par des points situés en haut de la carte de régimes d'écoulement. Par contre, les écoulements annulaires, caractérisés par une unique composante de fréquence et des taux moyen de dissipation d'énergie relativement élevés, se retrouvent au bas de la carte. Entre ces deux régions, nous rencontrons les données correspondant aux écoulements par bouchons et par écume. Le fait que le taux de dissipation moyen d'énergie pour les écoulements par bouchons est plus faible que celui pour les écoulements par écume rend possible l'identification de ces deux régimes sur la carte. Cette carte de régimes d'écoulement nous permet donc de mieux identifier les transitions de régimes d'écoulement.

En conclusion, nous avons montré dans notre étude que la nature stochastique des signaux de taux de vide et de pression sont fortement dépendants du régime d'écoulement. Les techniques de PDF et de PSDF peuvent être utilisées toutes les deux pour l'identification des régimes d'écoulement. Grâce à la réponse en fréquence du transmetteur ainsi que de la configuration spéciale des lignes de pression, la PSDF pour les signaux de la fraction de vide et de la pression sont en excellent accord pour tous les

cas étudiés. L'utilisation de signaux de pression pour identifier les structures d'écoulement constituent une nouvelle technique prometteuse. L'élaboration des cartes de régimes d'écoulement est fondée sur des analyses stochastiques quantitatives de PDF et de PSDF. Les résultats montrent que l'identification objective de régimes d'écoulement mérite une plus longue attention. Finalement, il devrait être possible d'étendre l'application de la technique présente à des systèmes vapeur-eau à haute pression.

Table of contents

List of figures

List of tables

List of symbols

A	Flow area	m^2
A_k	Amplitude of k-th component of PSDF	
$ARMA$	Auto-regressive moving-average model	
D	Tube diameter	m
D_h	Hydraulic diameter	m
E	Expected value, mean value	
E_n	Normalized output of void gauges	
E_n'	Output of void gauges	$Volts$
E_{n0}'	Output of void gauges when test section full of water	$Volts$
f	Single-phase friction factor	
f	Cyclical frequency	Hz
g	Gravitation field constant	m/s^2
Gg	Gas mass flux	kg/m^2s
G_l	Liquid mass flux	kg/m^2s
$G_x(f)$	Power spectrum density function over positive frequencies	
$\hat{G}_x(f)$	Approximation of Power spectrum density function	
$HFCF$	High-frequency contribution fraction	
J_g	Superficial gas velocity	m/s
J_l	Superficial liquid velocity	m/s
J_g^*	Normalized superficial gas velocity	m/s

J_l^*	Normalized superficial liquid velocity	*m/s*
L	Tube length	*m*
n_d	Number of sub-records	
N	Sampling size, number of points per record	
Output	Output corresponding to the full range of the transducers	*Volts*
PDF	Probability density function	
Prob	Probability	
PSDF	Power spectrum density function	
$p(x)$	Probability density function	
$\hat{p}(x)$	Approximation of probability density function	
$p(X)$	Gram-Charlier polynomial	
P_g	Pressure at the outlet of the rotameters	*psig*
P_t	Random pressure output	*Pa*
P_A	Absolute pressure	*Pa*
P_R	Absolute pressure	*Volts*
Q_g^{inlet}	Gas flowrate at the inlet of the test section	m^3/h
Q_g^{meter}	Gas flowrate from rotameters	*scfm*
Q_g	Gas flowrate in the test section	m^3/h
Q_l	Liquid flowrate in the test section	m^3/h
Range	Full range of pressure transducers	*psi*
Re	Reynolds number	
$R_x(t)$	Autocorrelation function	
s	Two-phase slip ratio	
$S_x(f)$	Power spectrum density function	
T	Record length	
$u(t)$	Time window function	
$U(\theta)$	Spectral window function	
$v(t)$	Infinite time record	

$V(\theta)$	Fourier transform of $v(t)$	
V_g	Gas phase velocity	*m/s*
V_l	Liquid phase velocity	*m/s*
W_g	Gas mass flow rate	*kg/s*
W_l	Liquid mass flow rate	*kg/s*
x	Two-phase flow quality	
$X(f)$	Fourier transform of time dependent variable, $x(t)$	
α, α_n	Void fraction	
α_t	White noise input	
β	Volumetric flow quality	
$<\varepsilon>$	Average dissipation energy rate	*J/s kg*
Δt	Sampling interval	*s*
Δf	Bandwidth resolution	*Hz*
Δp	Pressure drop	*Pa*
Δp_R	Pressure drop	*Volts*
Δp_2	Two-phase pressure drop	*Pa*
Δp_0	Single-phase pressure drop	*Pa*
Δp_a	Two-phase acceleration pressure drop	*Pa*
Δp_f	Two-phase friction pressure drop	*Pa*
Δp_g	Two-phase gravitation pressure drop	*Pa*
$\Delta p_{f,1p}$	Single phase friction pressure drop	*Pa*
$(\frac{\Delta p}{\Delta z})_{f,1p}$	Single-phase friction pressure gradient	*Pa/m*
$(\frac{\Delta p}{\Delta z})_{f,2p}$	Two-phase friction pressure gradient	*Pa/m*
ΔP^*	Normalized pressure drop	
ΔP_a^*	Normalized pressure drop over a short scale	
ΔP_c^*	Normalized pressure drop over a large scale	

$(\Delta P)_h$	Hydrostatic pressure drop	Pa
Δz	Differential distance	m
Ψ_k	Spectrum-energy ratio	
ϕ_l^2	Two-phase multiplier	
ϕ_i	Auto-regressive parameter of order n	
$\phi_0(x)$	Normal frequency function	
$\phi_n(x)$	n-th derivative of normal frequency function	
θ_j	Moving average parameter of order n	
η	Dynamic signature	
τ	Time delay	s
ρ_g	Gas phase density	kg/m^3
ρ_l	Liquid phase density	kg/m^3
σ	Surface tension	N/m
σ	Standard deviation	
σ^2	Variance	
γ	Skewness coefficient	
γ_2	Excess coefficient	
ω	Angle frequency	rpm
ν_l	Liquid kinematic viscosity	m^2/s
λ	Kurtosis coefficient	
μ_l	Liquid viscosity	Ns/m^2
μ_n	n-th central moment	

Introduction

The simultaneous flow of gas and liquid in a channel may appear in different configurations as the flow velocities of the gas and liquid phases are varied. Several configurations have been observed by different experimenters. These configurations are referred to as two–phase "flow patterns". In the design and operation of industrial systems in which two–phase flows occur, it is essential to know the flow patterns due to the fact that the heat and mass transfer, pressure drop and chemical reaction rate are strongly affected by the way in which the phases are distributed in the flow. The importance of flow patterns will be illustrated by the following different two-phase flow situations.

In the simultaneous transport of gaseous and liquid petroleum compounds in a single pipeline, it is found that the changes of pressure loss will occur when the flow pattern changes over the flow lines. It is important to know the flow patterns in order to better estimate the pressure losses along the flow pipes.

In some industrial natural circulation boilers, large bullet-shaped vapor bubbles can be formed in the pipes exposed to high heat flux. If the diameter of the bullet-shaped vapor bubbles is almost equal to the tube diameter, dryout and the consequent

damage of the tube may occur. Slug flow pattern should also be avoided in long distribution lines due to its hammering effect. In such cases, it is important to choose the flow conditions in order to avoid the occurrence of slug flow in pipes. It is also important to have reliable methods to predict when or where such an unsafe flow pattern may take place.

In some chemical processes, it is useful to increase the contact surface between gas–liquid phases in order to improve the mass transfer for a better chemical reaction. In such processes finely distributed bubbles are needed to maximize the interfacial area between the two phases. Therefore, it is important to determine the flow conditions which bring about the required flow pattern, i.e., bubbly flow pattern.

In nuclear power reactors, a situation which is of special interest to nuclear designers, is to predict two-phase flow transients under various operating condisions or under the loss-of-coolant-accident conditions. Most modern thermalhydraulics codes used for calculating steady state and transient flow conditions are based on the use of separate flow equations for the vapor and liquid phases. Thus, separate time dependent conservation equations for mass, momentum and energy are applied for each phase. Under conditions of thermal and mechanical non equilibrium, e.g., saturated steam in contact with subcooled liquid or superheated steam carrying droplets of water at saturation temperature flowing with different phase velocities, the transfer of mass, momentum and energy between the phases depends on the distribution of the phases. Therefore, constitutive relationships are required to account for interfacial terms that are influenced by the distribution of the phases in the flow. In such situation, it is

important to predict the flow patterns since the constitutive relationships that are required to solve the equations of the system are very sensitive to the topology of the flow.

Two-phase flow patterns depend on the fluid properties, the flow rates, direction of the flows, the geometry of the conduit and the flow orientations.

In the past, flow patterns were identified experimentally using direct and/or high speed photographic techniques. Flow pattern maps have been proposed which use dimensional coordinates based on the liquid and gas superficial velocities or non-dimensional groups that take into account the properties of the fluids, the velocity field and the geometry of the conduit. Dukler and Taitel (1977) have shown that there exists little agreement among these maps. The discrepancies between them are mainly due to subjective criteria used by different investigators. Therefore, the lack of generality and accuracy of flow regime maps still requires objective flow pattern identification methods based on rigorous statistical objective analyses.

In general, two–phase flows are characterized by an inherent random behavior. It has been shown that specific statistical characteristics of local void fraction or differential pressure measurements are strongly related to the flow patterns for both adiabatic (Jones & Zuber 1975; Vince & Lahey 1982; Matsui 1986; Costigan & Whalley 1997; Elkow & Rezkallah 1997) and diabatic flow conditions (Jain & Roy 1983). A straight forward statistical analysis leading to flow pattern identification was first suggested by Jones & Zuber (1975). They applied the probability density function (PDF) to void fraction measurements carried out using the X-ray absorption technique. Vince

& Lahey (1982) suggested the use of the second statistical moment as an auxiliary tool for flow pattern identification. Dan & Pattanayak (1993) and Costigan & Whalley (1997) conducted an experimental flow pattern study by applying PDF analysis to void fraction signals obtained with electrical impedance probes. Elkow & Rezkallah (1997) applied PDF to the signals obtained with capacitance sensors. For slug flows, Costigan & Whalley (1997) used cross–correlation techniques to provide statistical data on the lengths of slugs. They provided more experimental information in predicting the boundaries between different flow patterns.

The analysis of the fluctuating component of signals obtained from pressure measurements has recently been considered as a promising objective technique for two–phase flow pattern identification (Han, 1998; Teyssedou & Han, 1998). In general, compared to void fraction, the pressure measurements are easily accessible even for flows with heat addition. Further, the pressure signals may contain enough information to determine not only the flow patterns but also other flow properties. Hubbard & Dukler (1966) and Nishikawa *et al.* (1969) were among the first to apply spectrum analysis of the signals obtained from pressure measurements in order to identify flow regimes. Akagawa *et al.* (1971) investigated the frequency distribution or PDF of differential pressure signals produced by slug flows. They observed that the distribution was affected by the distance between the pressure taps. Tutu (1982, 1984) used the PDF of differential pressure signals to establish a quantitative criterion for bubble–to–slug transition. Matsui (1984, 1986) performed more detailed flow pattern identification studies by using the PDF, cross–correlation and variance of differential pressure signals. Almost all of the aforementioned work provided only qualitative

statistical descriptions of the flow patterns.

The present work is intended to determine the flow patterns by analyzing the fluctuating component of both void fraction and differential pressure signals, collected from vertical air–water two–phase flows.

Chapter 1 gives a comprehensive review of different techniques used to identify the flow patterns. The most significant results encountered in the literatures are discussed in detail.

Chapter 2 describes the experimental facility used in the present study, including the air-water loop, the test section and the instrumentation.

Chapter 3 presents the experimental procedures. We present the experimental result obtained during the calibration of the system under both single– and two-phase flow conditions. These results are used later in the analysis of flow pattern data.

Typical experimental results used for flow pattern identifications are presented in Chapter 4.

Chapter 5 presents the complete analysis using four statistical moments, the probability density function and the power spectrum density function for the fluctuating signals of both void fraction and pressure.

Chapter 6 presents two quantitative criteria for flow pattern representation. These are local modes of PDF and energy-spectrum ratio based on PSDF. Two flow pattern

maps based on these two quantitative criteria are also constructed, respectively.

The concluding remarks of the current work will be presented in the last chapter.

Chapter 1

Literature Review

In general, there are two major methods that have been used to identify two–phase flow patterns. One method is to predict the transitions between different flow patterns using analytical models and correlations; the other method is to identify the flow patterns by using experimental tools. The method using experimental tools can be further classified into two different approaches. The traditional approach is to identify the flow patterns by viewing the flow through transparent channels, or by high speed photography, and to construct the flow pattern map which indicates the flow pattern existence domains directly from the experimental observation. The modern experimental approach for flow pattern identification is based on the statistical analysis of the fluctuating characteristics of the flow, such as void fraction and pressure. This approach is usually referred to as an "objective" flow pattern identification.

As an introduction to the discussion of flow pattern identification it is helpful to start with a description of flow patterns.

1.1 Description of Two–Phase Flow Patterns

For typical upward co-current two–phase flows the following flow patterns can be identified: bubbly flow, slug flow, churn flow and annular flow (including wispy–annular flow). These flow patterns are shown in Figure 1.1.

For bubbly two–phase flows, the gas is uniformly distributed in the form of discrete bubbles in a continuous liquid phase. The bubbles are usually distorted spheres having relatively small dimensions.

In slug flows, most of the gas is concentrated in large bullet shaped bubbles which have a diameter almost equal to the pipe diameter. These gas bubbles move uniformly upward and are separated by slugs of continuous liquid that fill the pipe. These liquid slugs may or may not contain small entrained gas bubbles. Between the gas bubbles and the pipe wall, one can observe a slowly descending thin film of liquid.

Churn flow is considered as a more chaotic and disordered flow pattern than slug flow. The bullet shaped gas bubbles which are seen in slug flows become narrow and their shape is distorted. The continuity of the liquid that separates the gas bubbles is repeatedly destroyed by a higher gas concentration in the liquid slug. When this occurs the liquid in the liquid slug falls down, merges with the oncoming liquid slug and is again lifted by the gas. This flow has an oscillatory character and hence is described as "churn" flow.

Annular flow is characterized by the continuity of the gas phase in the central region

(core) of the pipe surrounded by a liquid annulus on the pipe wall. The liquid phase moves upwards partly as wavy liquid film and partly in the form of droplets entrained in the gas core. Wispy annular flow occurs as a result of the agglomeration of the liquid droplets in the gas core into large streaks or wisps.

1.2 Flow Pattern Detection Methods

There are various methods available to detect flow patterns. Traditionally, flow patterns have been identified by visual observation or by using high speed photography through transparent channels (Cooper *et al.* 1963; Hewitt & Roberts, 1969). When the pipes are opaque, X–ray or γ–ray attenuation methods can be used (Vince & Lahey 1982; Jain 1983). As this technique is applied, the channel's material and thickness should be carefully chosen to avoid heavy absorption of the X–rays. Electrical contact probe techniques have also been employed to study the structure of two–phase flows. If a two–phase media is an electrical conductor then an electrical conductivity probe can be used (Das & Pattanayak 1993; Costigan & Whalley 1997). If a two–phase media behaves as a dielectric material then an capacitance sensor can be applied (Elkow & Rezkallah 1997). A thermal neutron scattering technique has been used to determine the structure of two–phase flows (Lubbesmeyer 1984; Kozma *et al.* 1992). The identification of two–phase patterns using pressure signals may be considered as a promising technique (Matsui 1986; Spedding & Spence 1993).

1.3 Traditional Experimental Flow Pattern Identification

Traditionally, flow pattern maps proposed for flow pattern transition boundaries have been determined directly from experiments. As discussed in the previous section, flow patterns were usually identified by viewing the flow through transparent channels or by high speed photography. During the experiments of flow pattern visualization or photography, experimenters also measure important flow conditions, such as gas and liquid flowrates and average void fraction. The observed flow patterns or their transition boundaries are then related to two flow parameters, or to two parameter groups with each parameter group combining the flow conditions and fluid properties. These two parameters, or parameter groups, are used to define a coordinate system in which the boundaries between different flow patterns may be charted. This leads to a flow pattern map. In general, there are two groups of coordinates used for the most common published maps.

One group represents the data in a plane where non–dimensional coordinates or a combination of dimensional and non-dimensional coordinates (Baker 1954; Taitel & Dukler 1976; Weisman *et al.* 1979) are used. In this group, the variables that are used to define the coordinates of the system include fluid properties, flow conditions and even the flow channel geometry. The coordinate systems are different according to different authors, and hence they have been more or less subjective and arbitrary. There is no agreement on the best coordinate system so far.

Another group represents the system simply by gas and liquid superficial velocities

J_g and J_l (Griffith & Wallis 1961). The superficial velocity of a given phase is defined as the volumetric flowrate of that phase divided by the cross sectional area of the conduit. Another simple coordinate system, represented by gas and liquid superficial momentum flux $\rho_g J_g^2$ and $\rho_l J_l^2$, has also been used by Hewitt & Robert (1969) and Mandhane (1974). At present, superficial gas and liquid velocities have been widely suggested as coordinates for flow regime maps, because they are simple, practical and represent main flow parameters.

1.4 Objective Flow Pattern Identification

Objective Flow Pattern Identification based on the statistical analysis of the signals produced by the fluctuation of properties such as void fraction or pressures have received increased attention during the recent years.

Some research works carried out for air–water cold–flow experiments have shown that the fluctuations of void fraction or differential pressure may provide a good insight into the flow pattern. However, the development of more appropriate predictive methods still require reliable experimental information. Therefore, in order to overcome the subjectivity of the traditional flow pattern identification methods and to reduce the incompleteness of theoretical predictive methods, it is necessary to develop objective flow pattern identification criteria for practical applications.

Many experimental studies have been carried out for the purpose of applying statistical flow pattern identification methods. Statistical functions such as the probability

density function (PDF) and the power spectral density function (PSDF) have been used in flow pattern identification.

1.4.1 Flow Pattern Identification with Void Fraction Signals

Initially, flow pattern identification, based on the analysis of void fraction, was carried out by Jones & Zuber (1975). An air–water two–phase mixture, flowing vertically in a rectangular test section, was used as the working fluid. They used the technique of the absorption of high energy X-rays for flow pattern identification. The system utilized a dual beam X-ray device. One of the beams passed through the two–phase mixture, and the other beam passed through a reference sample. The flow patterns was also observed by visualization. A typical result for PDF is shown in Figure 1.1. For bubbly flow, it can be seen that the PDF is characterized by one pronounced peak. This peak is produced by small void fraction fluctuations taking place around a mean value. For annular flows, they found a single peak that corresponds to the high void fraction region. These types of single peak PDFs are related to the so called unimodal flow distributions. In contrast, slug flows are characterized by the presence of two peaks, i.e., a bimodal distribution. The low void peak corresponds to the low void fraction liquid slugs that contained small–diameter bubbles in the water. The high void peak corresponds to the large gas bubbles in the tube. No PDFs were given by the authors for churn flows.

Vince & Lahey (1982) have demonstrated that the information available from PDF is not sufficient to distinguish the flow patterns. They recommended the use of the

variance or the second central moment around the mean value of the PDF distribution as an indicator for pattern identification. By plotting the variance as a function of void fraction, as shown in Figure 1.2, they found that a discontinuity in the slope of the variance can be noted at about 0.04 for both the transitions from bubbly–to–slug and from slug–to–annular flows. A variance greater than 0.04 indicates slug flows while smaller variances indicate bubbly or annular flows, depending on the mean void fraction. For slug flows, the presence of low void fraction due to the entrained bubbles in the liquid slugs, and a high void region due to the large spherical cap bubbles, produces a large variance from the mean. The disappearance of the liquid slugs contributes to a significant decrease in the variance which can therefore be used as an indicator of transition from one pattern to another. However, they admitted that the transition at a variance of 0.04 may be only characteristic of their experimental facility with low pressure air/water flow in a 2.54cm I.D. vertical tube. They suggested that more experimental work was still required.

Similar PDF studies for flow pattern recognition carried out in a vertical round tube were also reported by Das & Pattanayak (1993). Kelessidis & Dukler (1989) also reported data collected in vertical concentric and eccentric annuli. Costigan & Whalley (1997) have performed flow pattern identification with PDFs and reported similar PDF results for flow patterns to those obtained by Jones & Zuber (1975) in vertical two–phase flow. They concluded that under low liquid flowrates bubbly flow occurs for void fraction less than 45% at all times and annular flow exists when the void fraction are higher than 80%. Stable slug flow exists when the two PDF peaks are respectively around void fraction of 40% and 80% or higher.

Power spectrum density function has been used by Jan & Roy (1983) for flow pattern identification with the signals of static pressure and void fraction collected in a vertical heated concentric annular test section. The pressure was measured with a piezo–electric pressure transducer and the void fraction with a dual–beam X–ray system. The analysis of the pressure signals has shown the presence of several PSDF peaks for bubbly flows. However, for slug flows, only a single peak was observed. A single peak was also seen for annular flows. The study of the void fraction signals showed similar features of the PSDF.

Wang *et al.* (1988, 1990) also used PSDF in flow pattern identification with the void fraction measured signals in a upward vertical flow system. They further proposed the term "High-Frequency Contribution Fraction" (HFCF) in flow pattern recognition. HFCF was defined as the ratio of the PSDF of high frequency components to the PSDF of the whole frequency components:

$$HFCF = \frac{\sum_{k=s}^{N/2-1} PSDF(k)}{\sum_{k=0}^{N/2-1} PSDF(k)}, \tag{1.1}$$

where, N was the sampling size; Δf was bandwidth resolution, given by:

$$\Delta f = \frac{1}{N\Delta t}. \tag{1.2}$$

The symbol "s" in Equation 1.1 is a data point in order to give the boundary between low and high frequency components. Wang *et al.* (1988, 1990) chose $10Hz$ as the boundary between low and high frequencies because they found that there was no PSDF peak appearing above $10Hz$ for all the spectra of slug flows during the experiments. Therefore, the value "s" can be approximately calculated from Equation 1.2

such as:

$$(s-1)\Delta f \leq 10,$$

$$s = \text{Integer}[10N\Delta t] + 1.$$

Since for bubbly flows the fluctuating component of the signals are characterized by small amplitudes and high frequencies, the HFCF is the highest for this flow pattern. In annular flows the interfacial waves with various amplitudes and periods contribute to high frequency components, while the droplets contained in the gas core occasionally contribute to low frequency components, and therefore the HFCF for annular flows is of a middle value. In slug flows the HFCF value is the smallest, which differentiates this kind of flow pattern from those of the other flow patterns. Churn flow is regarded by Wang *et al.* (1988, 1990) as a transition flow between slug flow and annular flow, and the HFCF values of churn flow are between those of slug flow and annular flow.

1.4.2 Flow Pattern Identification Using Neutron Noise Analysis

It has been shown that the characteristics of the neutron–detector signals depend on the flow pattern of the liquid. As the two–phase flow has a fluctuating nature, the resulting measurements of the neutron densities exhibite a fluctuating intensity, reflecting both the local and global variations in the flow structure. Therefore, some researchers have proposed a method for flow pattern identification in boiling water reactors by analyzing the neutron–detector signals using statistical functions (Lubbesmeyer & Leoni 1983; Lubbesmeyer 1984; Kozma *et al.*1992). This method is

based on a comparison of several statistical functions of known flow-pattern signals in a simple air–water test facility and the equivalent functions computed from the neutron-detector signals of the investigated two–phase flow in boiling water reactors. Kozma *et al.* (1992) have reported the experimental study of flow pattern identification in boiling two–phase flow using neutron noise analysis. Air and water were used as the working fluid, flowing vertically in a narrow rectangular channel between the fuel plates of a simulated reactor fuel assembly. The fuel assembly was electrically heated. Flow patterns have been obtained by varying the coolant flow rate and the electrical power. Neutron detectors were located axially in the neighborhood of the boiling region. The signals from neutron detectors were used for PDF analysis. The authors have analyzed the data using the following four statistical moments:

- The first moment, the mean value of the signal, denoted by E.
- The variance, or the second central moment, a measure of scattering around the mean value of the signals, denoted by σ^2.
- The skewness coefficient, or the third central moment normalized by the third power of the standard deviation, a measure of the asymmetry of the distribution, denoted by γ.
- The kurtosis coefficient, the fourth central moment normalized by the forth power of the standard deviation, a measure of the peakedness of the distribution, denoted by λ.

The authors have found that slug flow are characterized by two PDF peaks and a large variance of the PDF. They argued that the large variance is due to the oscillating character to partial channel blockage caused by steam slugs generated periodically between the plates. The value of the kurtosis coefficient is smaller than 3 (almost flat PDF). On the other hand, PDFs of bubbly and annular flows are single-peaked. Their variances are small. The values of kurtosis coefficient are greater than 3. Bubbly and annular flow patterns can be distinguished on the basis of the position of the PDF peak. For bubbly flows the PDF peak corresponds to low void fraction values, while for annular flows the observed peak corresponds to a high void fraction. The skewness coefficient of the PDF, however, did not produce a consistent criterion for flow pattern identification. Moreover, the PSDF has shown that slug flows are characterized by a strong peak at low frequencies.

1.4.3 Flow Pattern Identification Using Pressure Signals

Statistical analysis using pressure signals, rather than void fraction, has been a promising tool for flow pattern identification. Compared with the measurements of void fraction, the instruments for measuring pressure signals are less complex. Pressure signals are easily accessible to measurements and may contain sufficient information on the features of the various flow patterns. In boiling water reactors, it has been shown that the fluctuations of pressure signals are strongly affected by the transient characteristics of flow patterns. However, to the author's knowledge, few of the published papers have reported the research on flow pattern identification using pressure signals.

The first attempt to relate the fluctuating pressure signals to flow patterns was that of Nishikawa (1969) who investigated the statistical properties of static pressures of each flow pattern in upward air–water flow in a 26.0 *mm* I.D. tube. Frequency distribution and power spectrum density function of static pressure signals for different flow patterns were presented. However, the fluctuations of the static pressure signals consists of two parts. One part of the fluctuations is due to the mechanical vibrations of the whole measuring system, which is called the global fluctuation. The other part of the fluctuations is due to the flow fluctuation, or void fraction fluctuation, in the measuring section, which is called local fluctuation. It is obvious that only the local fluctuation is related to the flow pattern. Static pressure signals are not the prefered signals for the statistical analysis of flow pattern identification since only part of the statistical information of the signals is related to the features of the flow patterns. The determination of flow regimes by the statistical characteristics of the static pressure presents some difficulties in the research of Nishikawa (1969). For example, the PSDF of the static pressure signals for slug flows presents more than one peak and it is difficult to tell which peak represents the periodical feature of slug flows and which one is due to the system vibration.

In order to eliminate the effect of static pressure fluctuations which contain information from regions outside the test section, Akagawa *et al.* (1971) used the differential pressure or pressure drop, instead of the absolute pressure, in their study of slug flows in a vertical air–water flow loop. They verified that the system mechanical vibration has the same effect on the fluctuation of the static pressure signals measured at different locations along the test section. Hence, this common effect coming from the

whole system disturbances can be eliminated by using the signal resulting from the subtraction of two static pressures. This leads to the use of differential pressure signal for statistical analysis for flow pattern identification. PDF as an important statistical feature was used by Akagawa *et al.* (1971) for the differential pressure signals on slug flows. They found that the PDF distribution was also sensitive to the distance between the two differential pressure taps. The PDF for the differential pressure over a long distance has shown a one-peak normal distribution for slug flows. This distribution for slug flows has shown no difference from that for bubbly flows. However, the PDF for the differential pressure over a small distance has shown a two-peak distribution. This suggested that a series of properly chosen differential pressure signals could be used to identify the flow patterns.

A detailed study on PDF analysis using differential pressure have been carried out by Matsui (1984, 1986). The experiments were carried out in a tube having 22.0 *mm* I.D. with a mixture of water and nitrogen as the working fluid. In the paper, a normalized differential pressure was given, which is the ratio of the differential pressure of the two–phase mixture, Δp_2, to the differential pressure of the still fluid column in the corresponding test section, Δp_0. It is expressed as:

$$\Delta P = \frac{\Delta p_2}{\Delta p_0}. \tag{1.3}$$

The author assumed that the acceleration and friction pressure losses in the two–phase flow could be neglected because their values were very small compared with $(\Delta p_0 - \Delta p_2)$.

Therefore, when the test section is full of water the quantity $(1 - \Delta P)$ is equal to

zero, while the quantity $(1 - \Delta P)$ is equal to one when the test section was empty. This quantity represents approximately the average void fraction in the test section. The normalized quantity $(1 - \Delta P)$ which is denoted by ΔP^* was used to perform the PDF analysis:

$$\Delta P^* = 1 - \Delta P. \tag{1.4}$$

In order to study the relationship between the PDF distribution of differential pressure fluctuations and the distance where the two pressure taps are mounted, two distances for differential pressure measurements were chosen. The short distance is equal to the inside radius of the pipe in order to recognize spherical cap bubbles flowing in the pipe. The large distance is equal to ten times the diameter of the pipe. The arrangement of the differential measurements is shown in Figure 1.3.

Under the same experimental conditions, the differential pressures over both the small and large distances were collected. The PDFs were analyzed using the normalized differential pressure for the small distance (ΔP_a^*) and for the large distance (ΔP_c^*), respectively. Typical results of PDFs as the function of void fraction for each flow pattern are shown in Figure 1.4.

For bubbly flow in which small bubbles are dispersed uniformly in the liquid, the PDFs of both ΔP_a^* and ΔP_c^* show a normal type distribution with a single sharp peak at a low void fraction.

Since for slug flow, the gas–plug and the liquid–slug with small entrained bubbles pass alternatively through the pressure sensor, the PDF of ΔP_a^* shows a peculiar distribution with two peaks. The liquid–slug with small bubbles contributes to the

peak at a low void fraction, while the gas–slug contributes to the peak at the higher void fraction. Matsui (1986) explained that the peak on the left side is higher than the peak at the right side because the liquid–dominant portion is longer than the gas–dominant portion, therefore the ratio of two peaks in slug flows indicates the ratio of liquid and gas dominant portions of the slugs. However, the PDF of ΔP_c^* for slug flow shows a distribution with one peak. It has been shown that some statistical information is lost when the distance between pressure taps is increased.

For churn flow, the gas bubbles have degenerated into longer ones and move more frequently through the test section. It is still a periodical pattern, however, the PDFs of both ΔP_a^* and ΔP_c^* did not show typical two–peak features for churn slows.

For annular flow, the PDF of ΔP_a^* shows a wider normal type distribution. A sharp peak distribution is obtained for ΔP_c^*.

It has been shown that the PDFs of the differential pressure measured over a small distance exhibits the statistical characteristics of flow patterns.

Matsui (1986) has further tried to fit the PDF data of the differential pressure over the small distance using Gram–Charlier polynomial expression. It is suggested that the flow patterns can be identified with the statistical parameters, such as mean, variance, skewness coefficient and excess coefficient, instead of calculating the PDF. After calculating the corresponding statistical parameters, the fitting curves of PDF can then be constructed.

The Gram–Charlier polynomial expression of order $n = 6$ was chosen by the author

for fitting the PDF data:

$$p(X) = a_0\phi_0(X) + a_1\phi_1(X) + a_2\phi_2(X) + a_3\phi_3(X) + a_4\phi_4(X) + a_5\phi_5(X) + a_6\phi_6(X), \tag{1.5}$$

where,

$$\phi_0(X) = \frac{1}{\sqrt{2\pi}} e^{-X^2/2},$$

$$\phi_n(X) = \frac{d^n}{dX^n}\phi_0(X),$$

$$n = 1, 2, \ldots, 6,$$

$$a_0 = 1,$$

$$a_1 = 0,$$

$$a_2 = 0,$$

$$a_3 = -\mu_3/3! \quad ,$$

$$a_4 = (\mu_4 - 3)/4! \quad ,$$

$$a_5 = -(\mu_5 - 10\mu_3)/5!,$$

$$a_6 = (\mu_6 - 15\mu_4 + 30)/6!,$$

$$\gamma_1 = -3!a_3 = \gamma,$$

$$\gamma_2 = 4!a_4 = \lambda - 3.$$

μ_n is the n-th central moment defined in section 5.3. γ_2 is called the excess coefficient. The excess coefficient is the value of the kurtosis coefficient (λ) minus three.

The variable X in Equation 1.5 is normalized by the mean, E, and the standard deviation, σ, given by:

$$X = \frac{x - E}{\sigma}.$$

The results of curve fitting for the PDF data are shown in Figure 1.5. In general, the fitting to the PDF distribution is good, except that the fitting for slug flows sometimes has negative values of low tertiary peaks. These tertiary peaks are due to the nature of the polynomial used by the author.

The results of curve fitting has shown that the statistical parameters, which are used to determine the coefficients of the Gram–Charlier polynomial, characterize the PDF distributions of flow patterns. The values of these parameters can be obtained by directly processing the signals from differential pressure fluctuation measurements. Therefore, the envelope of the PDF configuration of flow patterns can be obtained based on these parameters, without calculating the PDF from the differential pressure signals.

It has been found that the average value, E, becomes larger with the transition of flow patterns from bubbly flow → slug flow → churn flow → annular flow.

The variance, σ^2, for bubbly flow is the smallest. The variance for slug flow is larger than that for bubbly flow. The variance of churn flow is the largest among the four flow patterns. The churn flow is regarded as the most chaotic flow pattern. In annular flow the variance is less than that seen in slug or churn flow, but larger than that seen in bubbly flow. The above variance results of Matsui (1986) show the same trends as

those of Tutu (1982) and Kozma (1995).

The skewness coefficient is considered to be a measure of the asymmetry of the PDF distribution. If γ_1 is positive, the long tail of PDF should be on the positive side of the distributions, and if γ_1 is negative, the long tail is on the negative side. For bubbly and annular flows, the skewness is rather small. The skewness for slug flow has a larger and positive value, while the skewness for churn flow has a large and negative value.

The excess coefficient is used as a measure of the degree of flattening of a frequency curve near its center. If γ_2 is positive, the frequency curve is taller and slimmer in the neighborhood of the maximum point. As an example, a normal distribution has a small value of the excess coefficient. Thus the distributions of bubbly flow and annular flow should have positive values of the excess coefficient. For slug or churn flow the distributions should be flatter than normal distributions, and the value should be negative. However, Matsui (1986) did not provide correct results of the excess coefficient. For examples, the flow which was classified as churn flow by Matsui (1986) might be classified as churn–to–annular transition flow by other authors. In view of the lack of theoretical understanding of flow transitions, objective criterion for flow pattern identification needs to be developed in the meantime.

Similar PDF studies were also reported by Tutu (1982) and Das & Pattanayak (1993). In their studies, the PDFs of churn flow show a two–peak distribution, which reveals the periodic feature of this kind of flow.

In general, two–phase flow fluctuations may contain some dynamic information that could be tailored into a statistical model to provide a flow signature, i.e., flow characteristic. This kind of flow signature can provide a quantitative description of the different two–phase flow regimes.

In an effort to carrying out a quantitative analysis for flow pattern identification, King *et al.* (1988) used another statistical tool, called the time series analysis method, to identify air–water two–phase flow regimes based on the differential pressure signals. The experiments were carried out in a vertical 24 mm I.D. tube. The auto–regressive moving–average (ARMA) model as a basic difference equation in the form of a time series has been used. This model represents the relationship between the driving forces, i.e., a white noise random input (α_t), and the pressure output (P_t). The order of the ARMA model and the value of the dynamic signature that can be obtained from the model have been used as two quantitative statistical parameters for flow pattern identification. The ARMA model is expressed by:

$$P_t + \phi_1 P_{t-1} + \phi_i P_{t-i} + \ldots + \phi_n P_{t-n} = \theta_0 \alpha_t + \theta_1 \alpha_{t-1} + \theta_j \alpha_{t-j} + \ldots + \theta_{n-1} \alpha_{t+1-n}, \quad (1.6)$$

where, $\phi_i (i = 1, 2, ..., n)$ is the autoregressive parameter, $\theta_j (j = 0, 1, ..., n-1)$ is the moving average parameter and n is the order of the ARMA model. The order of the model is determined by the "trying" method. The residual variance of ARMA is calculated for several different values of n. The value of n which results in the minimum residual variance is chosen or optimized as the order of the model.

The dynamic signature η is defined as:

$$\eta = \frac{\text{original variance of pressure signals}}{\text{residual variance of ARMA model}}.$$

A detailed algorithm for the residual variance of the ARMA model is given in King *et al.* (1988). The dynamic signature, the order of the ARMA model and the power spectrum density function based on the ARMA model shown in Figure 1.6, are combined to identify the flow patterns.

For bubbly flow some peaks exist in the spectrum. King *et al.*(1988) explained that these peaks can be attributed to a series of dense and sparse bubble clouds. The dynamic signature had lower values compared with that of other flow regimes.

For slug flow most spectral density curves presented a dominant peak at a low frequency, which reflected the periodic nature of slug flow. The peak width for underdeveloped slug flow was wider than that for fully developed slug flow. This phenomenon could be attributed to the variations in the lengths of gas bubbles and liquid slugs under different flow conditions. The dynamic signature, η, of slug flow had an intermediate value.

The amplitude of the pressure fluctuations for churn flow was larger than that of any other flow regime. The value, η, for churn flow was quite high.

For annular flow, the authors had difficulty in providing consistent values of the dynamic signature.

It has been found that the order of the ARMA model for annular flow is always equal to 2 and that it was greater than 2 for churn flow.

Therefore, the flow patterns are determinable based on the classification of the sta-

tistical features.

1.5 Theoretical Models for Predicting Flow Pattern Transition Boundaries

Some investigators have directed their efforts towards the development of theoretical models for the prediction of the flow pattern transition boundaries, which is helpful for us to theoretically understand the mechanisms that govern the changes from one flow configuration to another. The coordinate system consisting of the superficial gas and liquid velocities was commonly used for constructing the theoretically based flow pattern map. The principal work in this field was carried out by Taitel *et al.* (1980), Mcquillan & Whally (1985), Mishima & Ishii (1984), Dukler & Taitel (1986) and Barnea (1987).

Taitel *et al.*(1980) as well as Dukler & Taitel (1986) gave theoretical based criteria covering all the typical flow pattern transitions. Barnea (1987) tried to generalize the existing transition models to take into account the effect to the inclination of the pipe.

Due to the fact that the churn flow pattern is the most complex one, some researchers focused their attention on the study of the transition curves for slug-to-churn flow (Brauner *et al.* 1986; Jayanti *et al.* 1992; Mao & Dukler 1993).

1.5.1 Flow Pattern Transition from Bubbly to Slug Flows

The transition process from bubbly to slug flow needs an agglomeration or coalescence mechanism to take place. In general, as the gas flow rate is increased, the gas portion in the flow increases and more bubbles are generated in the pipe. As the number of the bubbles increases, the distance between them decreases. This closer bubble spacing results in an increase in the rate of coalescence. However, when the liquid flow rate increases, the turbulent fluctuations associated with the flow can cause the breakup of larger bubbles formed as a result of agglomeration. Thus, two processes control the stability of bubbly flow. One is the bubble agglomeration caused by the coalescence of bubbles; the other is the bubble breakup caused by the increase of the turbulence in the liquid phase.

Taitel *et al.* (1980) for the first time divided the bubbly flow into two distinctive regimes. One was called bubbly flow in which the flow was not sufficiently turbulent to suppress the formation of relatively larger gas bubbles, and the second was called dispersed bubbly flow in which bubble breakup due to the turbulent force was dominant.

According to the published data of Taitel *et al.* (1980), for low liquid flow rates, i.e., conditions under which bubble breakup due to turbulence was small, the void fraction rarely exceeded 25%. Together with the relation for the rise velocity of large bubbles, they proposed the following criterion for transition from bubbly flow to slug flow:

$$J_l = 3.0 J_g - 1.15 \left[\frac{g(\rho_L - \rho_g)\sigma}{\rho_l^2} \right]^{\frac{1}{4}}, \tag{1.7}$$

where, J_g and J_l are gas and liquid superficial velocities respectively; ρ_g and ρ_l are gas and liquid densities respectively; g is gravity field constant and σ is the surface tension.

Once the fluid properties were known, the transition curve could be plotted using a J_l vs J_g (represented by J_{l_s} vs J_{g_s} in Figure 1.7) coordinate system. They pointed out that this representation was invariant with respect to the size of the tube.

At high liquid flow rates, once the turbulent fluctuations were vigorous enough to cause the bubbles to break up into smaller sizes, coalescence was suppressed and the dispersed bubbly flow pattern must develop. In general, the void fraction in the pipe could be higher than 25% in this situation. For vapor void fractions higher than 25%. Taitel *et al.* deduced the following transition model for the flow conditions at which turbulent induced dispersion took place:

$$J_l + J_g = 4.0 \left\{ \frac{D^{0.429} \left(\frac{g}{\rho_l}\right)^{0.089}}{\nu_l^{0.072}} \left[\frac{g(\rho_l - \rho_g)}{\rho_l} \right]^{0.446} \right\}, \tag{1.8}$$

where, D is the tube diameter and ν_l is the kinematic viscosity of the liquid. The plotting of this equation resulted in curve B as shown in Figure 1.7.

However, regardless of how much turbulent energy was available to disperse the mixture, bubbly flow cannot exist at packing densities above $\alpha = 52\%$, which is the maximum void fraction of spherical bubbles arranged in a cubic lattice. Thus the curve B delimiting dispersed bubbly flow must terminate at curve C in Figure 1.7 which related J_l and J_g for $\alpha = 52\%$.

It has been shown that, in bubbly flow, the flow contained deformable bubbles which

moved upwards with a zigzag motion with Taylor-style bubble appearing occasionally, whereas in dispersed bubbly flow, Taylor bubbles were absent. It was also argued that dispersed bubbly flow can be observed over the whole range of pipe inclination, while the bubbly flow pattern can be only seen in vertical flows for relatively large diameter tubes (diameter bigger than 5 cm). This observation was also confirmed by the experiments carried out by Barnea (1987).

In conclusion, it seemed that the averaged void fraction is the main factor in the determination of flow transition from bubbly to slug flow.

1.5.2 Flow Pattern Transition from Slug to Churn Flows

The slug–to–churn transition was rather difficult to describe exactly, because of the disagreement that existed between the possible mechanisms responsible of triggering churn flow.

For the transition from slug to churn flow in upward vertical tubes, there existed four major mechanisms:

- entrance effect (Taitel *et al.*, 1980; Dukler & Taitel, 1986 and Mao & Dukler 1993),
- wake effect (Mishima & Ishii, 1984),
- bubble coalescence (Brauner & Barnea, 1986),
- flooding (McQuillan & Whalley, 1985 and Jayanti & Hewitt, 1992).

Taitel *et al.* (1980); Dukler & Taitel (1986) and Mao & Dukler (1993) treated churn flow as an entrance phenomenon. It was argued that a liquid slug between two bubbles was unstable and alternately rises and falls. The liquid slug was too short to support a stable liquid bridge between two consecutive gas bubbles. The falling film around the bubble penetrated deeply into the liquid slug creating a highly agitated aerated mixture, at which point the liquid slug disintegrated and falled in a chaotic pattern. Most of this liquid merged at a lower level with the next liquid slug and resumed its upward motion. This process repeated itself and the lengths of liquid slug and gas bubble increased as they moved upward. Thus, if the pipe was long enough, this collapsing and merging of successive slugs would ultimately become stable and lead to steady slug flow. As the gas flow rate increased, the length of this entrance region increased. According to the entrance effect model, churn flow was essentially a developing slug flow, and stable slug flow would be formed if the length of the pipe was greater than a certain value. The resulting flow pattern maps were compared with the authors own experiments carried out in a tube of 2.5 cm I.D. at low pressure for a air–water mixture. However, the experiments of Jayanti & Hewitt (1992) showed that churn flow pattern can be still observed in the region of the tube in which slug flow was predicted to prevail by Taitel *et al.* (1980).

Mishima & Ishii (1984) attributed the collapse of the liquid slug to the wake effect of gas bubbles. At a point close to the slug–churn transition, the liquid slug would be very short, and the gas bubbles would be very close to each other. This would create a strong wake effect which would destabilize the liquid slug and destroy it. This led to the occurence of churn flow.

Mishima & Ishii (1984) proposed a theoretical model to determine the transition from slug–to–churn flow. In general, there was good agreement between the model and their experimental data obtained under atmospheric pressure. However, their slug–to–churn transition curve was in disagreement with that obtained by Taitel *et al.* (1980). This might be due to the large difference in the proposed mechanisms of the slug–to–churn flow transition.

Brauner & Barnea (1986) attributed the slug–to–churn transition to the coalescence of bubbles within the highly aerated liquid slugs. According to them, the gas phase was entrained in the liquid slugs and was kept in the form of dispersed bubbles because of the turbulence within the slug. When the void fraction in the liquid slug reached a value of 52%, the separation between bubbles became too small and the coalescence of bubbles took place. This destroyed the identity of the liquid slug and led to churn flow. Thus, the transition from slug to churn flow occurred when the void fraction in the liquid slug was higher than 52%. The model they proposed showed good agreement with their experimental data. The prediction of their model was also in agreement with the work of Dukler & Taitel (1986) for the tube length–to–diameter ratios of $L/D = 250 \sim 500$. However, the model was not able to predict the experimental data of Jayanti & Hewitt (1992) obtained under low liquid flow rate conditions.

Flooding is a phenomenon in which the liquid film in counter–current flow of gas and liquid breaks down due to the formation of large interfacial waves. The flooding mechanism has been proposed to explain the slug flow to churn flow transition by,

among others, Wallis (1969), McQuillan & Whalley (1985), Govan *et al.* (1991), Jayanti & Hewitt (1992) and Hewitt & Jayanti (1993). All these authors argued that the transition from slug to churn flow was due to the result of the increase of the gas flow rate in the slug up to a limit at which it caused flooding of the falling film surrounding the gas bubble. The link between flooding and churn flow in upward vertical flow was established experimentally in some cases. For example, Wallis (1969) observed that the air velocity required to initiate flooding in a falling film of very small flow rate was roughly the same as that at the slug–to–churn flow transition. Similarly, in a flooding experiment in which the water feed was fixed at a midway point rather than at the top of a vertical test section, Govan *et al.* (1991) observed that the flow configuration above the point of water injection was typical of churn flow when flooding occurred in the pipe.

McQuillan & Whalley (1985) and Govan *et al.* (1991) used the best known semi-empirical model proposed by Wallis (1969) for the prediction of flooding velocities to determine the boundary between slug-to-churn transition in upward vertical tubes. This relation was given as:

$$\sqrt{J_g^*} + m\sqrt{J_l^*} = C, \tag{1.9}$$

where, J_g^* and J_l^* are the dimensionless gas and liquid superficial velocities. The definitions were given in McQuillan & Whalley (1985).

The constant C in Equation 1.8 depends on many factors, such as tube end conditions and tube length. McQuillan & Whalley (1985) proposed to use $m = C = 1$ to predict the transition boundary between slug and churn flow.

Jayanti & Hewitt (1992) compared the above four models for the transition of slug–to–churn flow with the data obtained by Owen (1986) in a 20 m long and 0.0318 m I.D. test section at a pressure of 2.4 *bar* over a wide range of air and water flow rates. The flooding model of McQuillan & Whalley (1985) gave satisfactory results mainly for at low liquid flow rates.

Govan *et al.* (1991) studied the relationship between flooding and the slug-to-churn transition using pressure gradient data. It has been shown that for low liquid flow rates the transition to churn flow was accompanied by a large and sudden increase in the pressure gradient, see Figure 1.8. This might be significant because a similar jump in the pressure gradient can also be observed after flooding in counter-current flow. However, for high liquid flow rates there was no jump in the pressure gradient near the slug–to–churn transition.

1.5.3 Flow Pattern Transition from Churn to Annular Flows

If the gas flow rate becomes sufficiently high annular flow will be observed. The liquid film flows upward adjacent to the wall and gas carrying entrained liquid droplets flows in the center of the tube. The liquid film flowing upward against gravity results from the force exerted by the fast moving gas core. This film has a wavy interface and the waves tend to shatter and enter the gas core as entrained droplets. Thus, the liquid moves upwards, due to both interfacial shear and form "drag" on the waves and drag on the droplets. Annular flow occurs when the gas flow rate becomes high enough to suspend entrained liquid droplets.

Dukler & Taitel (1986) applied the balance of the drag and gravity force acting on a droplet to obtain an equality which must be satisfied for the formation of annular flow:

$$\frac{J_g \rho_g^{\frac{1}{2}}}{[\sigma g(\rho_l - \rho_g)]^{\frac{1}{4}}} = 3.1. \tag{1.10}$$

It can be seen that this transition did not depend on the liquid flow rate and pipe diameter.

The above theoretically based transition for annular flow was in good agreement with several published empirical transition models. However, for high liquid rates, there was discrepancy among the available models.

It should be noted that although various aspects of boiling flow in nuclear reactors have been the subject of many experimental studies, relatively little attention was paid to flow regime identification in such systems. Most reported studies on flow regimes were based on observation in adiabatic flow experiments where two–phase flow was produced by mixing air (or vapor) and liquid at the inlet of a test section. The flow pattern transitions are affected by the heat addition through channel walls. Application of transition criteria which were obtained from adiabatic flow data to boiling channels may give misleading results. It must be pointed out that to date there are no general flow pattern maps, correlation or transition criterion which reflect the influence of heat flux.

1.6 Discussion

As presented above, there are three methods for flow pattern identification. These are traditional flow pattern identification, objective flow pattern identification and theoretical modelling to predict flow pattern transitions.

Traditional flow pattern maps directly based on experimental data have been basically used as the tool for flow regime identification. It is important to mention that the flow pattern maps have been in general prepared from data taken for a particular experimental pipe size and working fluid. Thus, it is not surprising that some of them are not valid for other tube sizes or fluids. The coordinate system that were used to construct the flow pattern maps have been more or less arbitrarily chosen by different researchers. Therefore, the flow patterns and their transitions may lack in their generality and accuracy. It may happen that part of an existent flow pattern on one flow pattern map may disappear on another flow pattern map for which different coordinates were chosen. Flow pattern detection by visualization or high-speed photography may also lead to the subjectivity of the observer being involved in distinguishing between the various flow regimes.

Theoretical flow pattern maps based on the possible governing mechanism for flow pattern transition are important in flow pattern identification. The models and/or correlations used to predict the transitions incorporate the effect of fluid properties and pipe size and thus they are largely free of the limitations of empirically based transition maps. However, theoretical models have to be validated by experimental

data. Existing theoretical flow pattern maps are not usually in good agreement with each other. They are also not usually supported by the experimental data. This may be due to the following reasons:

- There are some difficulties involved in the definition of flow patterns by different authors, especially in the identification of the transition regimes. For example, for high liquid flow rates, it is hard to distinguish the slug flow from the churn flow. Thus, some experimental data, which were considered to be related to slug flow by one author, may be classified as being churn flow by another author.
- All the theoretical models have been developed on the assumption that the two–phase flow evolves during the boiling process. However, the models were validated by experimental data obtained from adiabatic two–phase flow experiments. Thus, the discrepancy between the theoretical models and experimental results is inevitable.
- A number of different flow transition mechanisms have been proposed by different researchers, and they are not usually in agreement with each other. Therefore, further study is required to completely understand the flow transition mechanisms. There may be different mechanisms for churn flow pattern for low and high liquid flow rates, respectively.

It has been shown that two–phase flow patterns are strongly related to their fluctuating behavior. Statistical analysis of a fluctuating flow parameter has been a promising objective method for flow pattern identification. Only one fluctuating flow parameter, such as void fraction or differential pressure, has been used for the statistical

analysis. Therefore, this objective method is practical and improves the generality of flow pattern prediction because it is free of fluid properties. It must be pointed out that all the research work in this field has been restricted to qualitative statistical analysis of the flow signals. No flow pattern map based on quantitative statistical analysis has been constructed so far. In our study, we have conducted the statistical analysis for flow pattern identification qualitatively as well as quantitatively. Flow pattern maps based on quantitative statistical descriptions have been constructed.

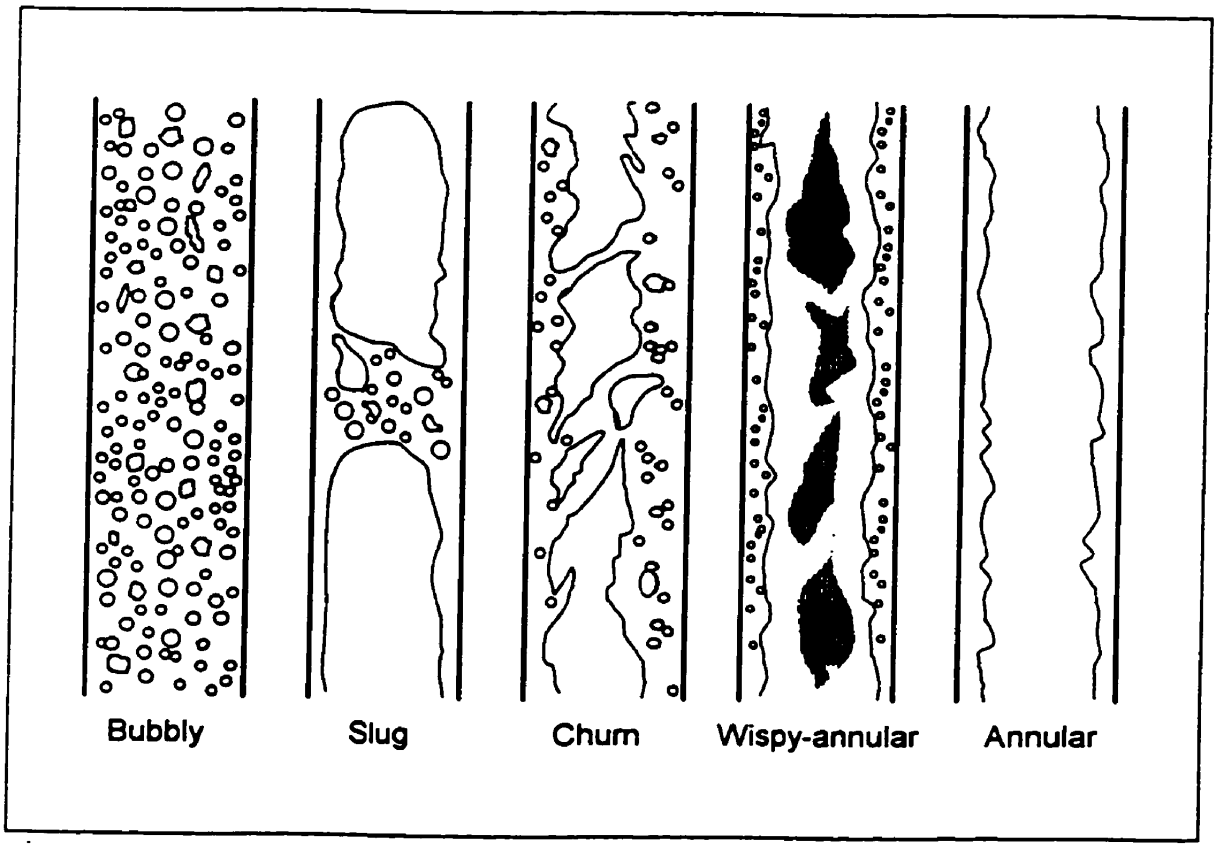

Figure 1.1: Typical flow patterns in vertical two–phase flow.

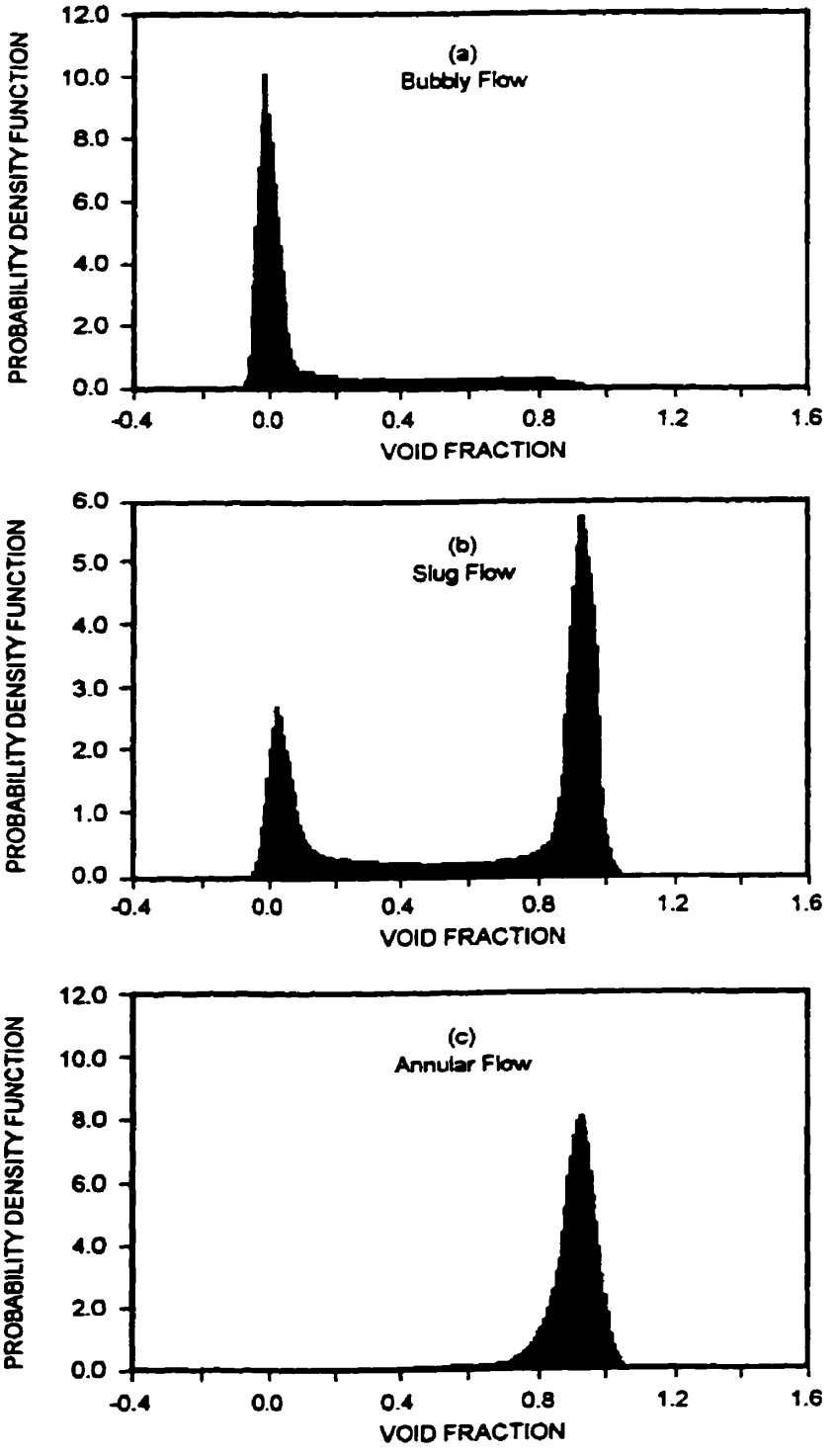

Figure 1.2: PDF figures of void fraction (Jones & Zuber,1975).

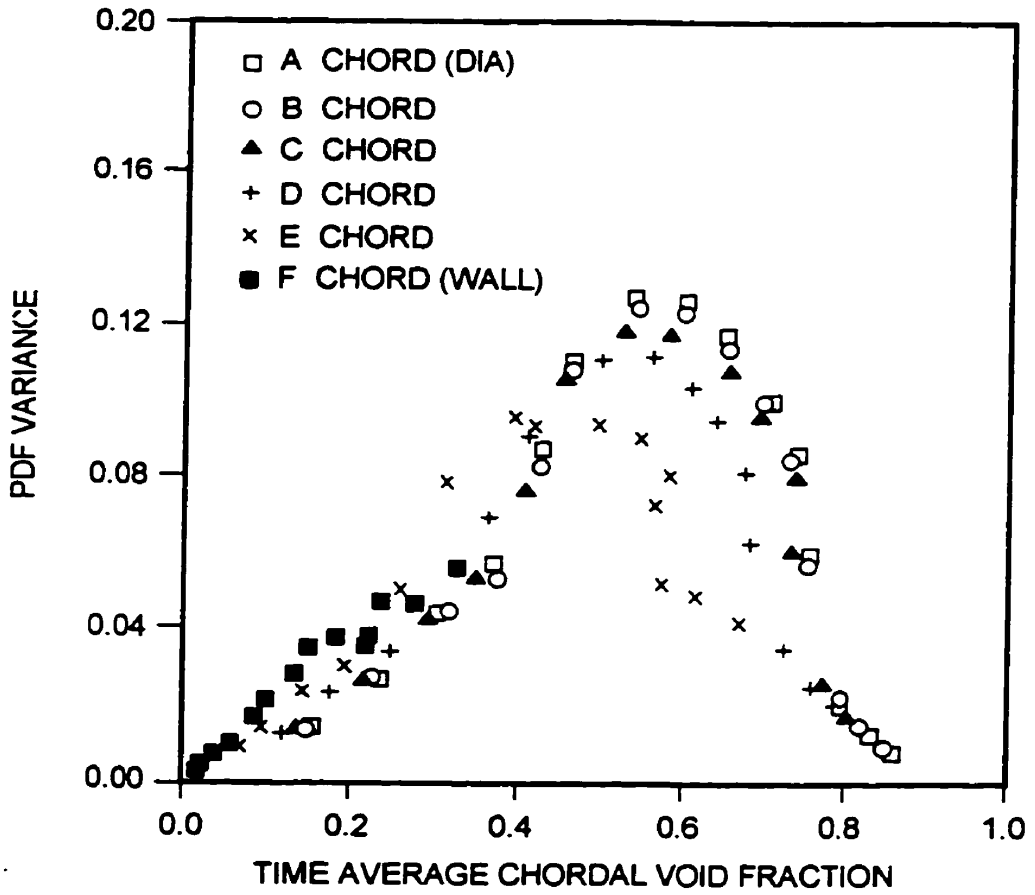

Figure 1.3: Variance as a function of void fraction (Vince & Lahey 1982).

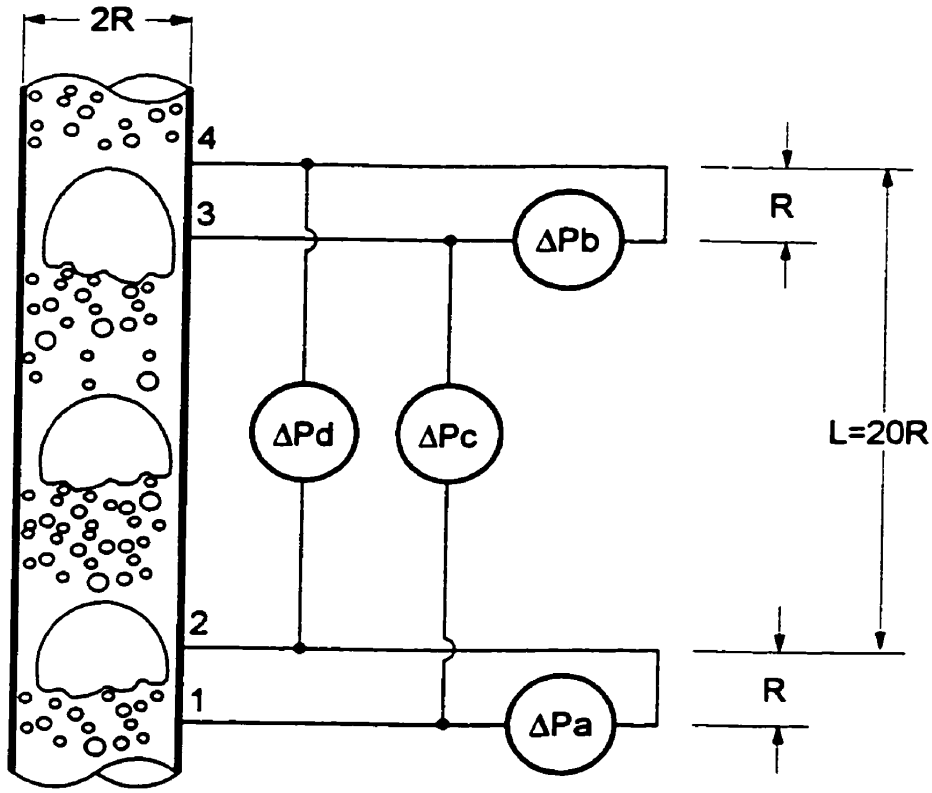

ΔPa , ΔPb : *R - scale*

ΔPc , ΔPd : *L - scale*

Figure 1.4: Differential pressure measurement (Matsui, 1986).

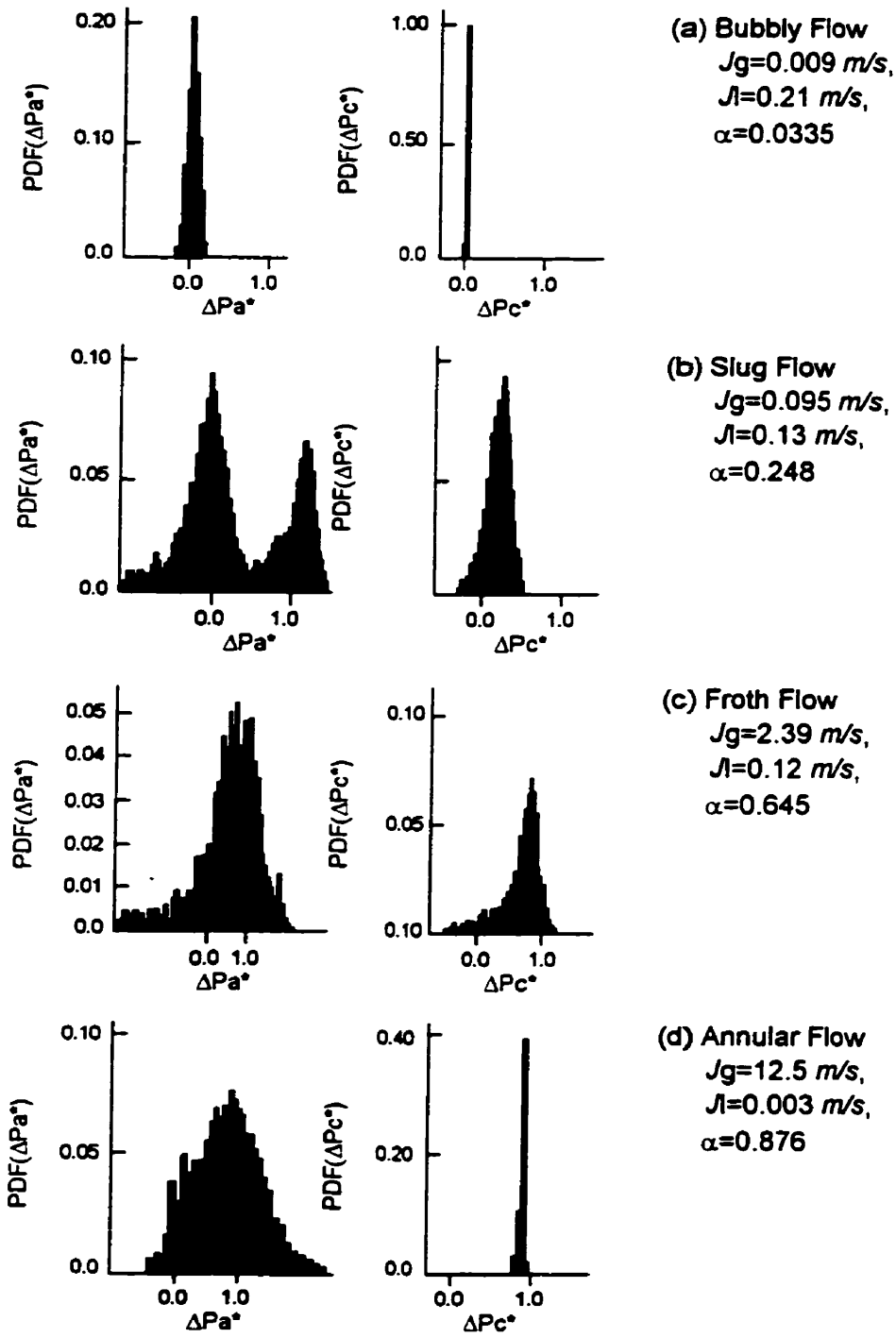

Figure 1.5: PDF of pressure signals (Matsui, 1986).

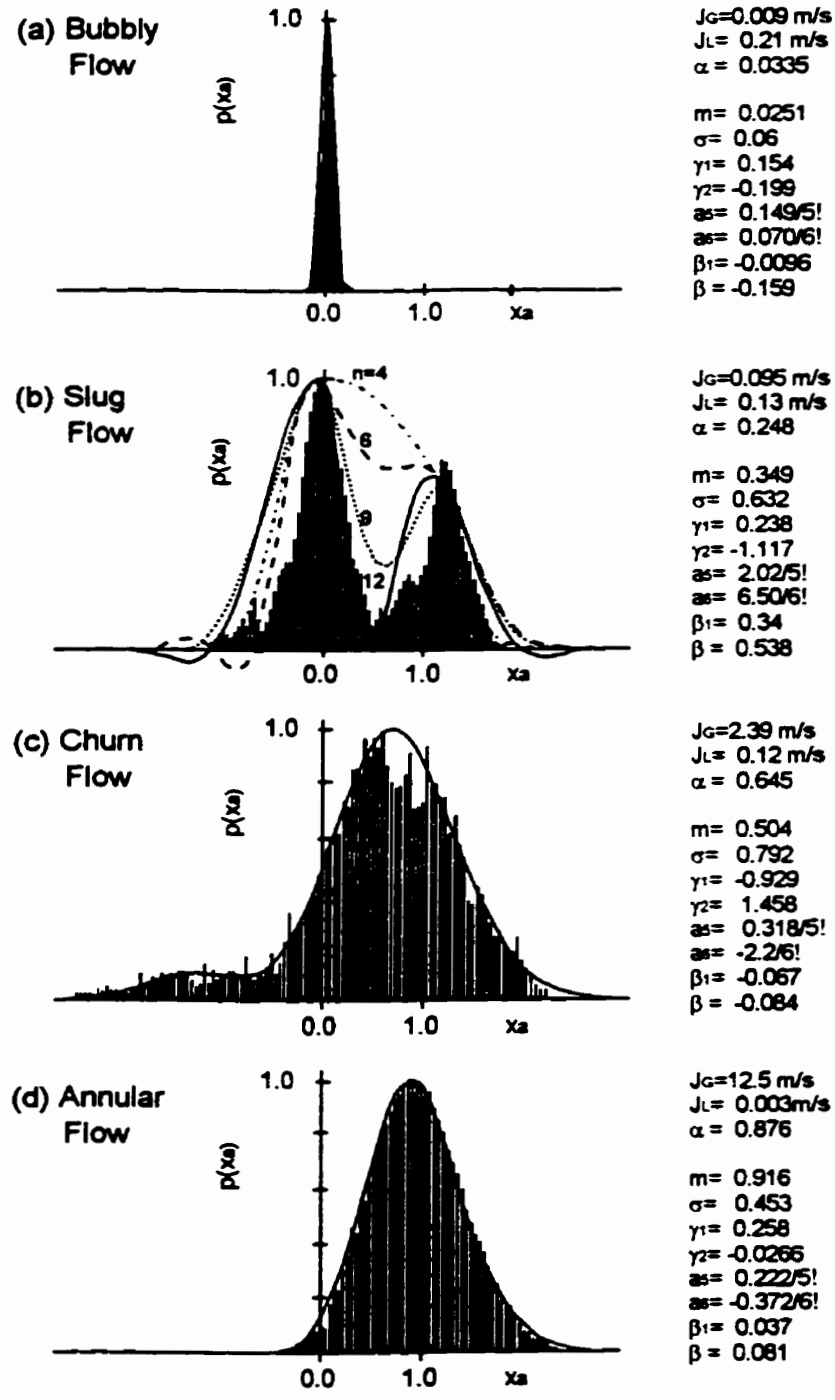

Figure 1.6: Curve fitting of PDF of pressure signals (Matsui, 1986).

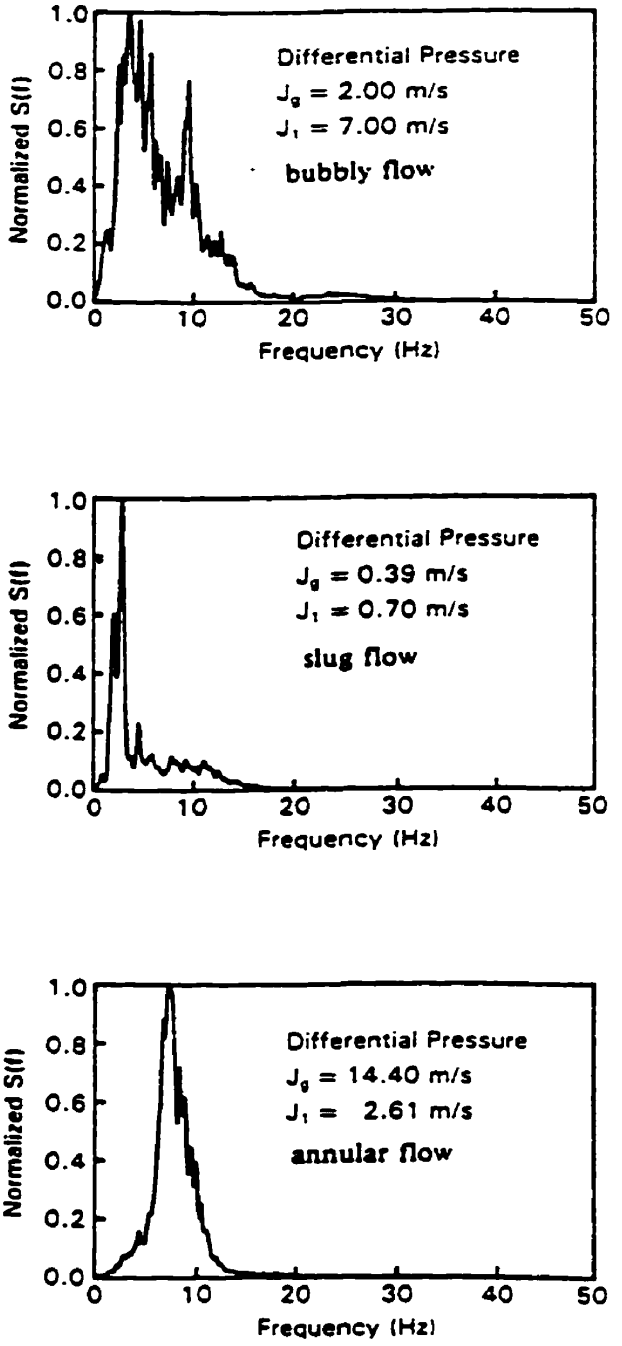

Figure 1.7: ARMA spectrum of King *et al.* (1988).

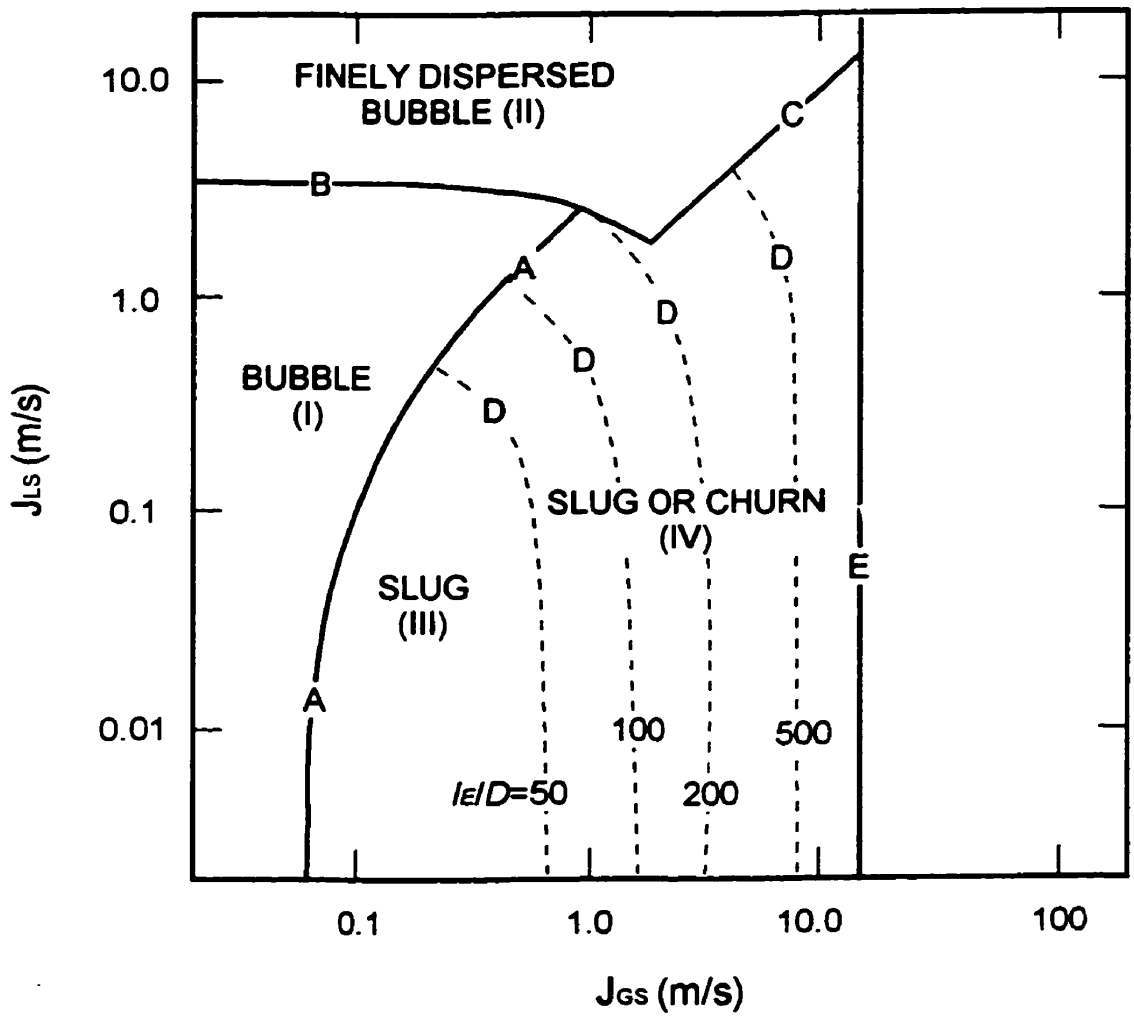

Figure 1.8: Flow pattern map based on theoretical prediction (Taitel *et al.* 1980).

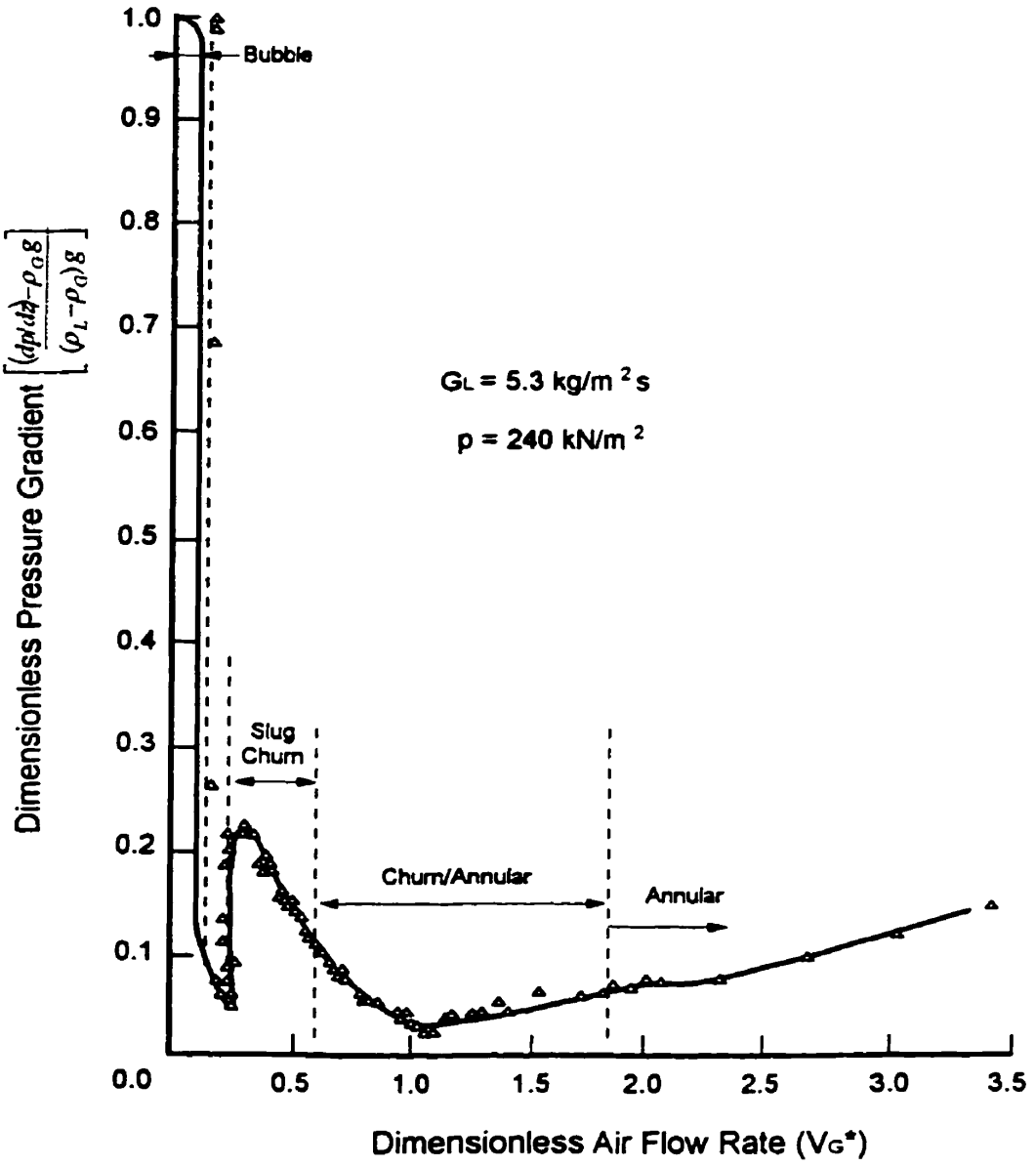

Figure 1.9: Pressure gradient in upward two–phase flow at low liquid flowrate (Govan *et al.* 1991).

Chapter 2

Experimental Apparatus and Instrumentation

In our study, the experiments for two–phase flow pattern identification were carried out in a vertical test section. The fluctuating signals of the void fraction and the differential pressure were measured to perform the statistical analysis. Important flow variables, such as gas and liquid flow rates and the absolute pressure in the test section were also measured. In this chapter, the experimental facility and the instrumentation used to carry out the experiments are presented.

2.1 Experimental Facility

The experimental apparatus used in this study is shown in Figure 2.1. The test section consisted of a 2 m long square channel having a cross sectional area of 161.3 mm^2. In order to permit the visual observation of the flow in the tube, the test section was made of a transparent acrylic material.

The experiments were carried out using an air–water mixture as the working fluid close to the atmospheric conditions. The water is supplied to the channel by a pump connected to a constant head water tank. A temperature sensor is immerged in the water tank to monitor the temperature. The temperature of the water is maintained constant at 20±0.5°C during the experiments. A flow calming tank is used to eliminate possible fluctuations due to the impeller of the pump. The inlet water flowrate is controlled by a valve located in the main feeder line and by a bypass valve. The inlet flowrates are measured by turbine flow meters with an accuracy of ±1% of the readings. The air is supplied from the mains of the laboratory and regulated by a relieving type regulator. The air flowrate was measured using "Brooks" rotameters with an accuracy of ±1% of the full range. In order to cover a wide range of flow rates , a set of three rotameters were used.

Ten pairs of void gauges and three pressure transducers are connected to the test sention. The signals produced by the void gauges and the pressure measurement system are collected by a data acquisition system (DAS). In order to eliminate any possible aliasing effects that may arise due to the using of the DAS, low pass filters are used to filter the signals.

A Hewlett Packard Analyzer is also connected to one pair of void gauges to get online PDF information on the flow structures.

At the outlet of the test section, the two–phase mixture flows into an air–water separator open to the atmosphere. The water level in the separator is kept constant.

2.2 Instrumentation

The instrumentation used to carry out the experiments will now be presented.

2.2.1 Liquid Flowmeter

Turbine flowmeters are used to measure the inlet water flowrates. The arrangement of the flowmeters having different ranges is shown in Figure 2.2.

According to the specifications of the manufacturer, the accuracy of the flowmeters is better than 1% of the reading, this feature is also confirmed by our calibration test performed by weighing the outlet flow of the water. Details on the range of the flow meters used to carry out the measurements are given in Table 2.1. The flowmeter with a desirable range can be chosen by openning the appropriate valves (see Figure 3.3).

Table 2.1: Liquid flowmeter parameters.

Flowmeter #(S/N)	Measuring Range (m^3/h)	Precision (%Readings)
1206612	0.451-4.735	1
120118	0.277-2.844	1

2.2.2 Gas Flowmeter

A set of three "Brooks" rotameters is used to measure the inlet air flowrates. The maximum range of the rotameters is 5.4 $scfm$ (m^3/h). These rotameters have been calibrated with an accuracy of 1% of full-scale. For a give run, the pressure of the air at the outlet of the rotameters is kept constant. It should be mentioned that the rotameters have been calibrated at a pressure of 2.07 bar (30 $psig$), therefore, a correction is necessary if the pressure differs from the value given by the manufacturer. This correction is carried out according to:

$$Q_g^{inlet} = Q_g^{meter} * 1.699 * (0.638 + 0.01307 * P_g - 0.00003548 * P_g^2), \qquad (2.1)$$

where, Q_g^{meter} is the air flowrate in $scfm$ read directly from the rotameters, P_g is the pressure in $psig$ at the outlet of the rotameters, Q_g^{inlet} is the air flowrate in m^3/h at the inlet of the test section.

In order to determine the volumetric flow rate of the gas phase in the test section, it is necessary take into account the effect due to the local absolute pressure. Assuming that the air behaves as an ideal gas and that the temperature is constant during the experiments, then we can write:

$$Q_g = Q_g^{inlet} * 101325(Pa)/P_A, \qquad (2.2)$$

where, P_A is the absolute pressure in Pa close to the center of the test section; Q_g is the gas flowrate in m^3/h in the test section.

2.2.3 Void Fraction Gauges

Several techniques have been developed for the measurement of void fraction. The application of each technique is normally limited to a specific problem. In general, all the existing methods can be classified into local measurement and spatially averaged measurement.

The local method, such as conductivity probes, film anemometers and optical fiber probes can give detailed information on phase distribution. However, these probes have the disadvantage of causing substantial perturbations in the flow patterns, especially when they are used with channels having relatively small flow area.

The average void fraction on a surface is generally measured by the absorption of X–rays or γ–rays. However, this measurement requires complex and expensive equipment. The volume averaged void fraction is usually measured by quick closing valves or by impedance gauges. Quick closing valves can not provide a continuous measurement of the void fraction. This method is usually used to calibrate other void fraction measurement techniques in the laboratory. The technique of neutron absorption or scattering becomes a powerful and sensitive way of measuring the volume averaged void fraction especially when gas-liquid mixture flows in a metallic pipe with thick walls.

The impedance technique is used for our study. With the impedance gauges, the void fractions at different axial locations can be quickly, continuously and simultaneously measured. Direct reading and a relatively low degree of uncertainty in the void

fraction determination are also advantages of impedance technique. The impedance gauges require calibration before their use. They have, however, relatively poor accuracy at high void fraction (80% and more). Their response depends strongly on the temperature and the impurity of the water.

In our experiments, the void fraction is measured by ten pairs of void gauges mounted along the test section. The signals are obtained by measuring the admittance between two parallel plate. The void fraction measurement system was manufactured by Auburn International Inc. Each pair of electrodes is connected to its own electric circuit and monitors the liquid fraction between the electrode plates. All the void gauges may be simultaneously monitored in real time or in an averaging cycle, if desired. In order to overcome the disadvantage of the response dependency on the temperature and the purity of the water, a separate reference channel is connected to continuously monitor the admittance of the inlet water. The response of the main channels is then divided by the response of the reference channel and the errors caused by the change of the temperature and the purity are thus reduced.

It must be pointed out that the reading of the void gauges represents the liquid portion in the two–phase mixture. When the test section is full of water, i.e., the void fraction of the mixture is zero, the reading of the void gauge is at the full range. When the test section is empty of water, i.e., the void fraction is one, the reading of the void gauge is zero. Therefore, in order to get the value of the void fraction in the test section, the following correlation should be used:

$$E_n = 1 - E'_n / E'_{n0},$$

$$n = 1, 2, \ldots, 10, \tag{2.3}$$

where, $E'_n(n = 1, 2, ..., 10)$ is the reading of the void gauges, $E'_{n0}(n = 1, 2, ..., 10)$ is the reading of the void gauges when the test section is full of water, and E_n is the normalized reading of the void gauges.

2.2.4 Pressure Transducers

The Figure 2.3 shows the details of the pressure measurement system. In order to determine the gas flowrate and hence the superficial gas velocity in the test section, the absolute pressure is measured close to the middle of the test section using a $1.7 \pm 0.25\%$ *bar* ($25 \pm 0.25\%$ *psig*) "Sensotec" pressure transducer, c1.

The fluctuating differential pressure is measured using a $689.5 \pm 0.25\%$ *Pa* ($0.1 \pm 0.25\%$*psid*) "Validyne" differential pressure transducer (c4 in Figure 2.3). The axial distance between the pressure taps is 19 *mm*. This distance is chosen in order to obtain the necessary information from the instantaneous signals for further statistical analysis. The connections between the pressure transducer and the pressure taps are made using short lengths of capillary copper tubes. To avoid the damage of the differential pressure transducer (c4) caused by over-scale measurement, a $1.4 \pm 0.25\%$ *bar* ($2.0 \pm 0.25\%$ *psid*) "Sensotec" differential pressure transducer (c3) is used to measure the differential pressure before opening the valves installed on the lines of pressure transducer c4.

The two–phase frictional pressure drop is also determined from separate measure-

ments using a $0.7 \pm 0.25\%$ *bar* $10 \pm 0.25\%$ *psid* differential pressure transducer (c2 in Figure 2.3).

The specifications of the pressure transducers are shown in Table 2.2.

Table 2.2: Pressure transducer parameters.

Pressure Transducer #	Measuring Range +/-	Output (Volts)	Precision (% Full Range)
c1	50.0*psig*	5.0030	0.25
c2	10.0*psid*	5.0040	0.25
c3	0.5*psid*	5.0013	0.25
c4	0.1*psid*	10.0100	0.25

The absolute pressure, P_A, in the test section is given by:

$$P_A = P_R * C * 6895 + 101325, \tag{2.4}$$

$$C = Range/Output,$$

where, P_R is the response of the pressure transducer, c1, in $Volts$, C is a constant, it represents the conversion of the output from $Volts$ to *psi*, the "*Range*" represents the transducer measuring range in *psi* and the " *Output*" represents the output in $Volts$ corresponding to full scale, see Table 2.2.

The differential pressures are determined by the direct reading of the transducer corrected by the water column in the pressure lines:

$$\Delta p = \Delta p_R * C * 6895 + \rho_l g \Delta z, \tag{2.5}$$

where, Δz is the distance between the two pressure taps which are connected to a differential pressure transducer, ρ_l is the water density at room temperature, g is the

acceleration of the gravity, Δp_R is the reading of the differential pressure in $Volts$ from the transducer and Δp is the differential pressure in Pa in the test section.

2.2.5 Data Acquisition System

The readings of the void fractions, the differential pressure, the absolute pressure and the liquid flowrate were simultaneously collected by a data acquisition system. The selection of the sampling time is an important step for correctly detecting the signals without eliminating their characteristic features. In general, the instantaneous characteristics of the signals may be lost when the sampling time is too long, while the aliasing problem on the signals may be increased when the sampling time is too short. According to the Nyquist criterion for data sampling, a minimum sampling rate is required which is twice the highest frequency component of the signals we are interested in. However, a sampling frequency which is around two–to–five times the highest component is recommended by Sekoguchi *et al.* (1987) and Elkow & Rezkallah (1997) for two–phase flow pattern identification. Now the problem is to determine the highest frequency component to correctly represent the phenomenon. In our study, previous observations have shown that the highest component of the void fraction and differential pressure signals were about 18 Hz. Thus, a sampling time of 15 ms is selected. In order to eliminate any possible aliasing effect, the signals are also filtered by low pass filters. Furthermore, in order to ensure a good statistical representation a collection of 4096 points are used to perform the FFT analysis.

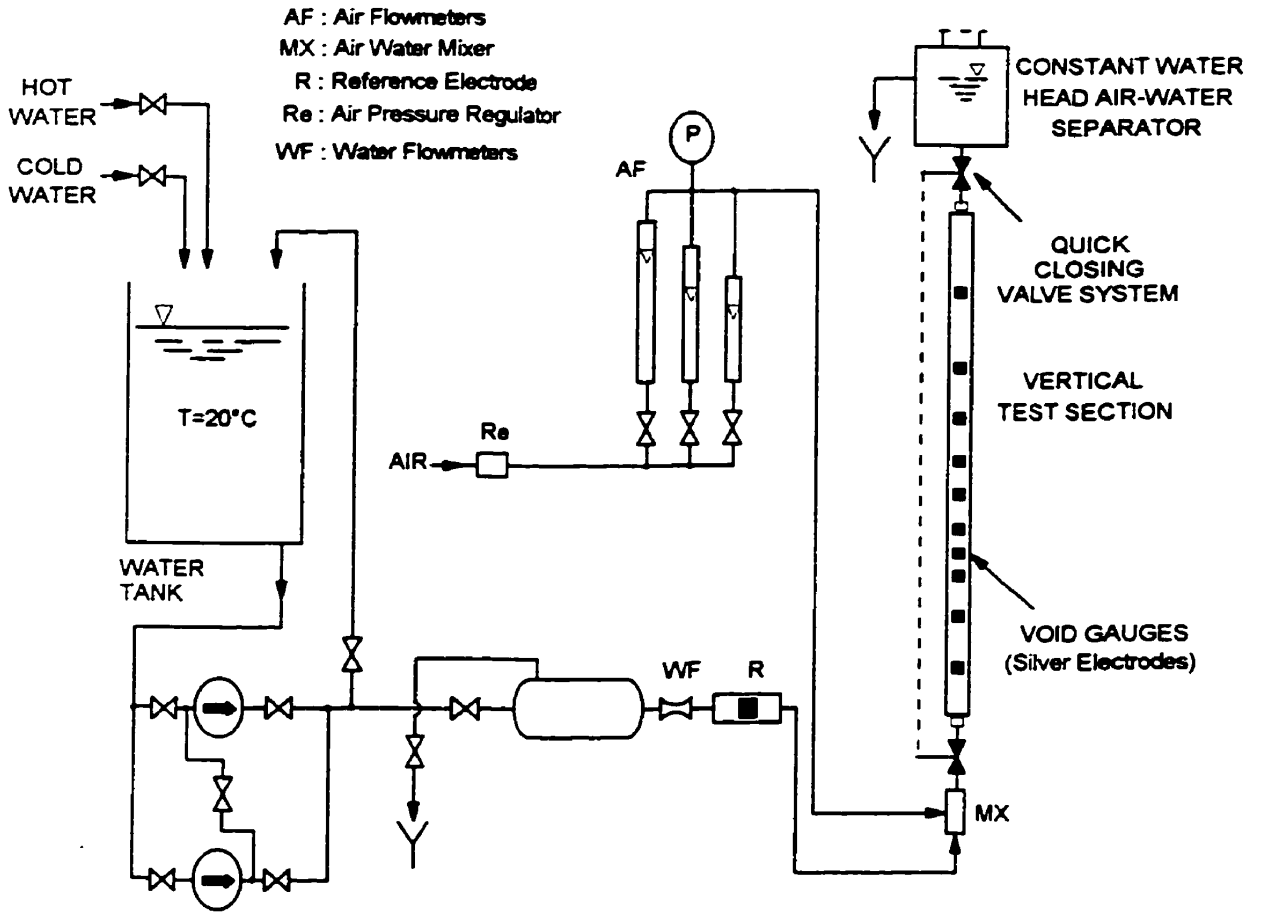

Figure 2.1: Experimental apparatus.

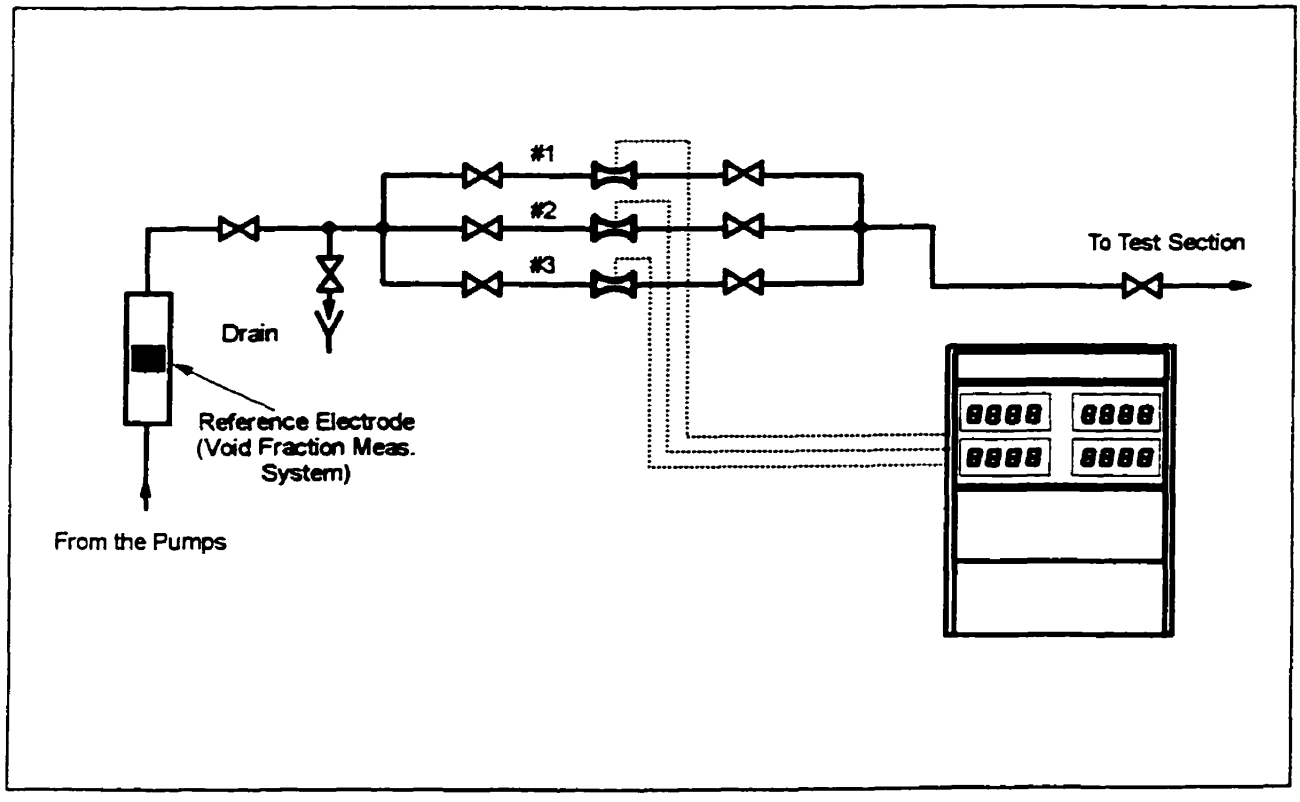

Figure 2.2: Arrangement of the liquid flowmeters.

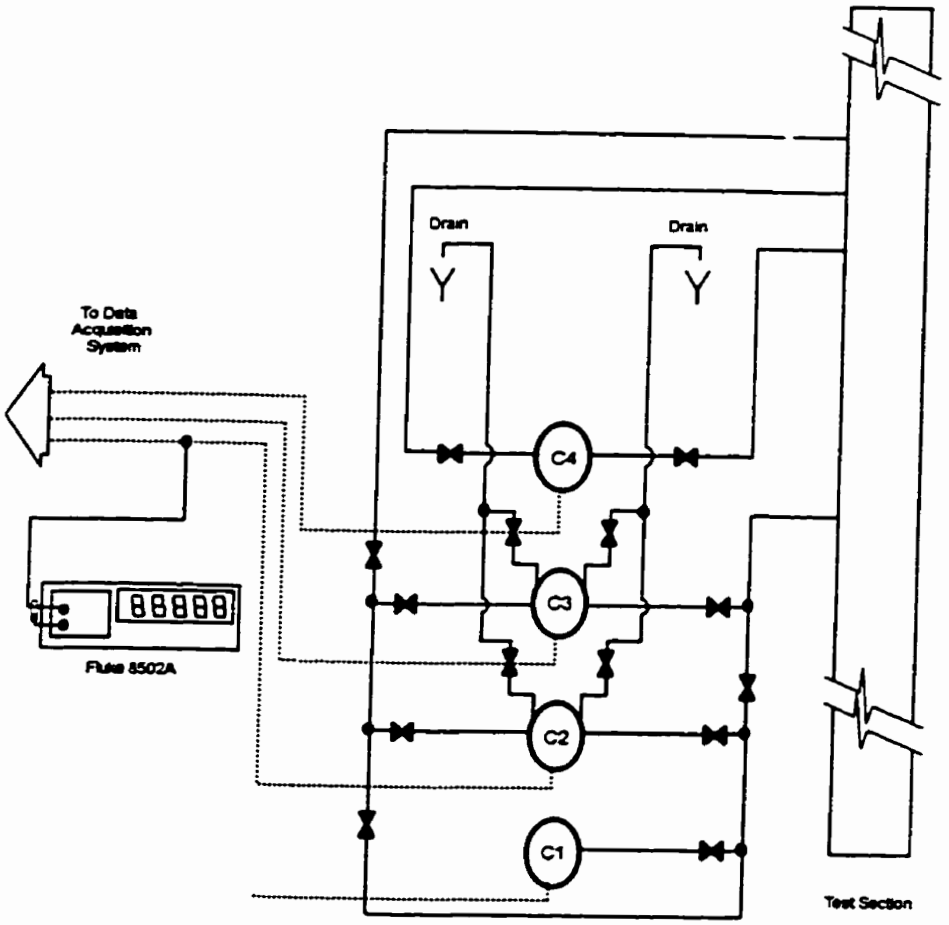

Figure 2.3: Arrangement of the pressure transducers.

Chapter 3

Experimental Procedures

The experiments were carried out in two different stages. In the first stage, the calibration of the impedance void gauges and the determination of the frictional pressure loss under both single– and two–phase flow conditions were obtained. In the second stage, the measurements of void fraction and differential pressure were carried out. These data were then analyzed using PDF and PSDF for flow pattern identification.

3.1 Calibration Experiments

3.1.1 Calibration of the Void Gauges

Ten pairs of impedance void gauges which are located at different axial positions were simultaneously calibrated using the Quick Closing Valve (QCV) technique.

During the experiments, for a given liquid mass flux, different void fractions in the

test section were obtained by changing the inlet gas flow rate. The void fraction was measured by ten pairs of void gauges. The void fraction was also determined using QCV by measuring the volume of the water in the channel after quickly and simultaneously closing ball valves mounted at both ends of the test section. The sampling time of the instantaneous electrical signals of void gauges was 50 ms. The total number of data points collected for each channel in each run is 870. The experiments were done for three ranges of liquid mass fluxes. These are 1000 kg/m^2s, 1500 kg/m^2s and 2000 kg/m^2s. The temperature was maintained almost constant around 20 $\pm$ 0.5°C during the calibration experiments.

3.1.2 Single–Phase Frictional Pressure Loss

Experiments were carried out to determined the single–phase frictional pressure loss. The single–phase friction factor was determined as a function of Reynolds number. According to Darcy's formulae, the single–phase frictional pressure drop is calculated as:

$$\frac{\Delta p_{f,1p}}{\Delta z} = \frac{1}{2} f \frac{G_l^2}{\rho_l} \frac{1}{D_h}, \tag{3.1}$$

where,

$\Delta p_{f,1p}$ = single–phase friction pressure drop,

D_h = hydraulic diameter (0.0127 m),

f = friction factor,

G_l = liquid mass flux (kg/m^2s),

ρ_l = liquid phase density (kg/m^3).

The friction factor, f, depends on the liquid velocity and the roughness of the inner surface of the test section. It is generally correlated as a function of Reynolds number. The friction factor can be determined from the measurements of liquid flowrate and the pressure drop over the test section.

The frictional pressure loss, $\Delta p_{f,1p}$, with reference to Equation 2.5, can be determined as follows:

$$\Delta p_{f,1p} = \Delta p - \rho_l g \Delta z.$$

3.1.3 Two–Phase Flow Multiplier

The two–phase pressure drop is an important parameter in the design of two phase systems. The total pressure drop in two–phase flow consists of the following three parts: pressure drop due to acceleration, Δp_a, frictional pressure drop, Δp_f and gravitational pressure drop, Δp_g. Hence:

$$\Delta p = \Delta p_a + \Delta p_f + \Delta p_g. \tag{3.2}$$

When the void fraction is known, then the gravitational pressure drop can be obtained by:

$$\Delta p_g = g \Delta z (\alpha \rho_g + (1 - \alpha)\rho_l), \tag{3.3}$$

where, ρ_g and ρ_l are the gas and liquid phase densities, respectively, and α is the void fraction.

The two–phase frictional pressure drop, Δp_f, can not be directly measured. The experimental data provide only the values of the total pressure drop. The frictional

pressure drop can be experimentally determined by subtracting the gravitational and the acceleration pressure drops from the total measured pressure drop. In general, the two–phase frictional pressure drop is determined from the following relationship:

$$(\frac{\Delta p}{\Delta z})_{f,2p} = \phi_{l0}^2 (\frac{\Delta p}{\Delta z})_{f,1p}, \tag{3.4}$$

where, $(\frac{\Delta p}{\Delta z})_{f,2p}$ is the two–phase frictional pressure gradient, $(\frac{\Delta p}{\Delta z})_{f,1p}$ is the single–phase frictional pressure gradient when only the liquid phase flows in the test section and ϕ_{l0}^2 is two–phase multiplier. The two–phase multiplier indicates the manner in which the two–phase frictional pressure drop is greater than the single–phase frictional pressure drop.

In our study, the two–phase multiplier is determined experimentally using values of $(\frac{\Delta p}{\Delta z})_{f,2p}$ and $(\frac{\Delta p}{\Delta z})_{f,1p}$. It should be pointed out that the acceleration pressure drop Δp_a, which is due to the void fraction changes in the two–phase flow, is neglected, since the distance, Δz, over which the total pressure drop is measured is very small and the void fraction is assumed to remain unchanged within this distance. Hence:

$$\Delta p_a = 0. \tag{3.5}$$

Combining Equation 3.2 and Equation 3.3 , yields:

$$(\frac{\Delta p}{\Delta z})_{f,2p} = \frac{\Delta p}{\Delta z} - g(\alpha \rho_g + (1-\alpha)\rho_l). \tag{3.6}$$

The single–phase frictional pressure gradient, $(\frac{\Delta p}{\Delta z})_{f,1p}$, is calculated using the Darcy relationship (Equation 3.1). The single–phase friction factor, f, is determined experimentally from single–phase experiments and correlated in term of the Reynolds number.

3.2 Fluctuating Component of Pressure and Void Fraction Signals

Two–phase flows are characterized by fluctuating characteristics of the void and pressure signals. The features of the fluctuating signals of void fraction and differential pressure depend strongly on flow patterns. A very important step for flow pattern identification in our study is to obtain the fluctuating components of the signals of void fraction and differential pressure.

In order to cover all possible two–phase flow configurations, the experiments are carried out under the following inlet conditions: liquid mass fluxes of 1000 kg/m^2s, 1500 kg/m^2s and 2000 kg/m^2s; gas flow from 0.0 m^3/h to 9.175 m^3/h. The average void fraction in the region where the pressure differences are measured ranges from 0% to 80%. Important flow regimes such as bubble, slug, churn and annular flows are covered in this work.

The differential transducer, c4, of 0.1 *psid* as shown in Figure 2.3, is used to measure the instantaneous pressure drop. This transducer is sensitive enough to capture the characteristic features of the pressure fluctuations. As shown in this figure, the distance between the pressure taps is 19 mm. This distance was chosen after several trial experiments. If the distance is too large, the fluctuating features of the pressure are not sensitive to flow patterns. Thus the reading only represent the averaged statistical features of the flow. If the distance is too small, the signal–to–noise ratio of the measurement may decrease and the results of the analysis may be distorted.

For the analysis of the void fraction, the instantaneous signals of void gauge #8 were used, because this void gauge is located close to the pressure taps where transducer c4 is connected. The statistical features of the signals from void gauge #8 can be compared with those obtained from pressure transducer C4.

For a given set of experimental conditions, i.e., fixed gas and liquid flow rates, the instantaneous signals of the void fraction, the differential pressure, the absolute pressure and the liquid flowrate were collected simultaneously by programming the data acquisition system. The sampling time is 15 ms and the total number of samples that form a record is 4096 points.

Chapter 4

Experimental Results

The result of the calibration experiments are presented in this chapter. The relationship of some important two–phase flow parameters, such as the volumetric flow quality, flow quality and slip ratio, with the void fraction are also presented. The result of flow pattern classification of the experimental data has been compared with Taitel's flow pattern map (1980).

4.1 Calibration Results

The results of the calibration experiments for void gauge #8 are shown in Figure 4.1. From the calibration curves, it can be seen that void fractions up to 80% can be measured reliably. It can also be seen that the calibration curves of the void fractions are not affected by liquid flowrate. Each calibration curve has also been fitted by a polynomial having the following form:

$$\alpha_n = c_0 + c_1 E_n + c_2 E_n^2 + ... + c_m E_n^m, \tag{4.1}$$

where, $n = 1, 2, ..., 10$, which denotes the number of the electrode, $m = 6$, which denotes the order of the polynomial. The coefficients of the polynomials used to fit the response of the void gauges are given in Table 4.1.

It should be pointed out that during the calibration of the void gauges, it was assumed that the void fraction was not affected by the local pressure in the test section. Thus the expansion of the gas caused by the local pressure was neglected. As a matter of fact, since the void fraction obtained with the QCV gives an average value, the actual void fraction near the inlet of the channel should be lower and that near the exit of the channel should be higher. However, in our experiments, the impedance void gauges are distributed vertically over a rather short distance and the pressure drop over this short distance is small when compared with the system operating pressure. Therefore, the effect of the pressure drop on the void fraction can be negligible.

The results of the calibration experiments for the single phase frictional factor as a function of Reynolds number are shown in Figure 4.2. It has been found that the following correlation yields the best fit to the results in the range of Reynolds number from 10000 to 80000.

$$f = 0.0032 + 0.221 Re^{-0.237}, \tag{4.2}$$

where, Re, is the Reynolds number which is given by:

$$Re = \frac{\rho_l V_l D_h}{\mu_l},$$

where, V_l, the liquid velocity and μ_l, the liquid viscosity.

The results obtained for the two-phase multiplier as a function of void fraction for

mass fluxes of 1000 kg/m^2s and 1500 kg/m^2s are shown in Figure 4.3.

The experimental data for the two–phase multiplier have been fitted with the following polynomials:

for $G_l = 1000\ kg/m^2s$,

$$\phi_l^2 = 1.0157 + 6.1124\alpha - 7.1317\alpha^2 + 5.8851\alpha^3 + 1.9831\alpha^4 + 38.9398\alpha^5,$$

for $G_l = 1500\ kg/m^2s$,

$$\phi_2^2 = 1.0023 + 6.2649\alpha - 24.7255\alpha^2 + 109.0478\alpha^3 - 222.7706\alpha^4 + 194.5431\alpha^5.$$

4.2 Two–Phase Volumetric Flow Quality, Flow Quality and Slip Ratio

In order to further understand the behavior of two–phase flow, other important two–phase flow parameters, such as the volumetric flow quality, flow quality and slip ratio, as a function of void fraction, are also determined from the experimental results. The aforementioned two–phase parameters are briefly described below.

The two–phase volumetric flow quality is defined as the volumetric flow rate of the gas phase, Q_g, divided by the total the volumetric flow rate, that is:

$$\beta = \frac{Q_g}{Q_g + Q_l}, \tag{4.3}$$

which can also be written in terms of the phase superficial velocities as:

$$\beta = \frac{J_g}{J_g + J_l}, \tag{4.4}$$

where, J_g is the gas superficial velocity, which is the velocity the gas phase would have if it flowed alone in the conduit and which is given by the following relationship:

$$J_g = \frac{Q_g}{A} = \frac{V_g}{\alpha},$$

where, V_g is the average gas velocity in the two–phase flow, A is the cross-section area of the conduit. J_l is the average liquid superficial velocity given by:

$$J_l = \frac{Q_l}{A} = (1 - \alpha)V_l,$$

where, V_l is the liquid velocity in the two–phase flow. For homogeneous flow, the value of the volumetric flow quality is the same as that of the void fraction.

The slip ratio represents the relative movement of the gas to the liquid phases:

$$S = \frac{V_g}{V_l}. \tag{4.5}$$

The flow quality is defined as the fraction of the gas mass flow rate W_g to the two–phase mixture mass flow rate $(W_g + W_l)$:

$$x = \frac{W_g}{W_g + W_l}. \tag{4.6}$$

The results of the volumetric flow quality, slip ratio, flow quality and gas superficial velocity (gas volumetric flux) as a function of void fraction are shown in Figures 4.4 to 4.7, respectively.

From Figure 4.4 for void fractions less than 30% the data points lie on the line $\alpha = \beta$. Furthermore, the data points for the slip ratio (Figure 4.5) are near unity, which indicates the existence of a homogeneous flow for this void fraction range.

Above a void fraction of 30%, the slip ratio is always greater than unity, indicating that the gas phase velocity is greater then that of the liquid phase.

Between the void fractions of 30% and 70%, the volumetric flow quality and the slip ratio increase with decreasing liquid flowrate at a given void fraction.

For void fractions greater than 70%, the results for the volumetric flow quality as a function of void fraction are independent of the mass flux for the two mass fluxes used in the current study.

Figure 4.6 and Figure 4.7 show that the flow quality and the volumetric flux of the gas phase (J_g) increase slowly with increasing void fraction up to a value of $\alpha = 50\%$ and more rapidly thereafter. Both of these quantities are affected by liquid flowrate.

4.3 Flow Pattern Comparison with Taitel's Map

In this study, two–phase flow patterns in a 0.0127 m (0.5 in) square test section are initially identified by direct visualization. The flow pattern identification map constructed by Taitel *et al* (1980) has been chosen to carry out a preliminary representation of the current data. The models proposed by Mishima & Ishii (1984) for predicting the bubbly–to–slug flow transition and by Brauner & Barnea (1986) for slug–to–churn flow transition for a 12.5 $mmI.D.$ tube have also been used for the comparison with our flow pattern identification results. For this purpose, the superficial velocities for both the liquid and gas phases are calculated. The absolute pressure measured at a location close to the differential pressure taps is used for determining

the gas velocity in the test section.

By comparing our experimental points with the aforementioned flow pattern identification models as shown in Figure 4.8, it has been observed that The bubbly flow regime extends somehow to the right of the bubbly-to-slug transition on Taitel's map, but the present results are close to the bubbly-to-slug transition given by Mishima & Ishii (1984). The slug flow points are also shifted to the right of the slug-to-churn transition curve of Taitel's map. The transition predicted from the slug-to-churn flooding mechanism model of by Brauner & Barnea (1986) also lies to the right side of the map of Taitel *et al* (1980). This shift has also been experimentally observed in a 12.5 *mm* tube by Shoham (1982) and in a 12.3 *mm* tube by Barnea, Luninski & Taitel (1983). The annular flows in our study took place somewhat earlier as compared to the churn-to-annular transition region on Taitel's map. Earlier transitions from churn to annular flow were also visually observed by Vince and Lahey (1982) in a 2.54 *cm* vertical tube.

It must be pointed out that two–phase flow patterns are inevitably dependent on the conduit geometry and flow conditions (Barnea 1987; Cheng, Hills & Azzorpardi 1998). Most efforts in the past have been devoted to the flow pattern identification in large diameter tubes and relatively low liquid flowrates, because typical flow patterns are easily obtained and visually detected under such conditions. Few experiments are reported on flow pattern identification in small diameter pipes. No flow pattern map for small square channels at high liquid flowrates has been reported. Thus, it is no surprise that our experimental points are not always consistent with the published

flow pattern maps.

Table 4.1: Polynomial coefficients for void gauges.

Electrode	*A1*	*A2*	*A3*	*A4*	*A6*
c_0	$6.8058e^{-5}$	$1.2746e^{-4}$	$4.7132e^{-4}$	$3.7426e^{-4}$	$1.047300e^{-3}$
c_1	0.452168	0.462556	0.501291	0.514883	0.486917
c_2	1.327281	1.174907	1.017780	1.014879	1.220287
c_3	-1.940089	-1.619715	-1.413596	-1.400820	-1.826144
c_4	1.162819	0.983850	0.893666	0.870050	1.113065
c_5	0	0	0	0	0
c_6	0	0	0	0	0

Polynomial coefficients for void gauges (continued).

Electrode	*A7*	*A8*	*A10*	*A11*	*A12*
c_0	$1.3903e^{-3}$	$1.9346e^{-3}$	$1.6098e^{-5}$	$1.6417e^{-3}$	$5.9056e^{-4}$
c_1	0.416000	0.321954	0.680413	0.546581	0.541683
c_2	1.558392	2.086974	-0.263163	0.469758	1.005382
c_3	-2.396573	-3.255641	0.063366	0.020923	-1.865385
c_4	1.412932	1.412932	5.186966	$5.7138e^{-3}$	1.208041
c_5	0	0	-10.303172	$7.3337e^{-3}$	0
c_6	0	0	5.633857	-0.015760	0

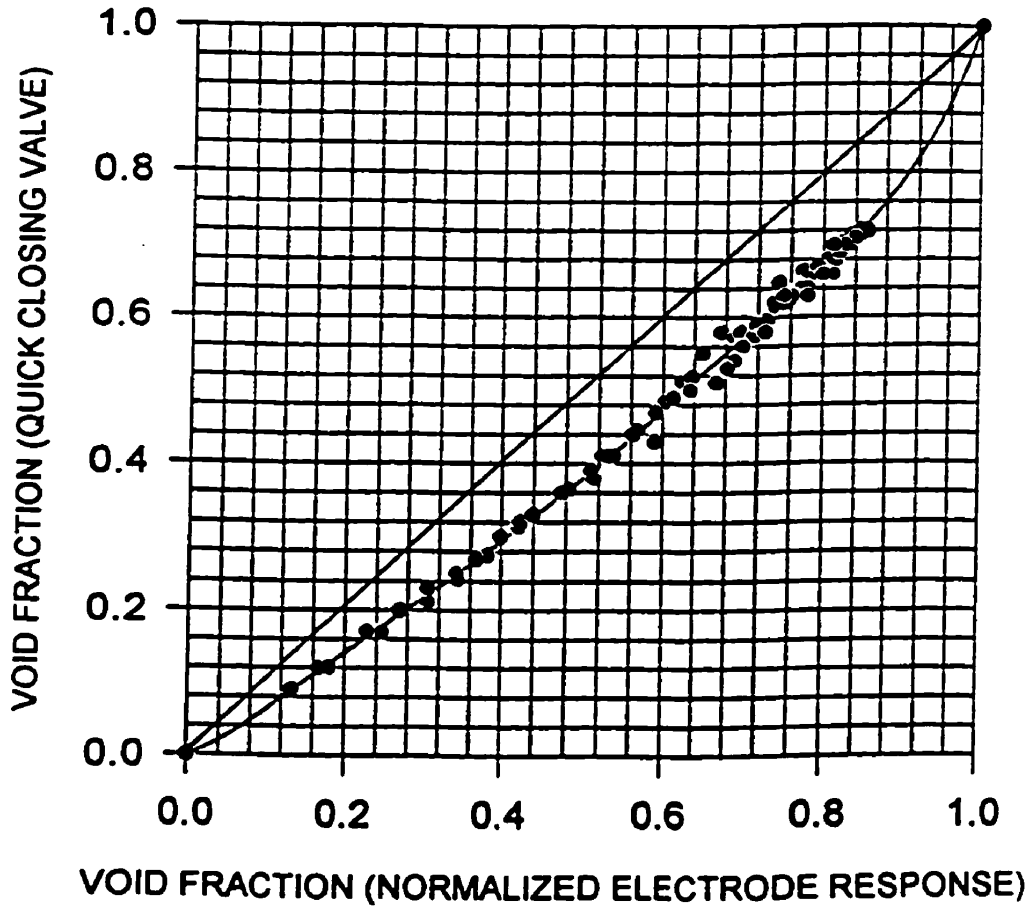

Figure 4.1: Calibration for void gauge #8.

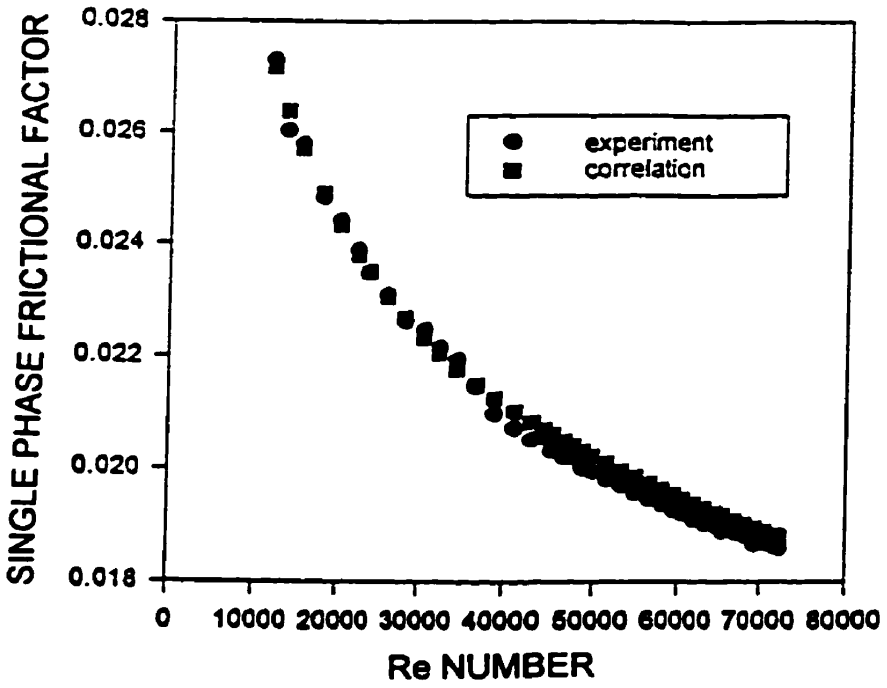

Figure 4.2: Single–phase frictional factor as a function of Renolds number.

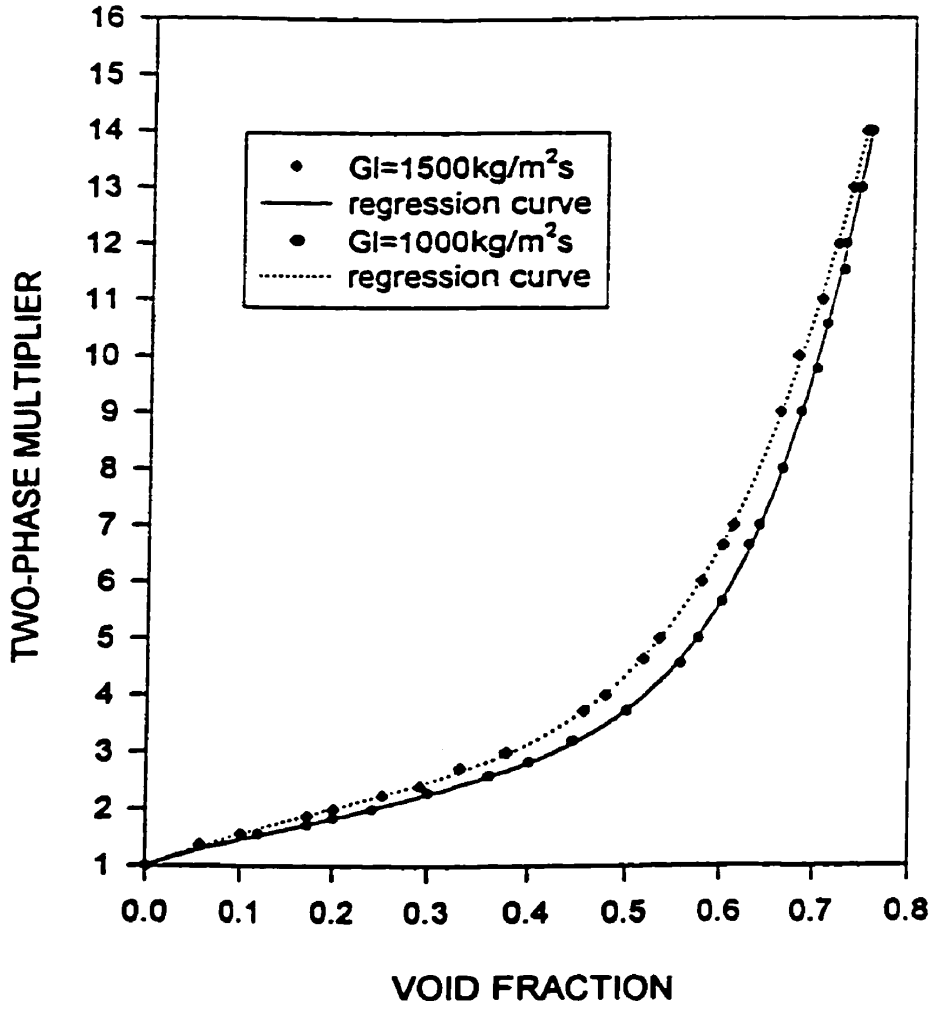

Figure 4.3: Two–phase multiplier as a function of void fraction.

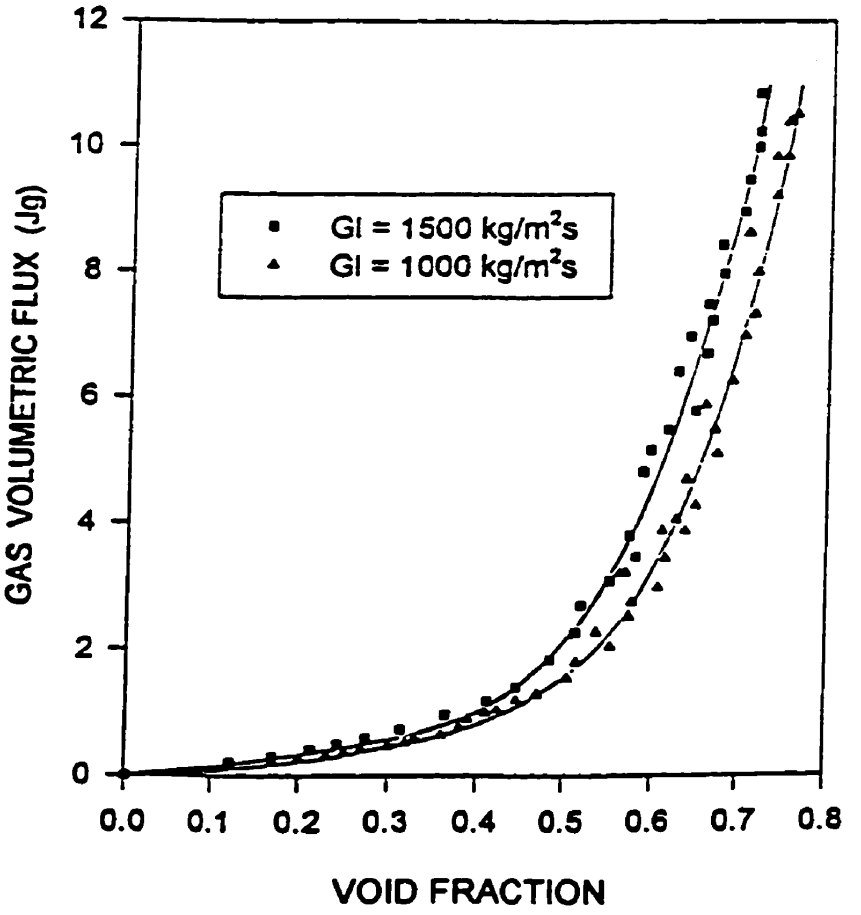

Figure 4.4: Two–phase volumetric flow quality as a function of void fraction.

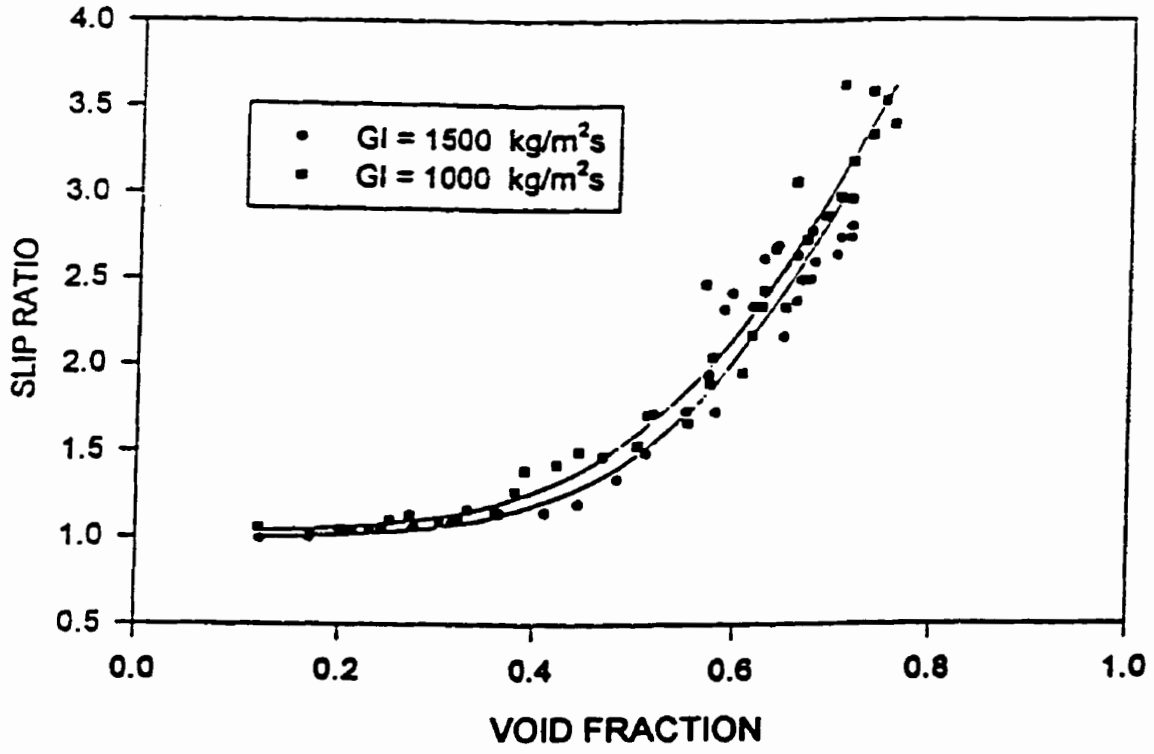

Figure 4.5: Two–phase slip ratio as a function of void fraction.

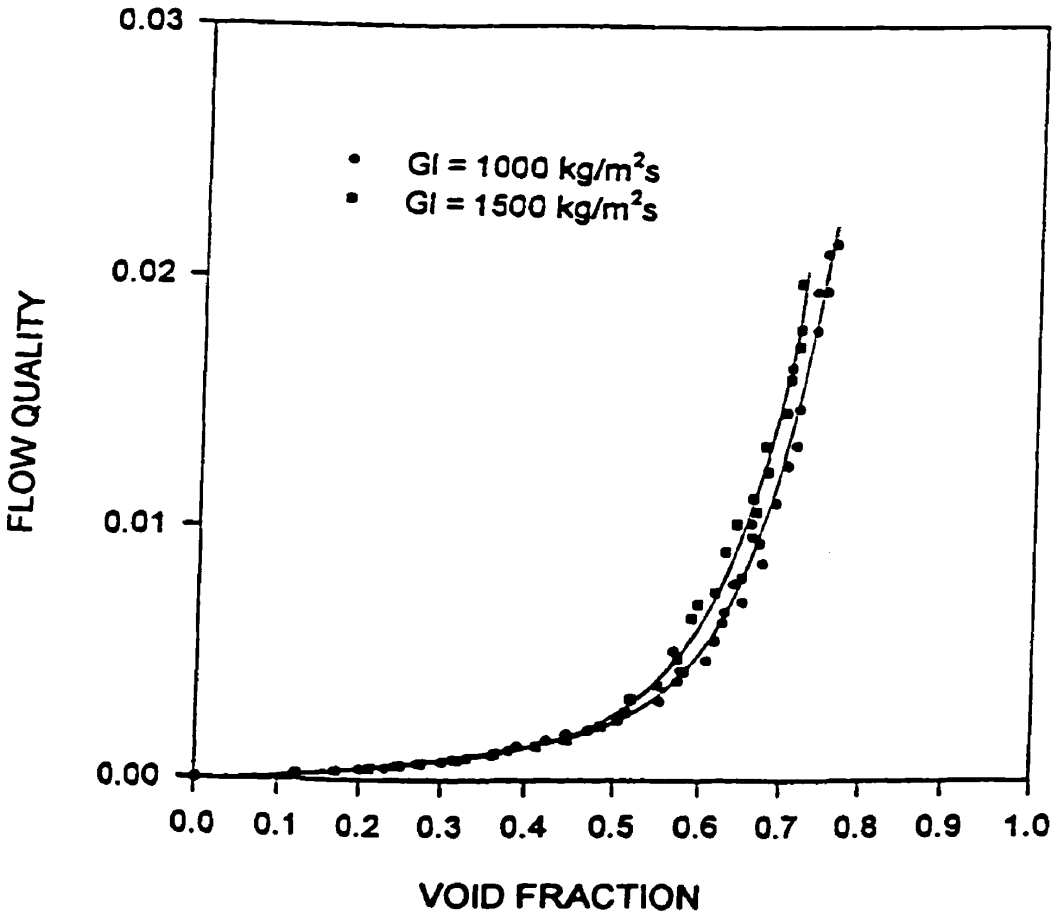

Figure 4.6: Two-phase flow quality as a function of void fraction.

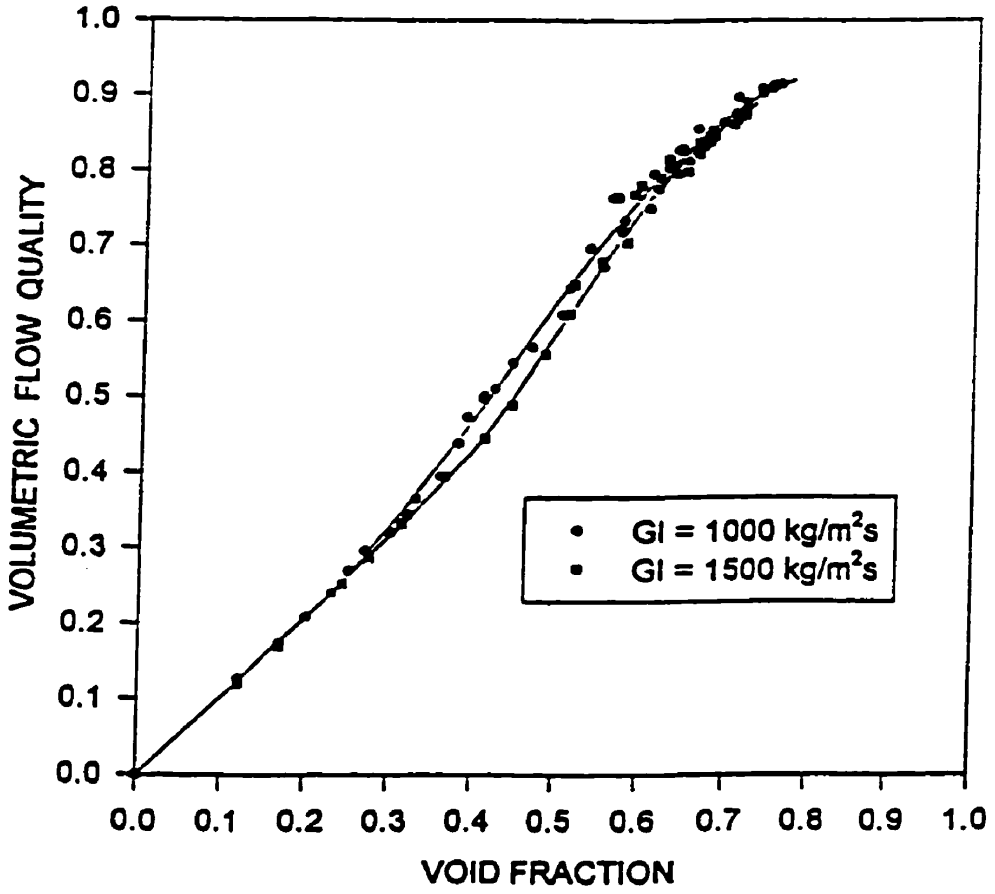

Figure 4.7: Two–phase gas volumetric flux as a function of void fraction.

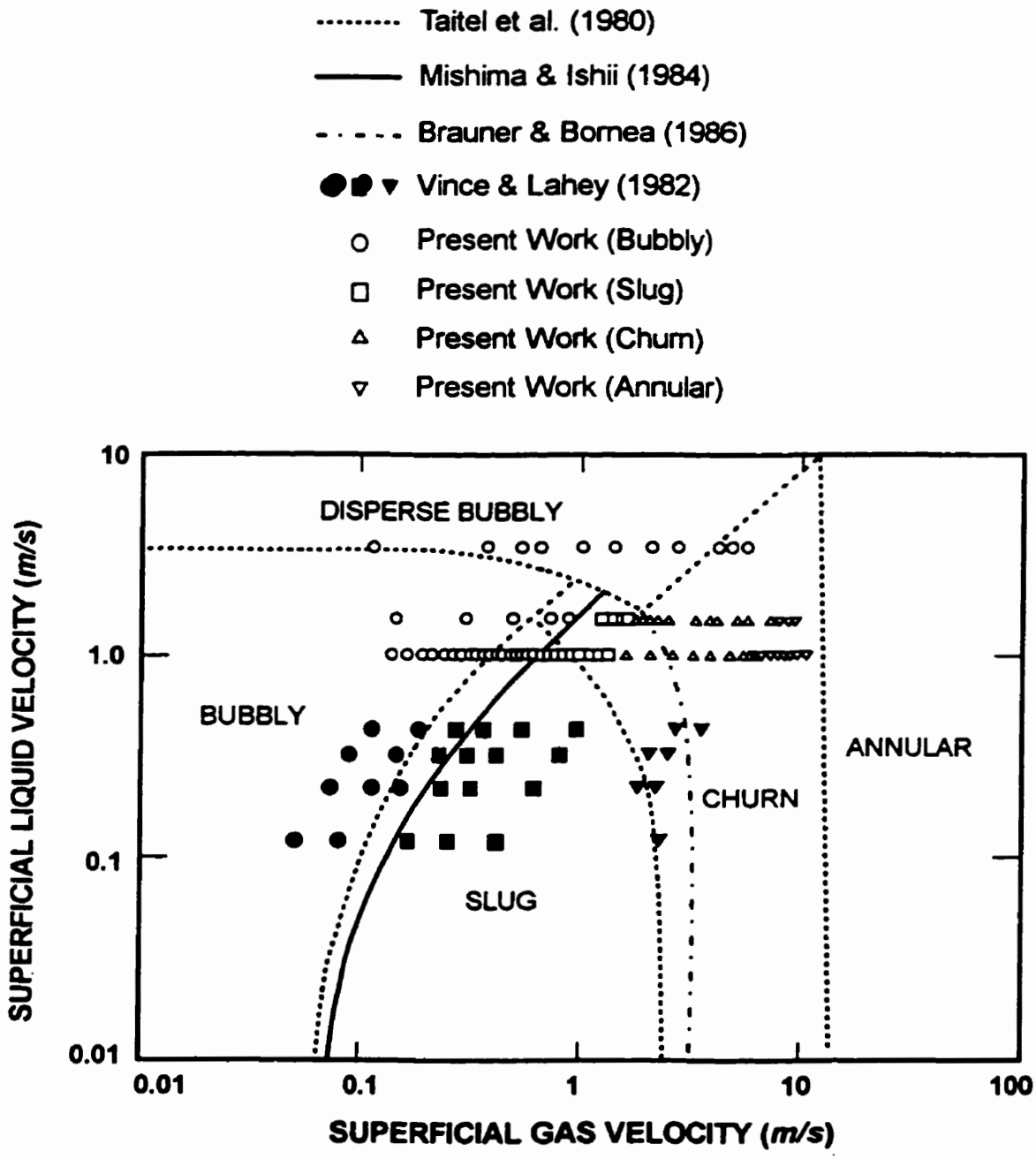

Figure 4.8: Flow pattern comparison with Taitel's map (1980).

Chapter 5

Statistical Analysis of Flow Pattern Identification Results

In this chapter, the results based on the statistical analysis of the signals of void fraction and pressure are presented. Important statistical moments as well as probability density function (PDF) and the power spectrum density function (PSDF) are employed to analyze the fluctuating signals of void fraction and differential pressure. It will be shown that the statistical results are strongly dependent on the flow patterns.

5.1 Statistical Assumption

Two–phase flow systems are characterized by the random variations in the values of the void fraction and the pressure. These values can not be predicted in advance. It is however possible to find the average value or the statistical property for the void fraction or the pressure. For example, during the experiments, we obtain a set of time records for a certain two–phase parameter (this parameter can be either the void

fraction or the pressure). These records are $x_1(t)$, $x_2(t)$, $x_3(t)$,...$x_N(t)$, as shown in Figure 5.1. The mean value (the first order average property) of the random process at an arbitrary time, t_1, can be computed by taking the instantaneous value of each time record at time t_1, summing the values and dividing by the number of the time records:

$$E(t_1) = \lim_{N\to\infty} \frac{1}{N} \sum_{i=1}^{N} x_i(t_1), \tag{5.1}$$

$$i = 1, 2, 3, ...N.$$

In the same way, we can also calculate the mean value of the random process at some other time $t_1 + \tau$:

$$E(t_1 + \tau) = \lim_{N\to\infty} \frac{1}{N} \sum_{i=1}^{N} x_i(t_1 + \tau). \tag{5.2}$$

If the mean value $E(t_1)$ is equal to $E(t_1 + \tau)$, then the random process is called stationary process.

We can also compute the mean value of any time record, $x_i(t), t = 1, 2, ..., T$:

$$\overline{x_i(t)} = \lim_{T\to\infty} \frac{1}{T} \sum_{i=1}^{T} x_i(t). \tag{5.3}$$

If the mean value of one time record $\overline{x_i(t)}$ is equal to an arbitrary ensemble mean value $E(t_1)$, then the random process is ergodic.

The ergodic consideration is very practical in statistical analysis. In such a case, the statistical analysis can be greatly simplified. The statistical analysis can then be applied to a single time record instead of the ensemble of records. In practice, one can usually design experiments that produce stationary and ergodic data, simply by maintaining steady experimental conditions. It must be noted that, in our study, all

the statistical analyses are based on the assumption that the two–phase fluctuating process is both stationary and ergodic.

5.2 Probability Density Function

Since two–phase flow is a random process, the precise value of the void fraction or the pressures at any chosen time cannot be precisely predicted. The best we can do is to find the chance, or probability, that the void fraction or the pressure at a given time will lie within certain limits. The subject of probability is, therefore, at the heart of random theory and the probability density function is an important statistical tool that has been frequently used for the analysis of random processes. Now let us consider a simple example in order to illustrate the statistical significance of the probability density function.

Suppose that we are dealing with a time history which is not random and is a sine wave, as shown in Figure 5.2. In this case we can exactly predict the value of x for any given value of t. We can therefore calculate the proportion of time that the waveform spends between any two levels of x. With reference to Figure 5.3, during one complete cycle, $x(t)$ lies in the band x to $x + dx$ for two periods of duration dt each. If $x = x_0 sin(\omega t)$, then $dx = x_0 \omega cos(\omega t) dt$, so that:

$$dt = \frac{dx}{x_0 \omega cos(\omega t)}. \tag{5.4}$$

Now substituting for $cos(\omega t) = \sqrt{1 - sin^2(\omega t)}$, we have:

$$dt = \frac{dx}{x_0 \omega \sqrt{1 - \frac{x^2}{x_0^2}}}. \tag{5.5}$$

The proportion of time per cycle that $x(t)$ spends in the band x to $x+dx$ is therefore:

$$\frac{dt}{T} = \frac{dx}{\omega T\sqrt{x_0^2 - x^2}}. \tag{5.6}$$

When setting $T = \frac{2\pi}{\omega}$, we have:

$$\frac{2(dt)}{T} = \frac{dx}{\pi\sqrt{x_0^2 - x^2}}. \tag{5.7}$$

For any complete number of cycles, Equation 5.7 gives the proportion of the total elapsed time for which $x(t)$ lies within the x to $x + dx$ band.

Now consider a situation in which we have to choose an instant of time, $t = t_0$, and find the value of x at this instant. Since $x(t)$ is a deterministic sine wave, as soon as we specify t_0, we immediately know $x(t_0)$. But suppose that t_0 is not precisely specified. Instead we are just told that it may lie anywhere along the time axis. In this case we cannot say what $x(t_0)$ will be; the best we can do is to predict what it may be. If t_0 is chosen perfectly arbitrarily, t_0 may lie anywhere during a complete cycle (the record is assumed to exist for ever with no beginning and no ending so that there is no question of t_0 falling in an unfinished cycle). The chance or probability that $x(t_0)$ lies in the band x to $x + dx$ will then depend only on how long per cycle $x(t)$ lies between x and $x + dx$. The probability that $x \leq x(t_0) \leq x + dx$ is therefore given by the fraction of time per cycle for which x(t) lies within the x to x + dx band:

$$\begin{aligned} \text{Prob}(x \leq x(t_0) \leq x + dx) &= \frac{2(dt)}{T} \\ &= \frac{dx}{\pi\sqrt{x_0^2 - x^2}}. \end{aligned} \tag{5.8}$$

The *probability density function* $p(x)$ is defined so that:

$$\text{Prob}(x \leq x(t_0) \leq x + dx) = p(x)dx. \tag{5.9}$$

Therefore, in this case, from Equation 5.8,

$$p(x) = \frac{1}{\pi\sqrt{x_0^2 - x^2}}$$

$$\text{for} - x_0 \leq x \leq x_0. \tag{5.10}$$

Now consider the situation when $x(t)$ is no longer a sine wave, but instead represents a random process. When we say that $x(t)$ is random, we mean that the values of $x(t)$ cannot be precisely predicted in advance. As soon as they occur, these values can of course be accurately recorded. Assuming that the time record, $x(t)$, is ergodic, then we can use this time record to calculate the probability density function for $x(t)$ in exactly the same way as we have just done for a sine function. Figure 5.4 shows a sample time record for a random process with the times for which $x \leq x(t) \leq x + dx$ identified by the shaded stripes. During the observation time interval T, $x(t)$ lies in the band of values x to $x + dx$ for a total time of $(dt_1 + dt_2 + dt_3 + dt_4)$. We can therefore say that, if T is long enough, the probability density function $p(x)$ is given by the fraction of the total elapsed time for which $x(t)$ lies in the x to $x + dx$ band:

$$p(x)dx = \frac{dt_1 + dt_2 + dt_3 + dt_4}{T} = \frac{\sum dt}{T}. \tag{5.11}$$

When $x(t)$ is a random discrete data series which is obtained from the experiments, the probability density function can be measured by dividing the sample record into many different levels, measuring the time spent at each band of values of x and then using Equation 5.11. If there are N sample values, as shown in Figure 5.5, and dn of these values lie in the band of x to $x + dx$, then, corresponding to Figure 5.5, the probability density function is given by:

$$p(x)dx = \frac{dn}{N}, \tag{5.12}$$

and represents the fraction of total number of samples which lie in the x to $x + dx$ band.

It must be noted that the probability density function is the rate of change of probability versus amplitude so that the area under the curve of the probability density function gives the probability. The probability of finding an amplitude in the range between x_1 and x_2 can be given by integrating the probability density function:

$$Prob[x_1 \leq x(t) \leq x_2)] = \int_{x_1}^{x_2} p(x)dx. \tag{5.13}$$

By letting $x_1 \rightarrow -\infty$ and $x_2 \rightarrow +\infty$, we have:

$$Prob[-\infty \leq x(t) \leq \infty)] = \int_{-\infty}^{\infty} p(x)dx = 1. \tag{5.14}$$

Therefore, the total area under the probability density function must be equal to unity.

The schematic procedures used to calculate the PDF in the present study is given as follows:

- In order to standardize the results, the experimental time records were first normalized within the range of (0, 1), hence:

$$y_i = \frac{x_i - x_{min}}{x_{max} - x_{min}}, \tag{5.15}$$

$$i = 1, 2, ..., N,$$

where, x_{max} and x_{min} are the maximum and minimum values of the time records, x_i, respectively.

- Divide the full range of $y_i, i = 1, 2, ..., N$ into an appropriate number of equal width class intervals.

  Assuming that K is the number of the intervals, the width of the interval is given by:

$$\Delta y = \frac{1}{K}. \tag{5.16}$$

  The values of the data are then divided in the following classes:

$$d_j = j\Delta y, \tag{5.17}$$

$$j = 1, 2, ..., K.$$

- Sort the experimental data falling into a given interval, then:

$$N_1 = [\text{number of } y_i \text{ that } 0 \leq y_i \leq d_1,]$$

$$N_2 = [\text{number of } y_i \text{ that } d_1 \leq y_i \leq d_2,]$$

$$...$$

$$N_j = [\text{number of } y_i \text{ that } d_{j-1} \leq y_i \leq d_j,]$$

$$...$$

$$N_K = [\text{number of } y_i \text{ that } d_{K-1} \leq y_i \leq d_K.]$$

- Calculate the PDF according to the following equation:

$$\hat{p}(j) = \frac{N_j}{N\Delta y},$$

$$j = 1, 2, ..., K.$$

The PDF has been used to analyze the random signals of the void fraction in the two–phase flow which were obtained in our experiments. As a preliminary objective indicator of the flow pattern, the PDF of the void fraction signals are first examined on–line by using a Hewlett Packard analyzer. The data collected with the data acquisition system is then treated using post–processing software. Typical PDFs of the void fraction signals obtained for the different flow regimes covered in this work, are shown in Figure 5.6 to Figure 5.10.

For low inlet gas and liquid flow rates, the gas phase is unable to be distributed as fine bubbles in small I.D. tubes (Taitel *et al.*, 1980 and Barnea *et al.*, 1983). In the test section used for the present work, the bubbles have a relatively small space to move and typical small spherical bubbles were not observed very frequently. Small bubbles tend to randomly collide and agglomerate, which form a lump of bubbles or elongated bubbles. For mixtures of low inlet gas flow rates with relatively high inlet liquid flow rates, however, the forces produced by turbulence, i.e., the increase of liquid velocity, contribute to the breakup of large bubbles into smaller ones. Small bubbles are then observed for average void fraction of up to about 45%. Under these conditions, it has been observed that the bubbly flow regime that resulted is formed by both small individual bubbles and lumps of bubbles mixed in a liquid core. Under low average void fraction conditions, the PDFs of the void fraction signals for bubbly flows are characterized by a single sharp peak (see Figure 5.6). With increasing both inlet liquid and gas flow rates the PDF still shows a unique distinctive peak followed by a decreasing tail toward higher void fractions. This tail seems to be due to the presence of lumps of bubbles distributed in a liquid core. In general, for bubbly two–phase

flows the PDFs obtained from the void fraction signals show a unimodal statistical feature. This observation characterizes a quite uniform flow distribution.

When lumps of bubbles become large enough to occupy almost the whole cross section of the channel, slug flow occurs. It has been observed that for relatively low inlet liquid flow rates, bullet–shaped Taylor bubbles are formed. These Taylor bubbles moved upwards, separated by liquid slugs containing small bubbles. Between the Taylor bubbles and the wall of the channel, a thin liquid film which moves downward is also observed. The PDFs of void fraction signals for slug flows show a bimodal type distribution (see Figure 5.7). A large peak corresponding to relatively low void fractions, due to the low void content carried by the slugs of liquid is observed. A second smaller peak corresponding to higher void fractions and related to the high void content of the Taylor bubbles, is also observed. The existence of a bimodal PDF for slug flows gives an indication of the oscillating nature of this flow regime.

Starting from slug flow conditions, a further increase on the inlet gas flow rate produces more aerated liquid slugs that fail to maintain the bridge between the Taylor bubbles. Thus, the slug of liquid is destroyed and falls downward merging with the oncoming liquid slug, it is then lifted again by the flow and again destroyed. This random process produces big distorted bubbles. This chaotic behavior characterizes the churn flow. This flow pattern also produces a double modal type PDF as shown in Figure 5.8. The first local mode (left side peak in the Figure) corresponds to the presence of an unstable and short portion of liquid that tends to decrease the void fraction. The elongated gas–dominant portions that pass more frequently through

the measurement device, promote the increase of the second local mode (right side peak in Figure 5.8).

Further increase of the inlet gas flow rate forces the gas phase to flow along the center line of the test section, entraining liquid droplets or liquid streaks (wisps) inside the gas core and a thin liquid film moving upward between the gas and the wall. Under these conditions the annular or wispy annular flow patterns take place. The visually observed periodicity of slug and churn flows disappears in annular flows. The PDFs for annular flow patterns show a unimodal peak at relatively high void fraction (see Figure 5.9). Adiabatic annular flow are characterized by a relatively uniform axial flow distribution.

Figure 5.10 shows the manner in which the PDF varies with the gas superficial velocity, i.e, flow patterns.

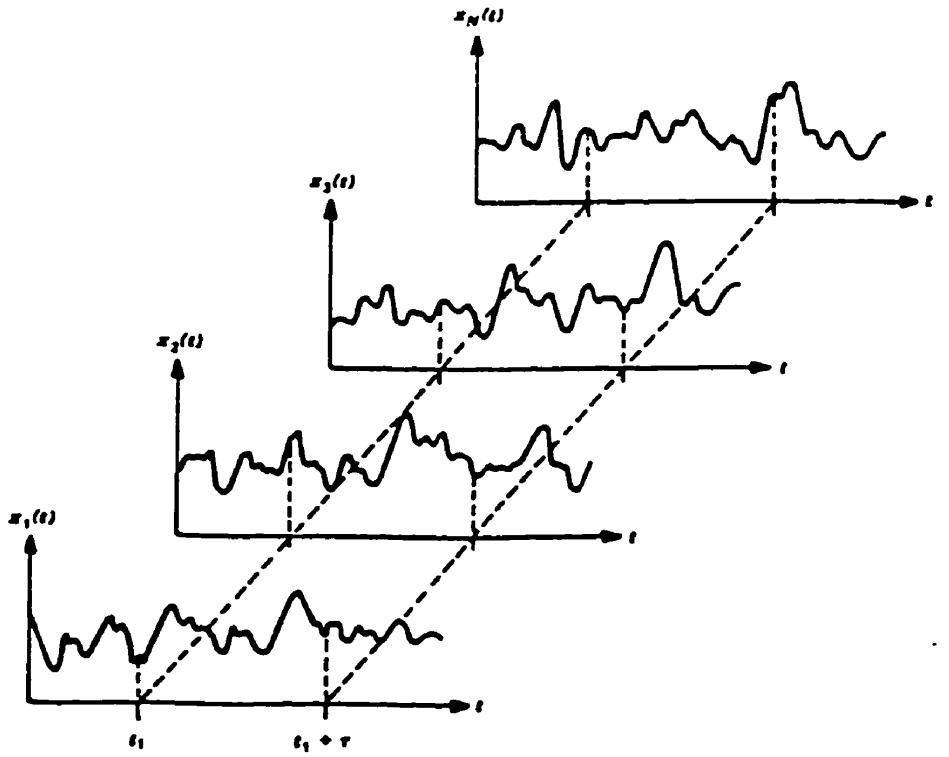

Figure 5.1: A random process for ensemble time records.

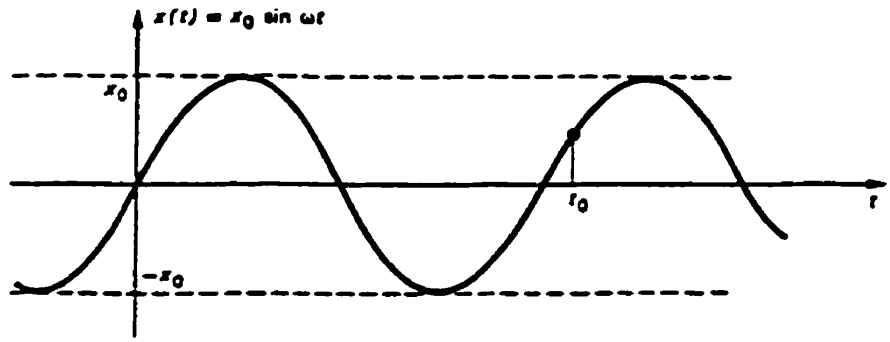

Figure 5.2: Waveform for steady state deterministic function $x(t) = x_0 sin(\omega t)$

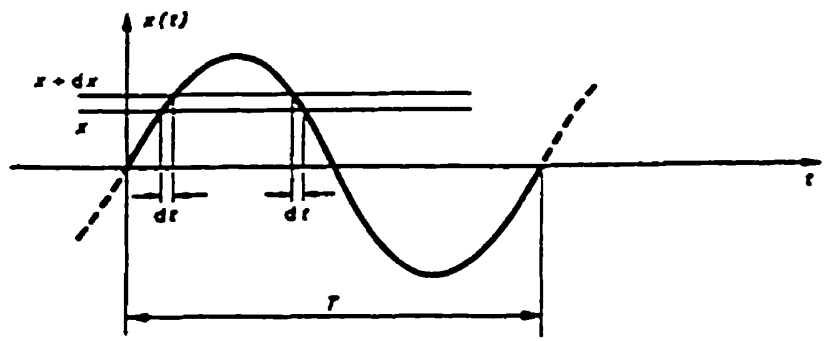

Figure 5.3: Illustrating calculation of time for which $x \leq x(t) \leq x + dx$.

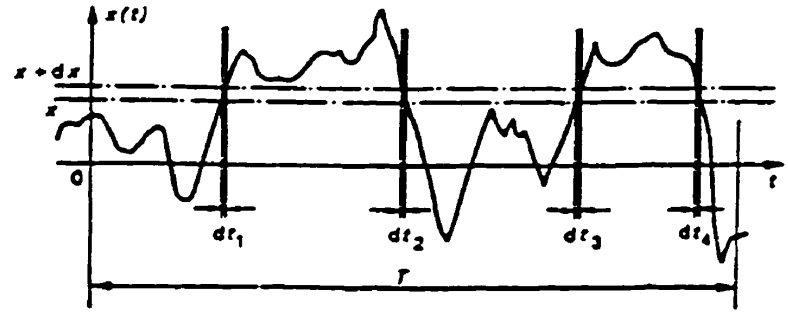

Figure 5.4: Calculation of the probability density function $p(x)$ for a random process.

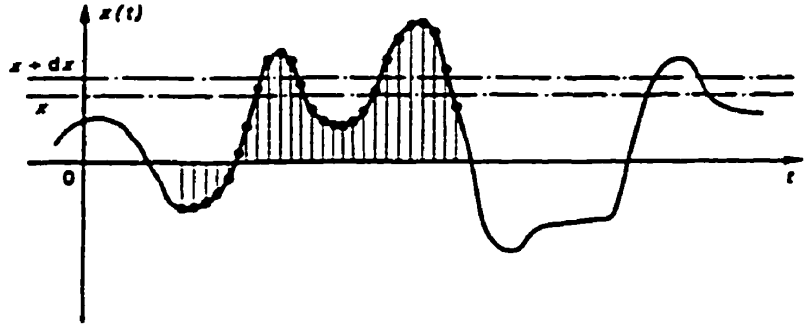

Figure 5.5: Sampling a random time history for digital analysis.

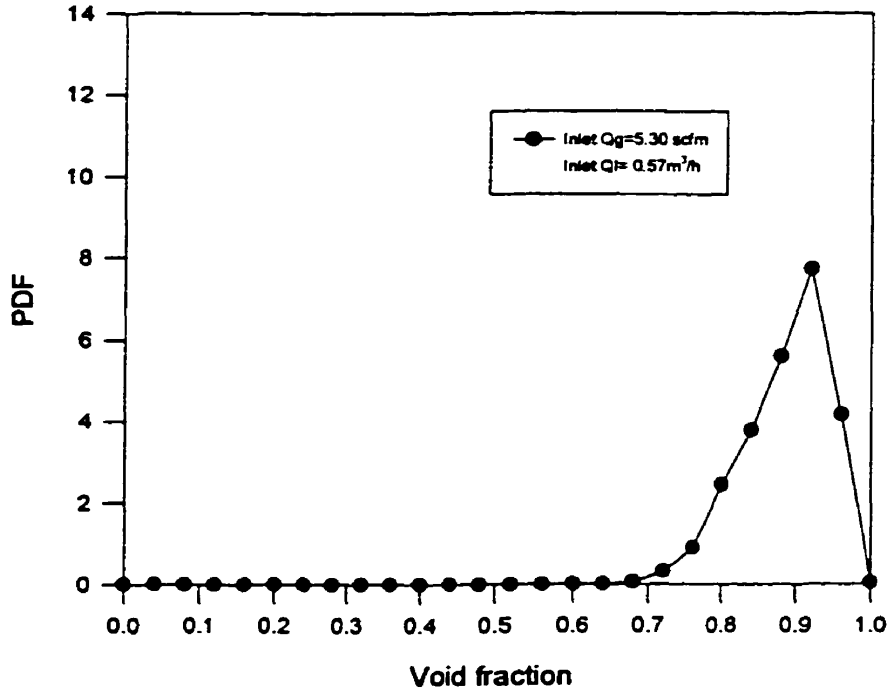

Figure 5.6: PDF for bubbly flow on void fraction signals.

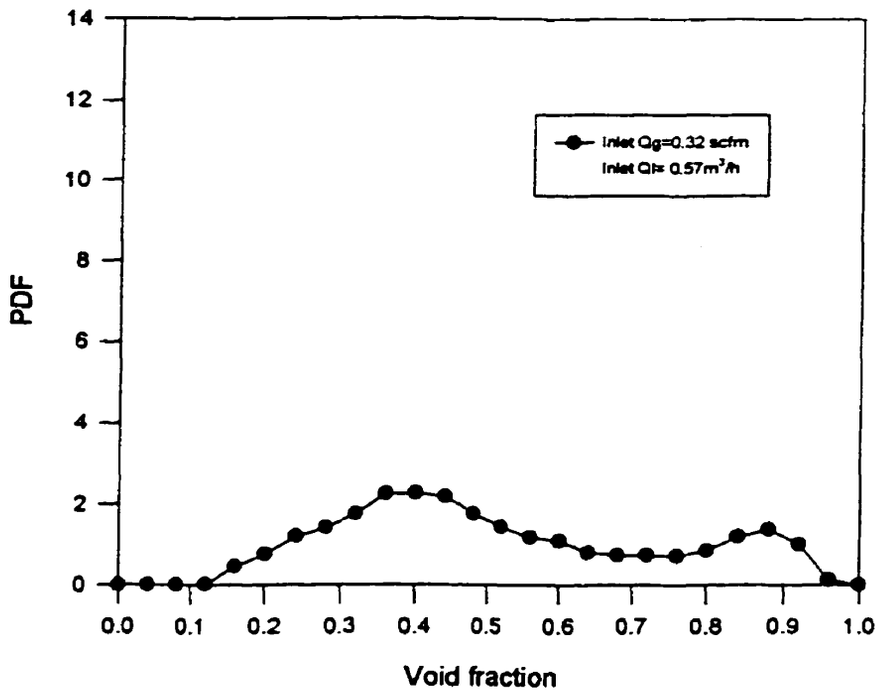

Figure 5.7: PDF for slug flow on void fraction signals.

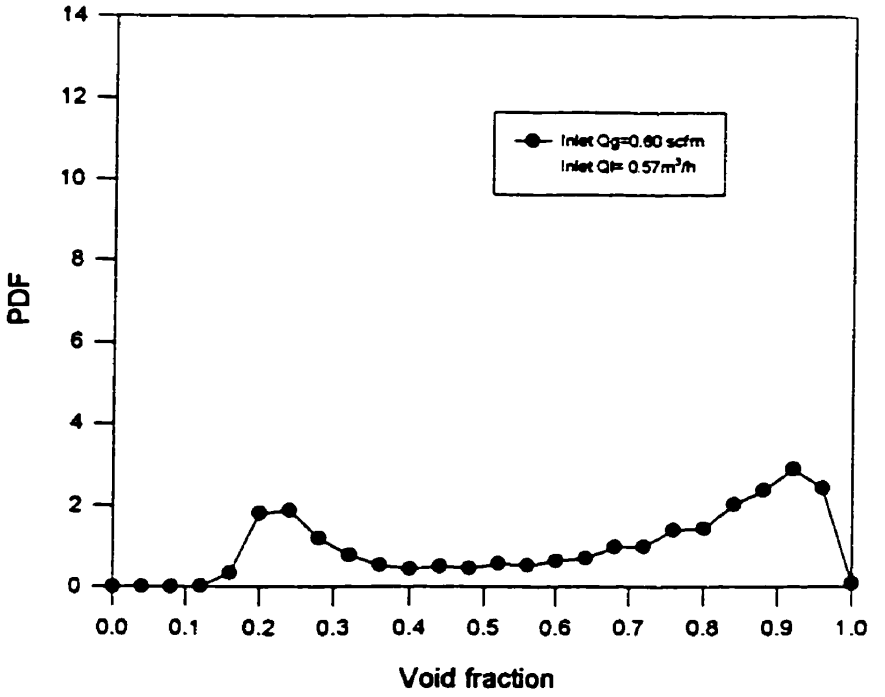

Figure 5.8: PDF for churn flow on void fraction signals.

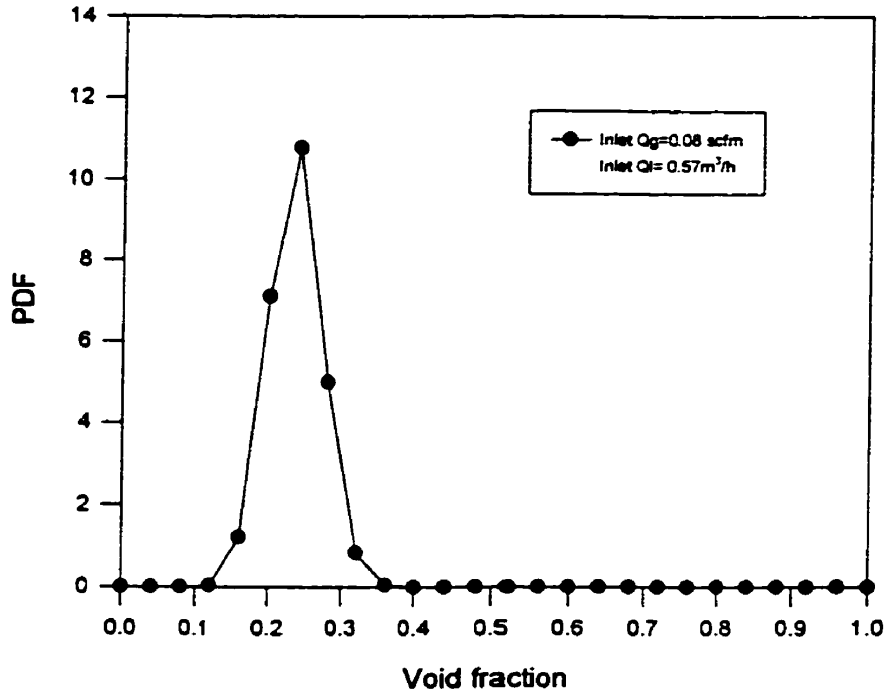

Figure 5.9: PDF for annular flow on void fraction signals.

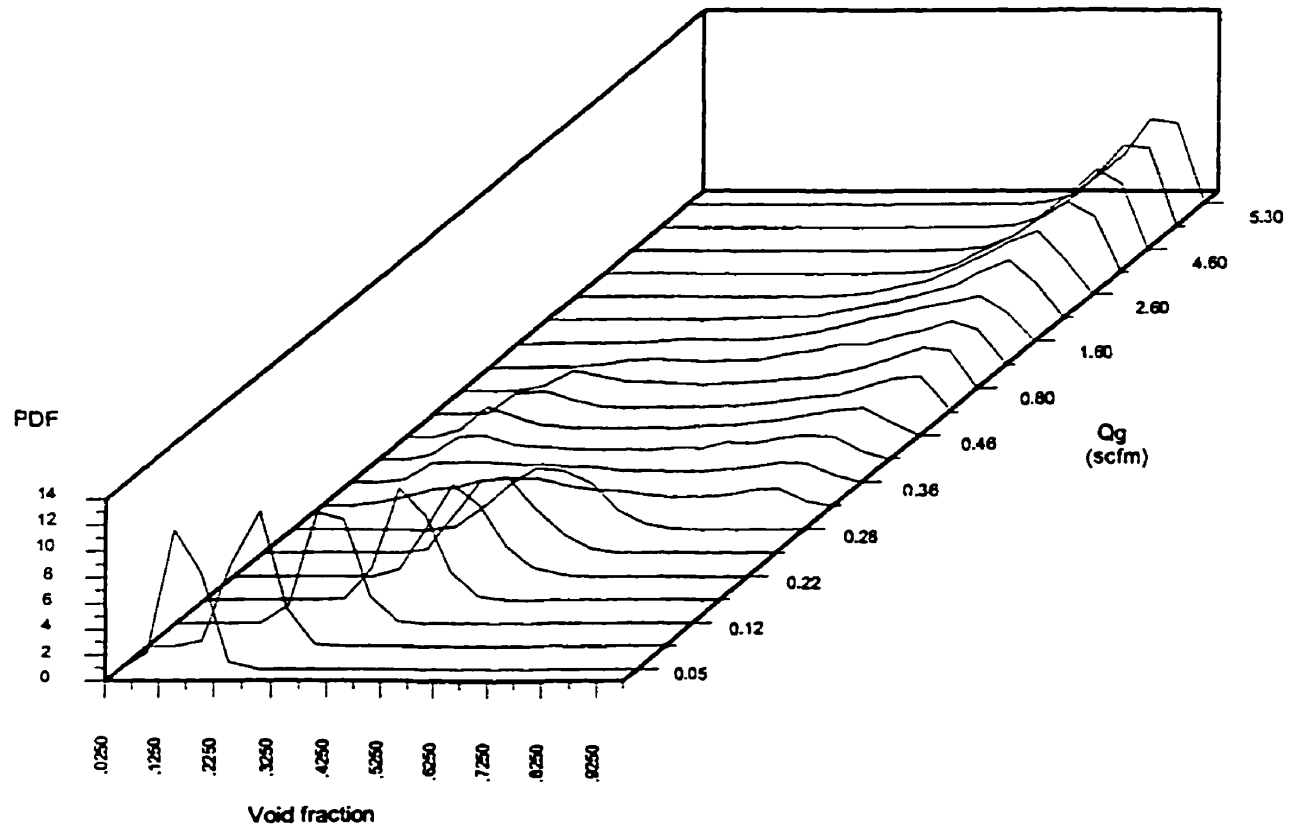

Figure 5.10: Three–dimensional figure of PDF on void fraction signals.

5.3 Important Statistical Moments

The central moments of a distribution, which are regarded as other statistical properties, have been used to characterize the flow patterns in the present study.

- The first moment is the mean value of the original signals.
- The second moment is the variance of the original data. It is a measure of scattering of the distribution around the mean value. The value is the square of the standard deviation, σ, given by:

$$\sigma^2 = \frac{1}{N}\sum_{1}^{N}(x_i - E)^2. \tag{5.18}$$

- The third normalized moment, i.e. the coefficient of skewness, is the third central moment normalized by the third power of the standard deviation. If the n-th central moment is calculated by:

$$\mu_n = \frac{1}{N}\sum_{1}^{N}(xi - E)^n.$$

The skewness coefficient is obtained for $n = 3$, given by:

$$\gamma = \frac{\mu_3}{\sigma^3}. \tag{5.19}$$

The skewness is a measure of the asymmetry of a distribution. A symmetric distribution, such as a normal distribution, has zero skewness. A unimodal distribution, which has a median to the left of the mean, (i.e., it is skewed to the left) has a negative skewness. If the distribution is skewed to the right, the skewness will hold a positive value. The skewness is related to the spread of the distribution of signals.

- The forth normalized moment, i.e. coefficient of kurtosis, is the fourth central moment normalized by the forth power of standard deviation. It is a measure of the peakedness of the distribution. The excess coefficient is the value of the kurtosis coefficient minus three, calculated by:

$$\gamma_2 = \frac{\mu_4}{\sigma^4} - 3. \tag{5.20}$$

The normal distribution has an excess coefficient equal to zero. In such a case, the distribution is identified as mesokurtic. A distribution with excess less than zero is called platykurtic. Such a distribution is flatter than a normal one. Distributions with more peakedness than a normal distribution are called leptokurtic, and have a coefficient of excess greater than zero.

The four moments have been used to analyse the signals of void fraction and the pressure to characterize the flow patterns.

When the void fraction is lower than about 45%, the two–phase flow is generally a bubbly flow. The variance of both the void fraction and the pressure has the smallest value (see Figure 5.11 and Figure 5.12). This means that the amplitude of the fluctuation of the void fraction and the pressure is the smallest. The skewness coefficient (see Figure 5.13 and Figure 5.14) and the excess coefficient (see Figure 5.15 and Figure 5.16) are close to zero, which characterizes a unimodal type PDF distribution for bubbly flow.

When the void fraction is larger than 45% but less than about 60%, the slug flow pattern prevails in the test section. A sharp increase of the variance of both the void

fraction and the pressure can be seen near the boundary of the bubbly and the slug flow (see Figure 5.11 and Figure 5.12). The sharp increase of the variance indicates the beginning of a violent flow, i.e., the slug flow. For slug flow, most of the values of the skewness and excess coefficients of both the void fraction and the pressure are negative (see Figure 5.13 to Figure 5.16). This characterizes a left-skewed bimodal PDF distribution for slug flow.

When the void fraction increases further, churn flow can be observed. This flow pattern is quite violent and the variance of the void fraction reaches its highest value for both the void fraction and the pressure (see Figure 5.11 and Figure 5.12). Most of the values of the excess are negative for both the void fraction and the pressure (see Figure 5.15 and Figure 5.16). Churn flow is characterized by a right-skewed bimodal PDF distribution. However, the skewness for the void fraction (Figure 5.13) does not provide correct value for this type of flow pattern.

When the void fraction exceeds 80%, annular flow occurs. For the void fraction, the variance of the annular flow decreases gradually to zero.The variance of the pressure for the annular flow is greater than that for the bubbly flow but smaller than that for the churn flow. The values of the excess of the void fraction are close to zero (Figure 5.15). This is consistent with a unimodal PDF distribution for annular flow. However, the values of the excess of the pressure (Figure 5.16) do not reflect the PDF distribution of this kind of flow pattern.

The results of the analysis for typical flow patterns are summarized in Table 5.1. It has been shown that the four moments can be used as an auxiliary tool to allow

different flow patterns to be distinguished.

Table 5.1: Four moments of the void fraction for different flow patterns.

four moments	bubble flow	slug flow	churn flow	annular flow
average	small	large	larger	largest
variance	small	large	largest	moderate
skewness	near zero	negative	positive	moderate
excess	positive	negative	negative	positive

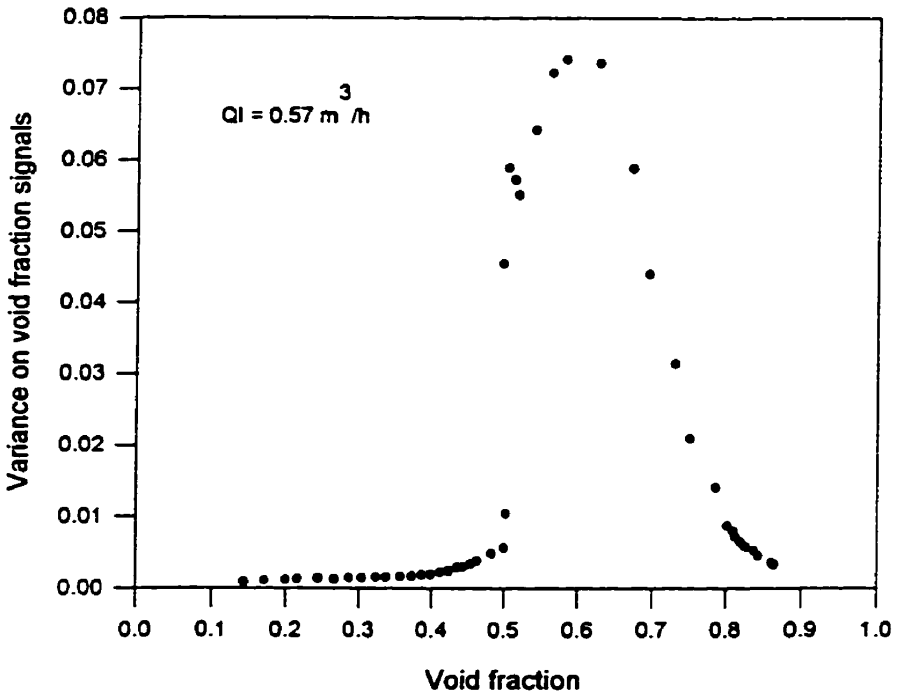

Figure 5.11: The variance of the void fraction.

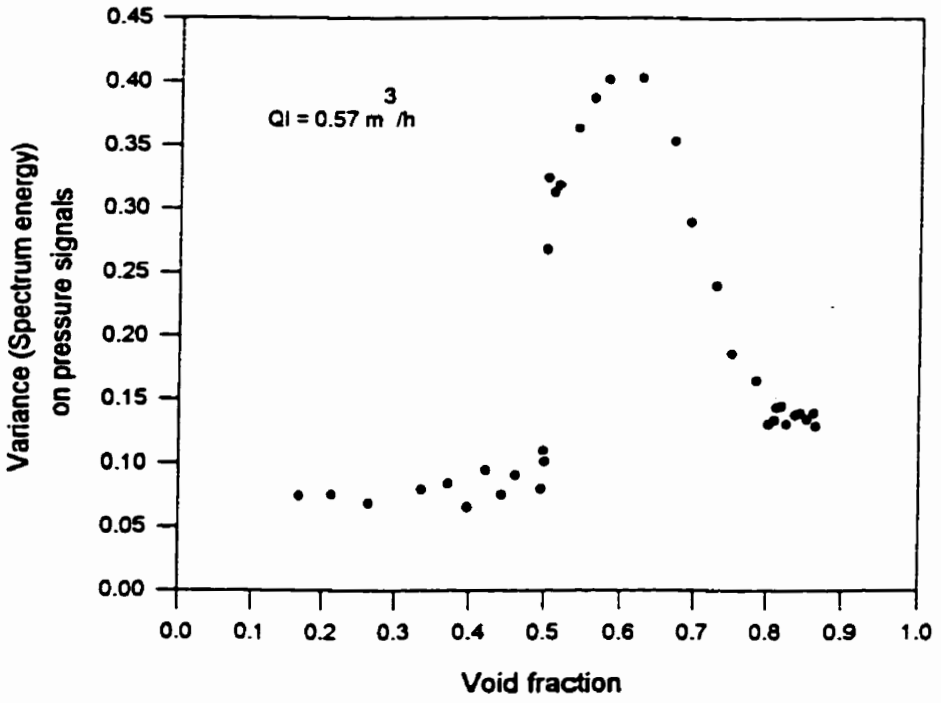

Figure 5.12: The variance of the pressure.

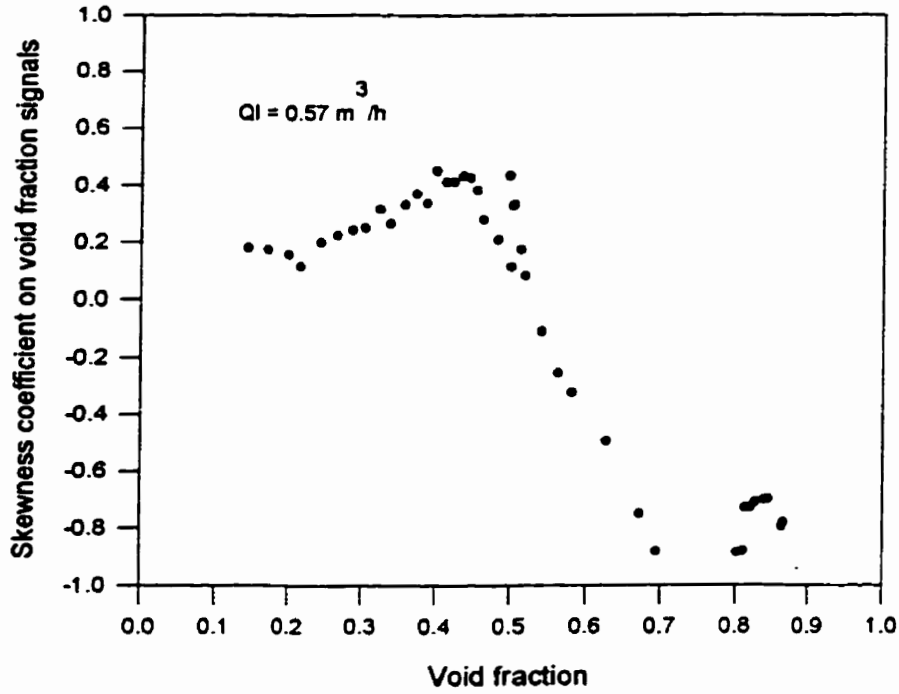

Figure 5.13: The skewness coefficient of the void fraction.

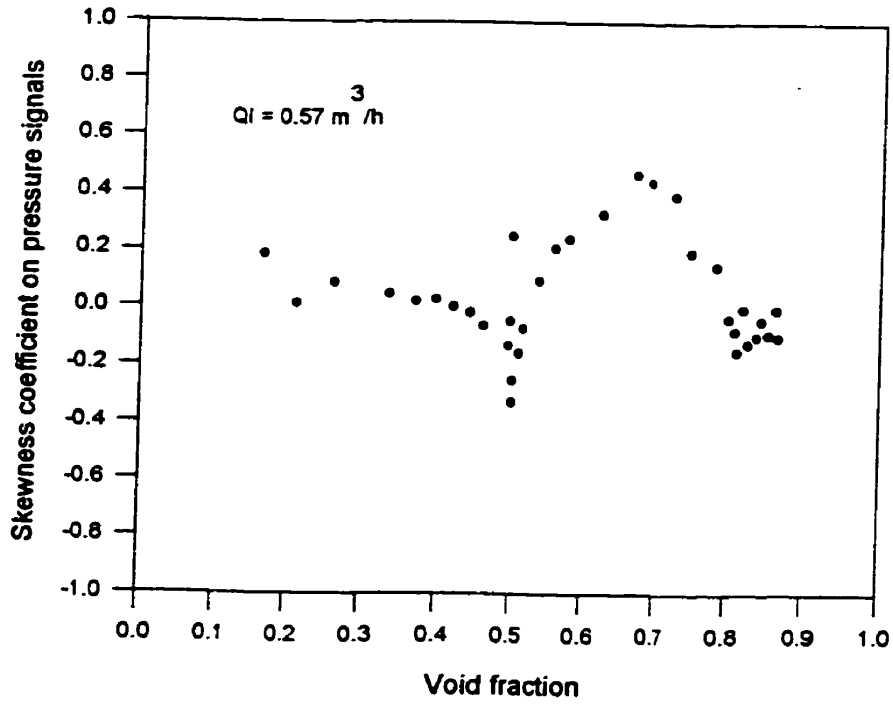

Figure 5.14: The skewness coefficient of the pressure.

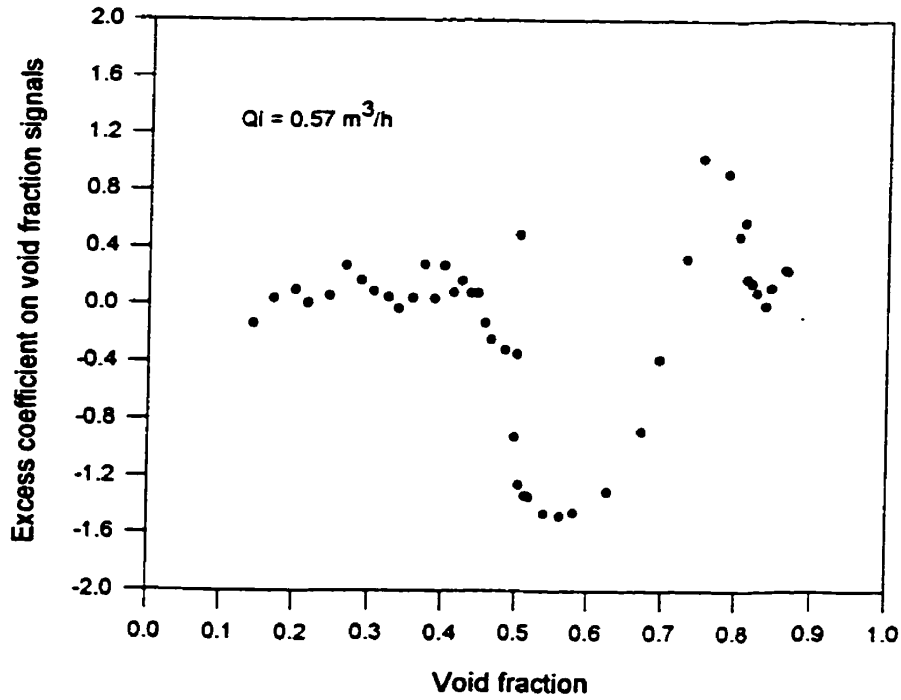

Figure 5.15: The excess coefficient of the void fraction.

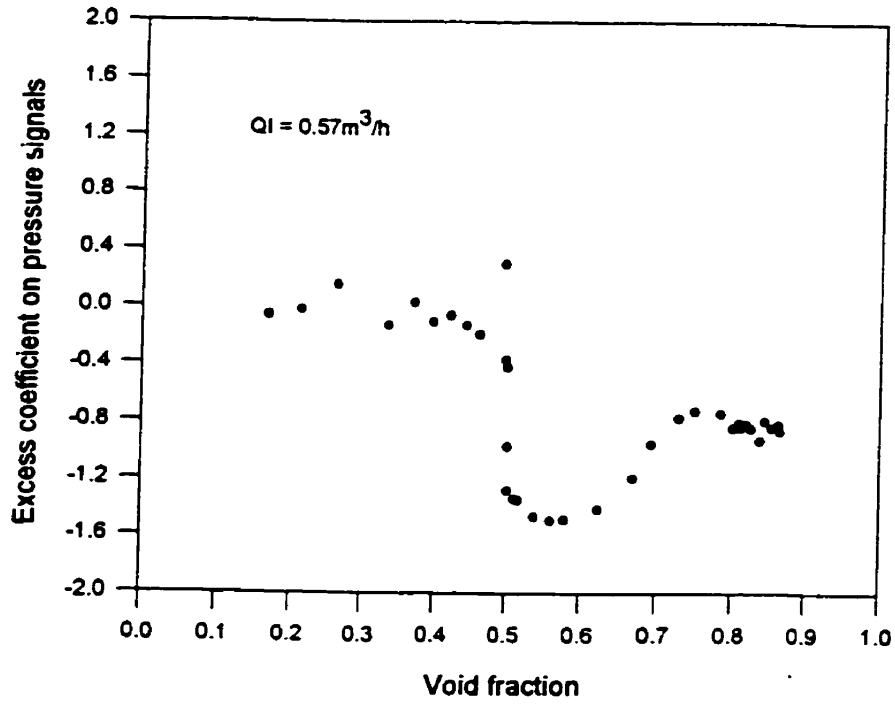

Figure 5.16: The excess coefficient of the pressure.

5.4 Power Spectrum Distribution Function

Many engineering applications that require the analysis of random data requires as well the determination of the linear relationships of the data. In general, these linear relationships can be represented by a correlation function, or its Fourier transform which is called a Power Spectrum Density Function. Correlation and power spectrum density functions provide the same information extracted from the data, but presented in a different domain. The correlation function provides the analysis in the time domain while the power spectrum density function in the frequency domain. Compared with the correlation function, power spectrum density function is developed more directly as an useful analytical tool for engineering problems.

For a set of data $x(t)$, the auto-correlation function for any time delay, τ, is given by:

$$R_x(\tau) = \lim_{T \to \infty} \frac{1}{T} \int_0^T x(t)x(t+\tau)dt. \tag{5.21}$$

For the time lag, $\tau = 0$, the value of the auto–correlation goes to a maximum that corresponds to the mean square value of the data:

$$R_x(0) = \sigma^2 + E^2. \tag{5.22}$$

If the mean value of the data is equal to zero, the autocorrelation at zero time lag is the variance of the data.

The auto-correlation is usually interpreted as the manner in which future values of the data are related to the current values, or how well the future data can be predicted by the past measurements.

By definition, the power spectrum density function for one set of data is the Fourier transform of the auto-correlation function.

$$S_x(f) = \int_{-\infty}^{\infty} R_x(\tau) e^{-j2\pi f\tau} d\tau. \tag{5.23}$$

Since the auto-correlation is always an even function of τ with respect to the integral range of $\int_{-\infty}^{\infty}$, it follows that:

$$S_x(-f) = S_x(f). \tag{5.24}$$

The spectral density function in the equation is defined over all the frequencies. For engineering applications, only the spectral density function on positive frequencies is useful. The power spectrum density function over positive frequencies, denoted by $G_x(f)$, as shown in Figure 5.17, is then introduced as:

$$G_x(f) = 2S_x(f) = 2\int_{-\infty}^{\infty} R_x(\tau) e^{-j2\pi f\tau} d\tau, \tag{5.25}$$

$$f \geq 0.$$

The auto-correlation function is obtained by the inverse Fourier transformation:

$$R_x(\tau) = \int_{-\infty}^{\infty} S_x(f) e^{j2\pi f\tau} df = \int_0^{\infty} G_x(f) \cos 2\pi f\tau df. \tag{5.26}$$

When τ is equal to zero, it follows that:

$$R_x(0) = \int_0^{\infty} G_x(f) df = \sigma^2 + E^2. \tag{5.27}$$

When only the fluctuating components of the data are treated the mean value of the data, E, is equal to zero. The total area under the spectral density function $G(f)$ or $S(f)$ is exactly the variance of the data, which is also called total "Spectrum Energy". The spectral density function is usually interpreted as the manner in which the total

spectrum fluctuating energy is distributed with frequency. For typical periodical phenomenon, for example, sinusoidal signals, all the spectrum energy is centered at a unique frequency. For widely stochastic phenomena, for example, white noise signals, the spectral density is a constant over all the frequencies.

It must be pointed out that Equation 5.23 or Equation 5.25 gives the fundamental definition of PSDF. In engineering applications, data records are never available for the integral range of $(-\infty, +\infty)$. In general, data records are only available for a limited time period $t = 0$ to $t = T$. In this case we cannot calculate the corresponding PSDF according to its fundamental equation since we do not know $R_x(\tau)$ for $| \tau | < T$. The best we can do is to approximate $G_x(f)$ by truncating the integral in Equation 5.25 to give the approximation:

$$G_x(f) = 2S_x(f) \simeq 2\int_{-T}^{T} R_x(\tau)e^{-j2\pi f\tau}d\tau. \tag{5.28}$$

Therefore, the statistical error occurs inevitably due to the approximation.

Now let us study a little more the difference of Equation 5.25 and Equation 5.28 in order to see if we can reduce the statistical error introduced by the approximation. Actually, the approximated PSDF given in Equation 5.28 can be regarded as the result of the Fourier transform of the function $R_x(\tau)$ multiplied by a rectangular function $u(\tau)$:

$$Y_x(\tau) = R_x(\tau), \tag{5.29}$$

$$u(t) = \begin{cases} 1 & \text{if } -T \le t \le T \\ 0 & \text{otherwise} \end{cases}$$

$$G_x(f) = 2S_x(f) = 2\int_{-\infty}^{\infty} R_x(\tau)e^{-j2\pi f\tau}u(\tau)d\tau$$

$$= 2\int_{-\infty}^{-T} R_x(\tau)e^{-j2\pi f\tau}u(\tau)d\tau + 2\int_{-T}^{T} R_x(\tau)e^{-j2\pi f\tau}u(\tau)d\tau + 2\int_{T}^{\infty} R_x(\tau)e^{-j2\pi f\tau}u(\tau)d\tau$$

$$= 2\int_{-T}^{T} R_x(\tau)e^{-j2\pi f\tau}u(\tau)d\tau.$$

The function $u(\tau)$ is called a time window function, as shown in Fig 5.18. It should be noted that $u(\tau)$ is not necessarily a rectangular function. In order to get a better approximation of the PSDF or to further reduce the statistical error, some other window functions can also be used.

In general, the finite Fourier transform of $x(t)$ can be regarded as the Fourier transform of an infinite time record $v(t)$ multiplied by a time window function $u(t)$:

$$x(t) = u(t)v(t).$$

The Fourier transform of $x(t)$ is the convolution of the Fourier transforms of $u(t)$ and $v(t)$:

$$X(f) = \int_{-\infty}^{\infty} U(\theta)V(f-\theta)d\theta, \tag{5.30}$$

where, θ is a dummy frequency, $U(\theta)$ is the Fourier transform of the time window $u(t)$ and called the corresponding spectral window function. $V(\theta)$ is the Fourier transform of $v(t)$. It should be pointed out that it is only necessary to apply a windowing technique for a limited time record. For an infinite time record we do not have such a problem.

In our study, the PSDF is approximated by a Fast Fourier Transform (FFT), based on direct finite Fourier transform of the original experimental data, because the FFT method requires less computer calculations. The PSDF approximated by the FFT is equivalent to that obtained by applying the Fourier transform of the auto-correlation function (Bendat & Piersol, 1992).

Consider a continuous time record, $x(t)$, with the mean value equal to zero. Let the time record be divided into n_d subrecords, each of the subrecord containing a data length T. The purpose of dividing the data into subrecords is to reduce the random error and give a "smooth" approximation by averaging the results in each subrecord. Then:

$$x_i(t) \in x(t)$$

$$i = 1, 2, ..., n_d$$

$$(i-1)T \leq t \leq iT$$

The finite-range Fourier transform over $(0, T)$ for a subrecord of data is then defined as:

$$X_i(f, T) = \int_0^T x_i(t) e^{-j2\pi ft} dt. \tag{5.31}$$

The approximation of the power spectrum density function over positive frequencies is given by:

$$\hat{G}_x(f) = \frac{2}{n_d T} \sum_{i=1}^{n_d} | X_i(f, T) |^2 . \tag{5.32}$$

Now that let us consider an experimental discrete time record. Suppose that a discrete time record is divided into n_d subrecords and each subrecord $x_i(t)$ contains N data values, x_{in} , with $n = 0, 1, ..., N-1, i = 1, 2, ..., n_d$. The Fourier transform will be

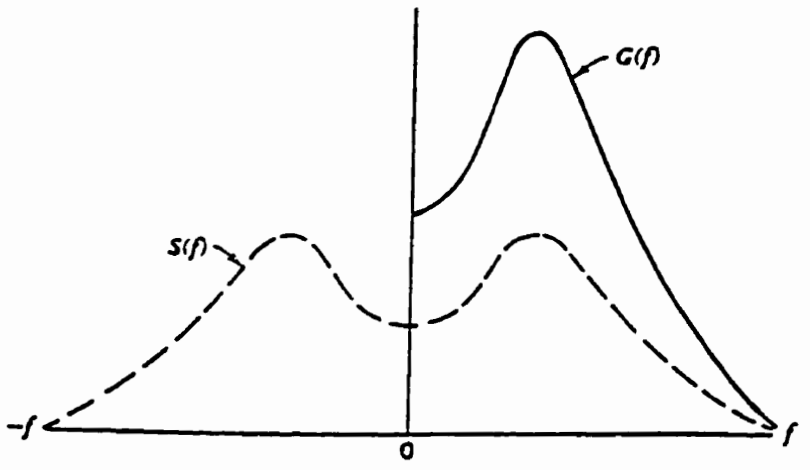

Figure 5.17: Relationship of spectral density functions $G(f)$ and $S(f)$

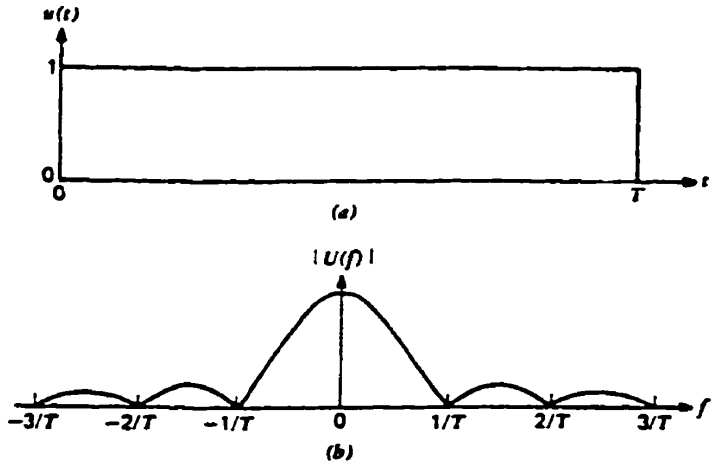

Rectangular analysis window. (*a*) Time window. (*b*) Spectral window.

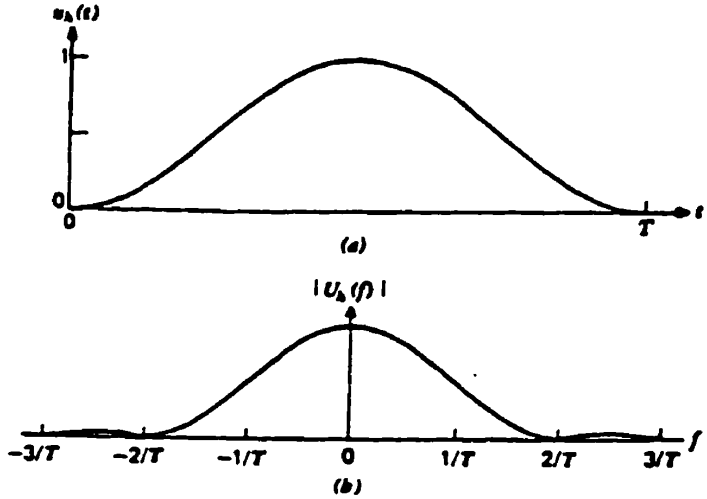

Hanning analysis window. (*a*) Time window. (*b*) Spectral window.

Figure 5.18: Windowing in spectrum approximation.

performed at discrete frequencies that are given by:

$$f_k = \frac{k}{N\Delta t}, \tag{5.33}$$

$$k = 0, 1, ..., N-1.$$

The finite-range Fourier transform over $(0, N)$ is given by:

$$X_i(f_k) = \Delta t \sum_{n=0}^{N-1} x_{in} e^{\frac{-j2\pi kn}{N}}, \tag{5.34}$$

$$k = 0, 1, ..., \frac{N}{2}.$$

When a window function $U(n)$ is used, the approximation of the spectral density function is given by:

$$X_i(f_k) = \Delta t \sum_{n=0}^{N-1} x_{in} U(n) e^{\frac{-j2\pi kn}{N}} \tag{5.35}$$

where $U(n)$ is the window function in discrete form.

The power spectrum density function for the discrete data is then given by:

$$\hat{G}_x(f_k) = \frac{2}{n_d N\Delta t} \sum_{i=1}^{n_d} | X_i(f_k) |^2 . \tag{5.36}$$

The spectral density function for discrete data is calculated using FFT algorithm, described in detail in Bendat & Piersol (1986). The transform is carried out only over the frequencies $(0, \frac{N}{2})$. This is due to the fact that the Nyquist frequency f_c occurs at $k = \frac{N}{2}$. The spectral values at $k = 0, 1, ..., \frac{N}{2}$ define the spectral estimate within the Nyquist frequency range, whereas the rest of the spectral values at $k = \frac{N}{2} + 1, \frac{N}{2} + 2, ..., N-1$ can be regarded as the spectral estimate in the range of $-f_c \leq f \leq 0$. To perform the FFT procedures, it is better to choose the length of the subrecord time record, N, equal to a power of 2, $N = 2^p$.

In the current study, the PSDF has been calculated on the signals of the differential pressure to characterize the flow regimes in the frequency domain. From experimental studies it has been shown (Akagawa *et al.* 1971; Tutu 1982; Matsui 1984) that differential pressure signals are more appropriate to carry out flow pattern identification. The use of differential pressures allow external mechanical vibrations to be canceled. In order to capture the inherent frequency components of the flow, the distance between the pressure taps has to be properly selected. For the present work the distance between the pressure taps is fixed at 19 mm. A numerical high pass filter with a cut–off frequency of 0.25 Hz is used to reduce the influence of the very low frequencies caused by the pump into the measured pressure signals. Typical normalized PSDF results obtained from pressure signals are shown in Figures 5.19, Figures 5.21, Figures 5.23 and Figures 5.25.

The PSDF has also been applied to the signals of the void fraction measured using Electrode #8 because it is located close to the pressure transducer c4. Hence, the PSDF results of the pressure and the void fraction can be compared. Typical normalized PSDF results obtained from pressure signals are shown in Figures 5.20, Figures 5.22, Figures 5.24 and Figures 5.26.

Bubbly flows are characterized by broadband PSDF's covering a wide range of frequencies (see Figure 5.19 for the pressure signals and Figure 5.20 for the void signals). The fluctuating amplitude of the frequency components for bubbly flows have small values. Further, the amplitude of the spectrum decreases with frequency. For bubbly flows, small gas bubbles in the liquid core contribute to a random process with

relatively low total spectrum energy (see Fig 5.12 and Fig 5.11).

For slug flows, the PSDF's show a dominant frequency component accompanied by several smaller amplitude components as shown in Figures 5.21 and Figures 5.22. The dominant frequency is attributed to Taylor bubbles passing periodically through the pressure taps and void gauges. The presence of the small peaks is attributed to small bubbles moving more or less randomly within the liquid slugs. The presence of a dominant frequency indicates the periodical nature of slug flows. It has also been observed that the dominant frequency increases with increasing inlet liquid flow rate. This behavior is due to the fact that Taylor bubbles tend to move faster with increasing liquid velocity. Furthermore, the spectrum energy for slug flows is larger than that for bubbly flows (see Fig 5.12 and Fig 5.11).

Similar to slug flows, churn flows are characterized by the presence of a dominant frequency component (see Figures 5.23 and Figures 5.24). However, for a constant inlet liquid flow rate, it has been noticed that the dominant frequency for churn flows is higher than that observed for slug flows. Once more the dominant frequency increases with increasing liquid velocity. It must be pointed out that the total spectrum energy for churn flows reaches the highest value compared to all the other flow regimes studied. Even though, the distribution of the phases seems to be chaotic, the presence of a dominant frequency confirms the periodic behavior for this type of flow.

During the churn to annular flow transition it has been observed that the spectra around the dominant frequency broadens, i.e. a wider band peak is observed for flows near the transition conditions. A further increase in the inlet gas flow rate

allows the annular flow distribution to be developed and a sharp dominant high frequency component is observed (see Figures 5.25 and Figures 5.26). As was already pointed out for both boiling (Jain & Roy, 1983) and adiabatic flows (Nishikawa *et al*, 1969), this high frequency is caused by surface waves that develop at the gas–liquid interface. The total spectrum energy for annular flows is of a medium value and the dominant frequency shifts to higher values with increasing flow velocity.

It is important to note the strong similarity that exists between PSDF's obtained from the pressure and void fraction signals (compare the PSDF figures for a same type of flow pattern). Thus, the measurement of differential pressures, using appropriate pressure taps and transducers can provide excellent information on the inherent characteristics of the structure of two–phase flows.

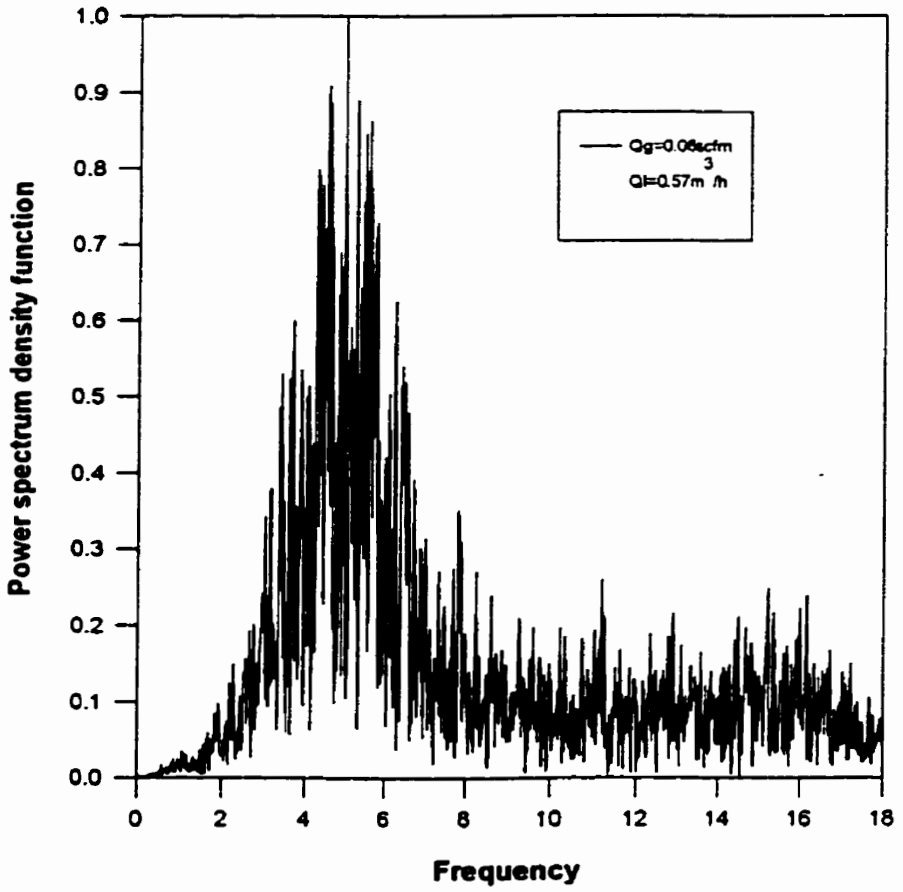

Figure 5.19: PSDF for bubbly flow on pressure signals.

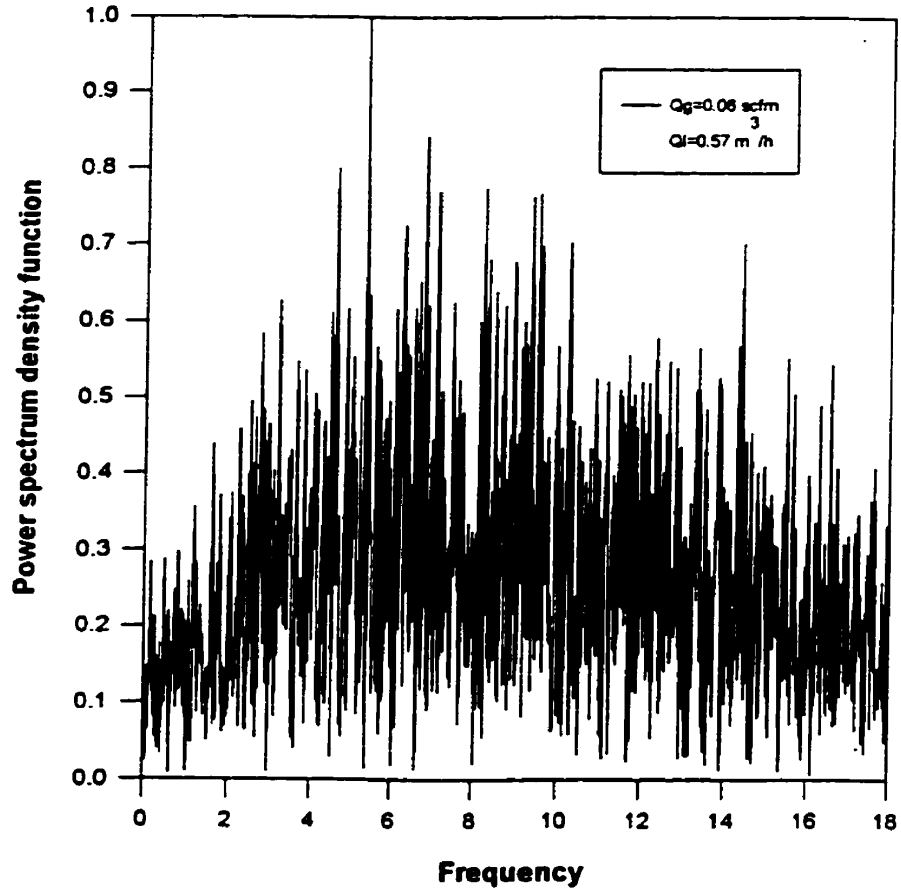

Figure 5.20: PSDF for bubbly flow on void fraction signals.

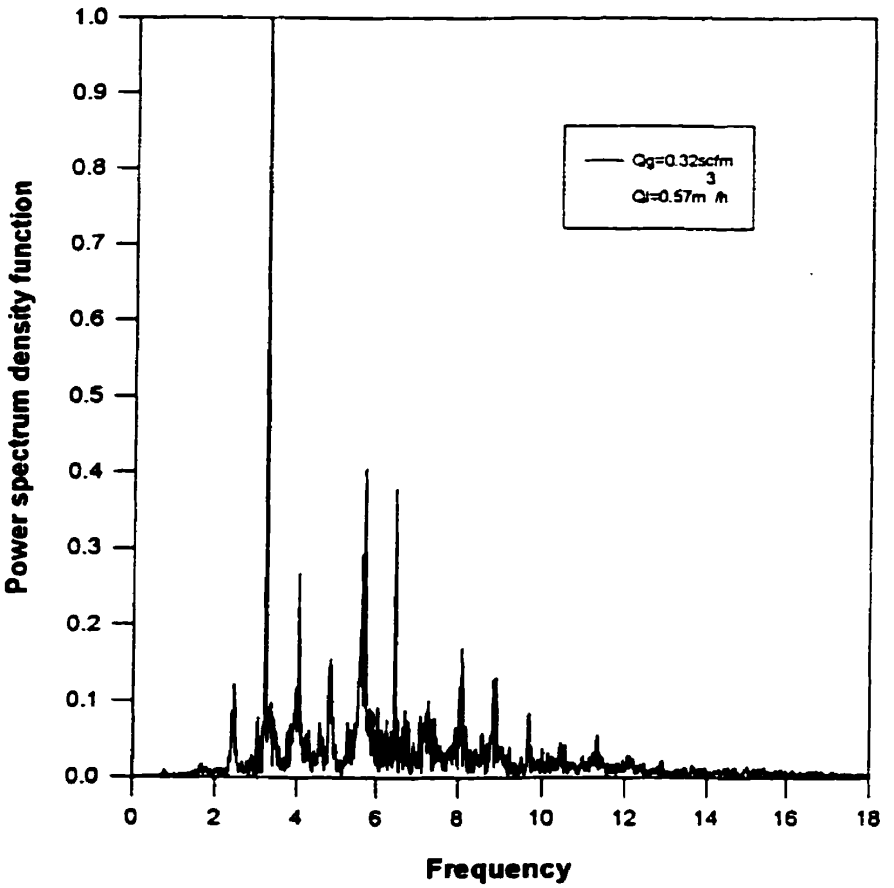

Figure 5.21: PSDF for slug flow on pressure signals.

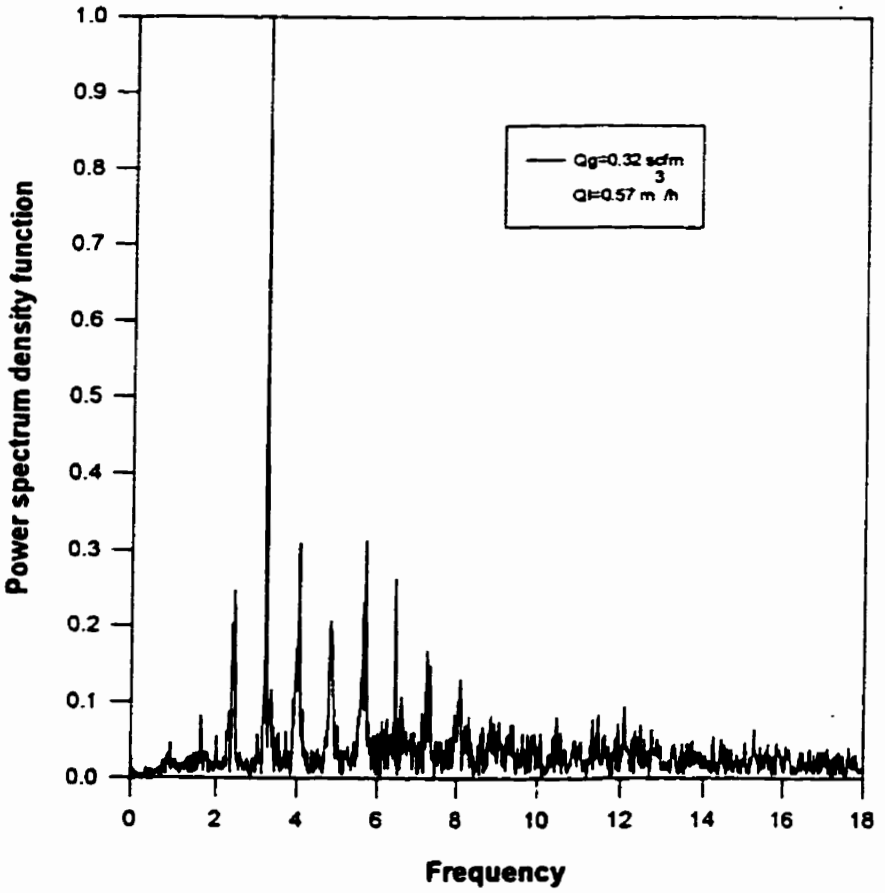

Figure 5.22: PSDF for slug flow on void fraction signals.

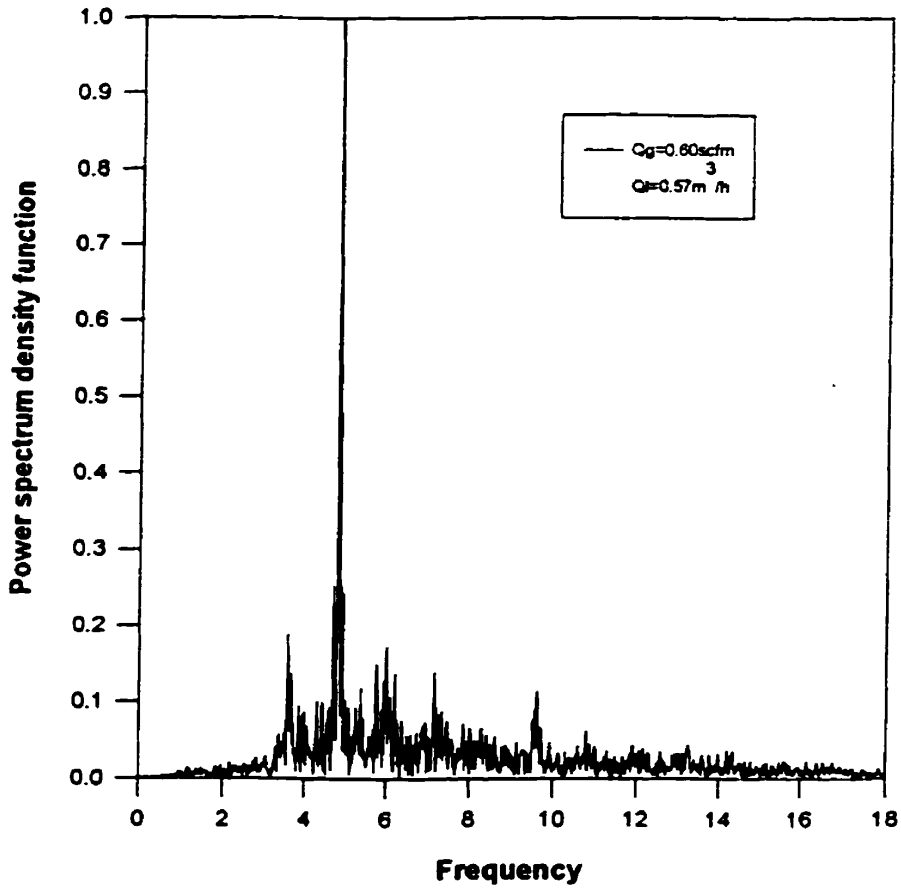

Figure 5.23: PSDF for churn flow on pressure signals.

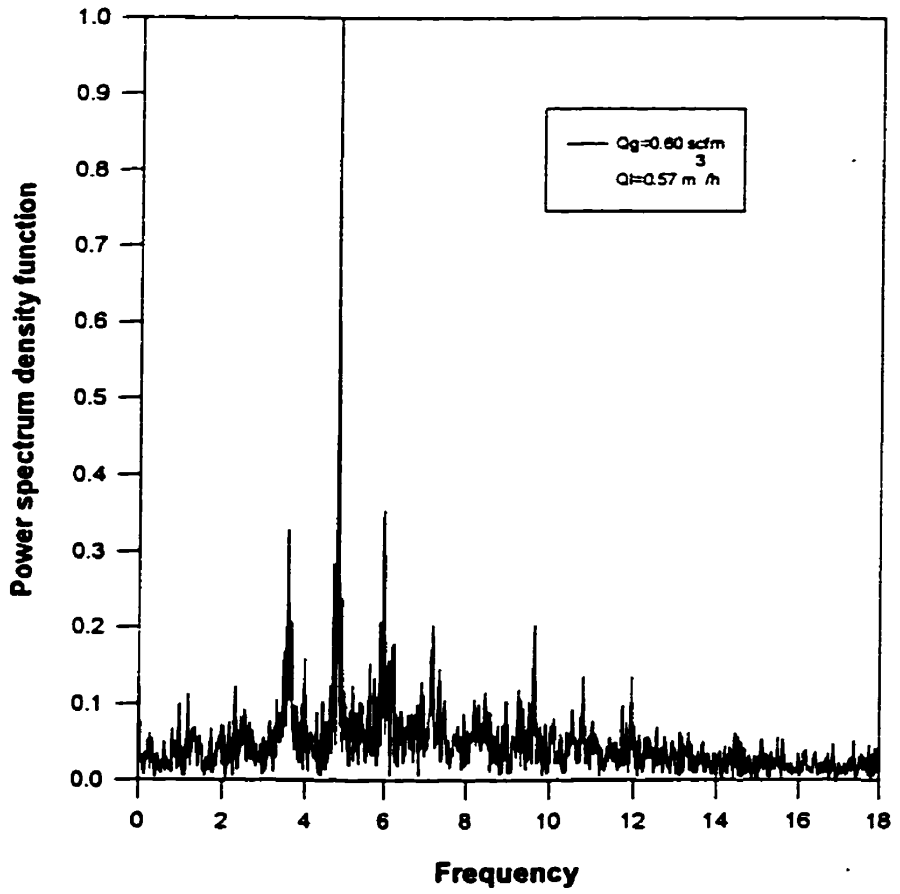

Figure 5.24: PSDF for churn flow on void fraction signals.

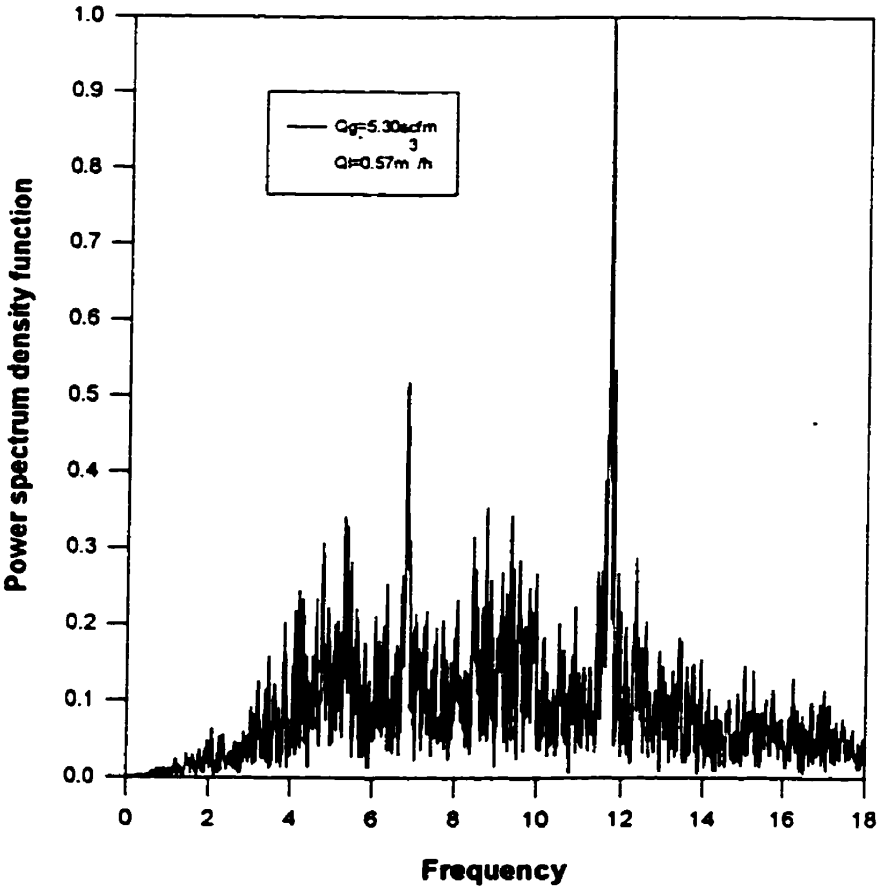

Figure 5.25: PSDF for annular flow on pressure signals.

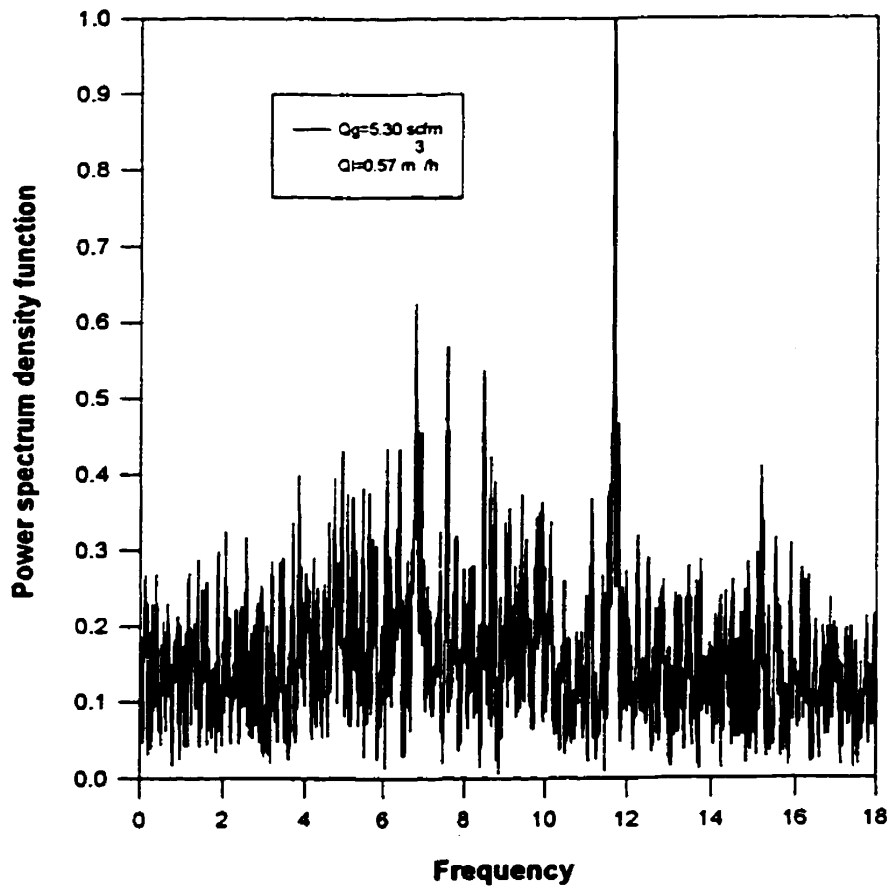

Figure 5.26: PSDF for annular flow on void fraction signals.

Chapter 6

Construction of Flow Pattern Map

The PDF and the PSDF have been applied to the fluctuating signals of the void fraction and the pressure. It has been shown that the shapes of the PDF and the PSDF are strongly dependent on the flow patterns. Qualitatively, bubbly flows are characterized by a broadband spectrum distribution and single modal PDF at a low void fraction. Annular flows are characterized by dominant–peak spectrum and single modal PDF at a high void fraction. Slug and churn flows are characterized by a dominant peak spectrum and double modal PDF, differentiated by the location of the bigger peak of the PDF. In this chapter, two quantitative criteria, which are based on the qualitative study of the PDF and the PSDF, respectively, have been proposed to identify the flow patterns. Flow pattern maps that are used to give the transition boundaries of the flow patterns are then constructed based on the two criteria.

6.1 PDF Local Mode

When carefully studying the PDF figures of the void fraction signals for different flow patterns, we have found that uniform flow patterns, i.e., bubbly and annular flows, are characterized by a single peak PDF, whereas periodic flows, slug and churn flows, are characterized by a two peak PDF. Hence, the number of peaks in the PDF can be used to identify the two major types of the flow patterns: the uniform and the periodical flow patterns. We have also found that the single peak appears at low void fractions for bubbly flows and at high void fractions for annular flows. Therefore, the bubbly and the annular flows are further characterized by the location where the single PDF peak appears. Slug and churn flows can also be further identified by the location where the bigger peak appears. For slug flows, the bigger peak is located at a low void fraction side while the situation reverses for churn flows.

Judging from these observations, the "local mode" of the PDF is defined to quantitatively describe the characteristic features of PDFs. The first local mode, M_1, is defined as the PDF peak appearing at a low void fraction. The second local mode, M_2, corresponds to the PDF peak appearing at a high void fraction. The four typical flow patterns can be then characterized in terms of the "local mode" of the PDF. For bubbly flows, there is no peak at a high void fraction and the value of the second local mode, $M_2 = 0$. For annular flows, the first local mode, $M_1 = 0$. For slug flows, the first local mode is generally bigger then the second local mode, $M_1 > M_2$, since the length of the gas bubble is usually shorter than that of the aerated liquid slug. For churn flows, the gas bubble is elongated and distorted and this kind of flow pattern is

usually characterized by a bigger peak appearing at a high void fraction, as discussed above. Hence, $M_2 > M_1$. The features of the values of the local mode of the PDF allow different flow patterns to be identified.

6.2 PDF Flow Pattern Map

A flow pattern representation developed from the study of the local PDF modes is summarized in Table 6.1. PDF flow pattern map has been established on the basis of the local mode (see Figure 6.1). The x–axis represents the first local mode of PDF while the y–axis the second local mode of PDF. The points on the x–axis corresponds to bubbly flows ($y = M_2 = 0$) and the points on the y–axis represent annular flows ($x = M_1 = 0$). The slug and churn flows patterns are located on the two–dimensional plane. Slug flows are scattered on the lower diagonal half–plane ($M_1 > M_2$) and churn flows are on the upper diagonal half-plane of the map ($M_2 > M_1$). It must be pointed out that the points corresponding to the bubbly flows whose PDF's show a single peak followed by a tail were also regarded as single peak type and plotted on the x–axis, since no significant "bump" was observed at a high void fraction.

The PDF map permits a quantitative representation of flow pattern transition boundaries. However, further experimental work is still required to confirm these observations. For example, further study is required to determine if the 45° dashed line can be used as the transition from slug to churn flows.

Table 6.1: PDF study for flow pattern identification.

PDF feature	bubble flow	slug flow	churn flow	annular flow
modal type	unimodal	bimodal	bimodal	unimodal
mode	single	double	double	single
mode value	$M1 > 0$, $M2 = 0$	$M1 > M2$	$M1 < M2$	$M1 = 0$, $M2 > 0$
flow type	uniform	periodic	chaotic	uniform
map location	x-axis	lower plane	upper plane	y-axis

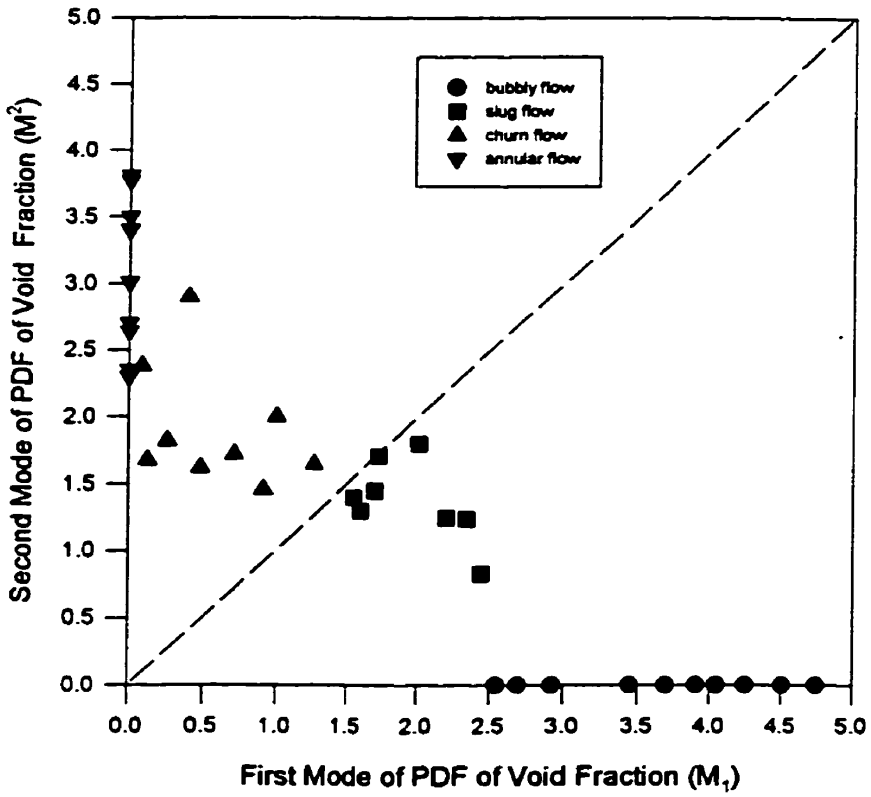

Figure 6.1: Flow pattern map from PDF.

6.3 Spectrum-Energy Ratio

When studying the figures of the PSDF in the signals of the void fraction and the pressure, we have found that the bubbly flows are characterized by a broadband spectrum over all the frequency range. The slug, churn and annular flows are characterized by a dominant peak spectrum. The dominant frequency component increases when the flow pattern changes sequentially from slug–to–churn–to–annular flows. Therefore, it is difficult to identify these three flow patterns based only on the spectrum. In other words, the information of the PSDF is not sufficient to identify the flow patterns. In such a case, the flow parameter that is called the "average energy dissipation rate" has been introduced to help to establish a quantitative PSDF criterion for flow pattern identification. The PSDF represents the statistical energy distribution over the flow frequency while the average energy dissipation rate represents the average fluid energy dissipated by the flow.

The term, spectrum–energy ratio, is then proposed to quantitatively describe the results of the analysis of the PSDFs for different flow patterns. An average energy dissipation rate as given in Lopes (1984) and Kocamustafaogullari *et al.*; (1993, 1994) and the normalized amplitude of each frequency component determined from differential pressure signals are used to define a spectrum–energy ratio given as:

$$\Psi_k = \frac{A_k}{\langle \epsilon \rangle}, \tag{6.1}$$

where, A_k represents the amplitude of the k^{th} frequency component and $\langle \epsilon \rangle$ represents

the average dissipation energy calculated by Kocamustafaogullari *et al.* (1993, 1994):

$$\langle \epsilon \rangle = \frac{J_g}{\rho_g} (\frac{\Delta p}{\Delta z})_{f,2p}, \tag{6.2}$$

with :

J_g: average superficial gas velocity (m/s)

$(\frac{\Delta p}{\Delta z})_{f,2p}$: two–phase frictional pressure gradient (Pa/m).

The average dissipation energy is a measure of fluid turbulence. The spectrum–energy ratio, Ψ_k, can be viewed as a relative energy parameter. It can be interpreted as the manner in which the spectrum fluctuating energy for a given frequency varies with the average fluid turbulent energy.

6.4 PSDF Flow Pattern Map

The new flow pattern representation, given by the spectrum–energy ratio in Equation 6.1 as a function of frequency components, is shown in Figure 6.2.

In practice, the values of the spectrum–energy ratio corresponding to the discrete frequency components are used for constructing the map. For bubbly flows, the spectrum is broadband over the frequency range and hence ten frequencies at equal intervals are chosen for the plot. For slug and churn flows, the dominant frequency and the several secondary frequencies are used. For annular flows, only the unique dominant frequency is considered.

In order to calculate the average energy dissipation rate, $\langle\epsilon\rangle$, the average superficial gas velocity is determined using the absolute pressure measured at a location close to the differential pressure taps in our study. The two–phase frictional pressure gradient is calculated using previous two–phase pressure drop measurements, i.e., two–phase friction multiplier, carried out under similar flow conditions in the same test section.

Since bubbly flows are characterized by a wide range of frequency components and small average energy dissipation rates, they are represented by the points plotted on the top of the flow pattern map. In turn, annular flows which are characterized by a single high frequency component and relatively large average energy dissipation rates, are confined to the bottom part of the map. In between these two regions data corresponding to slug and churn flow are plotted. The difficulty of differentiating slug from churn flows only based on their spectrum can be overcome when the term of the spectrum–energy ratio is applied to represent the flow patterns. The fact that the energy dissipation for the slug flows is smaller than that for the churn flows, makes it possible to identify these two flow patterns, as shown in Figure 6.2. Therefore, it can be expected that with the addition of more appropriate experiments and analysis, this kind of flow pattern representation could allow a better identification of flow pattern transitions to be carried out.

It is very interesting to find that the figures of the PSDF on the signals of the pressure are almost identical to those on the signals of the void fraction for all the flow patterns that have been studied. This observation is very important because it confirms that we can identify the flow patterns only using the measurement of the fluctuating signals of

the pressure. Once the frequency components of the pressure are determined from the two–phase flow, the spectrum–energy ratio can be determined and the flow patterns can be then identified from the PSDF flow pattern map.

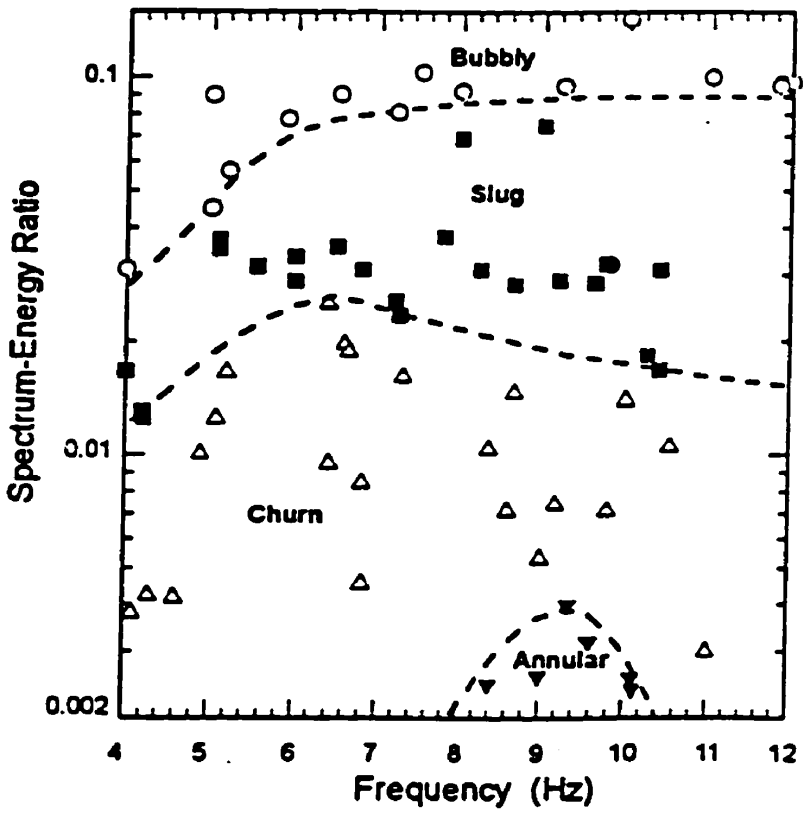

Figure 6.2: Flow pattern map from PSDF.

Conclusion

- The fluctuating component of the void fraction and differential pressure signals were measured and analyzed using PDF, statistical moments and PSDF techniques. In general it has been observed that the stochastic nature of the signals are strongly dependent on the flow patterns.

- A study of the statistical information obtained from both void and pressure signals validated the usefulness of the statistical identification technique presented in this work.

- The PSDF of both the void fraction and pressure signals are in excellent agreement for all the cases studied. It is feasible to identify the flow patterns on the basis of the pressure signals only.

- Furthermore, flow pattern identification using pressure signals is a promising technique. The appropriate selection of the pressure lines, the distance between the pressure taps and the pressure transducer permits the information on the flow structure to be easily obtained.

- Flow pattern maps are constructed based on quantitatively stochastic analyses from PDF and PSDF. The results show that this kind of approach allows a new

and clear flow pattern representation.

- It is possible to extend the application of the present technique to high pressure steam–water systems by using an appropriate pressure transducer.

Bibliography

AKAGAWA, K., HAMAGUCHI, H., SAKAGUCHI, T. & IKARI, T. (1971) "Studies on the fluctuation of pressure drop in two–phase slug flow." Bull. JSME. **14**, 447–469.

BAKER, O. (1954) "Simultaneous flow of oil and gas." Oil and Gas J. **53**, 185–195.

BARNEA, D. (1987) "A unified model for predicting flow pattern transitions for the whole range of pipe inclinations." Int. J. Multiphase Flow **13**, No.1, 1–12.

BARNEA, D. (1990) "Effect of bubble shape on pressure drop calculations in vertical slug flow." Int. J. Multiphase flow **16**, No. 1, 79–89.

BARNEA, D., LUNINSKI, Y. & TAITEL, Y. (1983) "Flow pattern in horizontal and vertical two–phase flow in small diameter pipes." The Canadian Journal of Chemical Engineering **61**, 617–620.

BARNEA, D. & TAITEL, Y. (1993) "Stability of seperated flow with applications to flow pattern transition." ASME., Heat transfer division **260**, 85–98.

BENDAT, J. S. & PIERSOL, A. G. (1986) "Random data, analysis and measurement procedures." John Wiley & Sons Inc., New York.

BENDAT, J. S. & PIERSOL, A. G. (1992) "Engineering applications of correlatin and spectral analysis." John Wiley & Sons Inc., New York.

BENNETT, A. W., HEWITT, G. F., KEARSEY, H. A., KEEYS, R. K. F. & LACEY, P. M. C. (1965) "Flow visualisatin studies of boiling at high pressure." UKAEA Report No.ERE–R4874. HMSO, London.

BRAUNER, N. & BARNEA, D. (1986) "Slug–to–churn transition in upward gas–liquid flow." Chem. Eng. Sci. **41**, No. 1, 159–163.

CHENG, H., HILLS, J. H. & AZZORPARDI, B. J. (1998) "A study of the bubble–to–slug transition in vertical gas–liquid flow in columns of different diameter." Int. J. Multiphase Flow **24**, 431–452.

COLLIER, J. G. (1981) "Convective boiling and condensation." McGraw–Hill Inc., New York.

COPPER, K. D., HEWITT, G. F. & PINCHIN, B. (1963) "Photography of two–phase flow." AERE–R4301.

COSTIGAN, G. & WHALLEY, P. B. (1997) "Slug flow regime identification from dynamic void fraction measurements in vertical air–water flows." Int. J. Multiphase Flow **23**, 263–282.

DAS, R.K. & PATTANAYAK, S. (1993) "Electrical impedance method for flow regime identification in vertical upward gas–liquid two–phase flow." Meas. Sci. Technol. **4**, 1457–1463.

DELHAYE, J. M., GIOT, M. & RIETHMULLER, M. L. (1981) "Thermohydraulics of two–phase systems for industrial design and nuclear engineering." Hemisphere Publishing Corporation.

DUKLER, A. E. & TAITEL, Y. (1977) "Flow regime transitions for upward gas liquid flow: a preliminary approach through physical modelling." Progress Report No. 1, NUREG—0162, NRC–2,4, University of Houston, Texas.

DUKLER, A. E. & TAITEL, Y. (1986) "Flow pattern transitions in gas–liquid systems: measurement and modelling." Multiphase Science and Technology **2**, Hemisphere, Washington DC.

ELKOW, K. J. & REZKALLAH, K. S. (1997) "Statistical analysis of void fluctuations in gas–liquid flows under 1 – g and m – g conditions using a capacitance sensor." Int. J. Multiphase Flow **23**, 831–844.

FULFORD, G. D. (1964) "The flow liquids in thin films." Advances in Chemical Engineering **5**, 151–236, Academic Press, New York.

GOVIER, G. W. & AZIZ, K. (1972) "The flow of complex mixtures in pipes." Van Nostrand Reinhold, New York.

GOVAN, A. H., HEWITT, G. F., RICHTER, H. J. & SCOTT, A. (1991) "Flooding and churn flow in vertical pipes." Int. J. Multiphase Flow **17**, No. 1, 27–44.

GRIFFITH, P. & WALLIS, G. B. (1961) "Two–phase slug flow." Trans. ASME, J. Heat transfer, **83**, 307–320.

HAN, Y. (1998) "Analysis of void and pressure signal fluctuations for two–phase flow pattern identification." Proceedings of 23rd CNA/CNS Annual Student Conference, 164–175

HEWITT, G. F. & ROBERTS, D. N. (1969) "Studies of two–phase flow patterns by simultaneous X–ray and flash photography." AERE–M 2159.

HEWITT, G. F. & JAYANTI, S. (1993) "To churn or not to churn." Int. J. Multiphase Flow **19**, No. 3, 527–529.

HASSAN, Y. A. & BLANCHAT, T. K. (1990) "A new heat transfer correlation and flow regime map for the tube bundles." Journal of Engineering for Gas Turbines and Power **112**, 150–156.

HINCE, J. O. (1955) "Fundamentals of the hydrodynamic mechanism of splitting in dispersion process." AIChE J. **1**, 289–295.

HUBBARD, M. G. & DUKLER, A. E. (1966) "The characterization of flow regimes for horizontal mechanics institute. Stanford Univ. Press, Standford, Calif.

JAIN, P. K. & ROY, R. P. (1983) "Stochastic characteristics of vapor fraction and pressure fluctuations in boiling flows." Int. J. Multiphase Flow **9**, 463–489.

JAYANTI, S. & HEWITT, G. F. (1992) "Prediction of the slug–to–churn flow transition in vertical two–phase flow." Int. J. Multiphase Flow **18**, No. 6, 847–860.

JONES Jr., O. C. & DELHAYE, J–M. (1976) "Transient and statistical measurement techniques for two–phase flows: a critical review." Int. J. Multiphase Flow **3**, 89–116.

JONES Jr., O. C. & Zuber, N. (1974) "Statistical methods for measurement and analysis in two–phase flow." Proceedings of the 5th International Heat Transfer Conference, Tokyo, IV–B5.4, 200–204.

JONES Jr., O. C. & Zuber, N. (1975) "The interrelation between void fraction fluctuations and flow patterns in two–phase flow." Int. J. Multiphase Flow **2**, 273–306.

KADAMBI, V. (1985) "Prediction of pressure drop and void–fraction in annular two–phase flow." Canadian J. of Chemical Engineering **63**, 728–734.

KING, C. H., OUYANG, M. S. & PEI, B. S. (1988) "Identification of two–phase flow regimes by an optimum modeling method." Nuclear Technology **82**, 211–226.

KOZMA, R., DAM, H. & HOOGENBOOM, J. E. (1992) "Identification of flow patterns by neutron noise analysis during actual coolant boiling in thin rectangular channels." Nucl. Technology **100**, 97–109.

LANGFORD, H. M., BEASLEY, D. E. & OCHTERBECK, J. M. (1998) "Observations on chaos in upward gas–liquid flow." HTD–Vol. 361–5, Proceedings of the ASME Heat Transfer Division, **5**.

LIN, P. Y. & HANRATTY, T. J. (1987) "Detection of slug flow from pressure measurements." Int. J. Multiphase Flow **13**, No. 1, 13–21.

LUBBESMEYER, D. & LEONI, B. (1983) "Fluid–velocity measurements and flow–pattern identification by noise–analysis of light–beam signals." Int. J. Multiphase flow **9**, 665–679.

MANDHANE, J. M., GREGORY, G. A., AZIZ, K. (1974) "A flow pattern map for gas–liquid flow in horizontal pipes." Int. J. Multiphase **1**, 537–553.

MATSUI, G. (1984) "Identification of flow regimes in vertical gas–liquid two–phase flow using differential pressure fluctuations." Int. J. Multiphase Flow **2**, 711–720.

MATSUI, G. (1986) "Automatic identification of flow regimes in vertical two–phase flow using differential pressure fluctuations. "Nuclear Engineering and Design **95**, 221–231.

MAO, Z. S. & DUKLER, A. E. (1993) "The myth of churn flow." Int. J. Multiphase flow **19**, No. 2, 377–383.

MATUSZKIWICZ, A., FLAMAND, J. C. & BOURE, J. A. (1987) "The bubble–slug flow pattern transition and instabilities of void fraction waves." Int. J. Multiphase Flow **13**, No. 2, 199–217.

MCQUILLAN, K. W. & WHALLEY, P. B. (1985) "Flow patterns in vertical two–phase flow." Int. J. Multiphase Flow **11**, No. 2, 161–175.

MINAMI, K. & SHOHAM, O. (1994) "Transient two–phase flow behavior in pipelines, Experiment and Modelling." Int. J. Multiphase Flow **20**, No. 4, 739–752.

MISHIMA, K, & ISHII, M. (1984) "Flow regime transition criteria for upward two–phase flow in vertical tubes." Int. J. Multiphase Flow **27**, No. 5, 723–737.

NISHIKAWA, K., SEKOGUCHI, K. & FUKANO, T. (1969) "On the pulsation phenomena in gas–liquid two–phase flow." Bull. JSME. **12**, 1410–1416.

OSHINOWO, T. & CHARLES, M. E. (1974) "Vertical two–phase Flow: Part 2, Holdup and pressure drop." Canadian J. of Chemical Engineering **52**, 438–448.

OWEN, D. J. (1986) "An experimental and theoretical analysis of equilibrium annular flow." Ph.D. Thesis, Univ. of Birmingham, Birmingham, U.K.

ROUHANI, S. Z. & SOHAL, M. S. (1983) "Two–phase flow patterns: a review of research results." Progress in Nuclear Energy **11**, No. 3, 219–259.

SEKOGUCHI, K., INOUE, K. & IMASAKA, T. (1987) "Void signals analysis and gas–liquid two–phase flow regime determination by a statistical pattern recognition method." JSME Int. J. **30**, 1226–1273.

SEVIC, M. & PARK, S. H. (1973) "The splitting of drops and bubbles by turbulent fluid flow." Trans. ASME, J. Fluid Engng. **95**, 53–60.

SHOHAM, O. (1982) "Flow pattern transitions and characterizations in gas–liquid two–phase flow in inclined pipes." Ph.D. Thesis, Tel–Aviv University.

SPENDING, P. L. & SPENCE, D. R. (1993) "Flow regimes in two–phase gas–liquid flow." Int. J. Multiphase Flow **19**, No. 2, 245–280.

TAITEL, Y., BORNEA, D. & DUKLER, A. E. (1980) "Modelling flow pattern transitions for steady upward gas–liquid flow in vertical tubes." AIChE J. **26**, 345–354.

TEYSSEDOU, A. & HAN, Y. (1998) "Two–phase flow pattern identification from fluctuating components of pressure and void fraction signals." HTD–Vol. 361–5, Proceedings of the ASME Heat Transfer Division, **5**, 267–274

TUTU, N. K. (1982) "Pressure fluctuations and flow pattern recognition in vertical two phase gas–liquid flows." Int. J. Multiphase Flow **8**, 443–447.

TUTU, N. K. (1984) "Pressure drop fluctuations and bubble–slug transitions in a vertical air–water flow." Int. J. Multiphase Flow **10**, 211–216.

VINCE, M. A. & LAHEY Jr., R. T. (1982) "On the development of an objective flow regime indicator." Int. J. Multiphase Flow **8**, 93–124.

WALLIS, G. B. (1961) "Flooding velocities for air and water in vertical tubes." UKAEA Report No. AEEW–R123. HMSO, London.

WALLIS, G. B. (1969) "One–dimensional Two–phase Flow." McGraw–Hill Inc., New York.

WANG, Y. W., KING, C. H. & PEI, B. S. (1988) "Identification of two–phase flow patterns by a single void fraction sensor." Nuclear Technology **83**, Oct. 56–63.

WANG, Y. W., PEI, B. S. & KING C. H. (1990) "Identification of two–phase flow patterns in a nuclear reactor by high–frequency contribution fraction." Nuclear Technology **89**, 217–226.

WEISMAN, J., DUNDAN, D., GIBSON, J. & GRAWFORD, T. (1979) "Effects of fluid properties and pipe diameter on two–phase flow patterns in horizontal lines." Int. J. Multiphase Flow **7**, 271–291.

WEISMAN, J. & KANG, S. Y. (1981) "Flow pattern transitions in vertical and upwardly inclined lines." Int. J. Multiphase Flow, 271–291.

Appendix

Data Acquisition Connections and Conversion Ratios

A step in programming the data acquisition is to make sure that the analog channel of the data acquisition system is related to the desirable measuring channel. Table 6.2 shows the relationship between the analog channels for data acquisition system and the real measuring channels for void fraction, liquid flowrate and pressure signals. It is mentioned here that the information of the relationship for channel B is also provided in the convenience of possible future sub-channel experiments. Channel B, located beside the channel A, is the test channel with the same geometry as the one we used for the present work.

The data acquisition system is also calibrated by checking the difference between a known reference input and the actual system output. This difference, represented in the form of conversion ratios, are then taken into account in the data acquisition program as correction factors for each channel. Thus, if x_a is an arbitrary value read

from data acquisition system, the corresponding corrected value, x, is obtained by:

$$x = kx_a + b,$$

where, k and b represent the conversion and offset factors, respectively. They are determined using a reference voltage and a short circuit as input to each channel. The value of k of the void gauges is around two, because the data acquisition system saturates at $10 Volts$ and a voltage divider is introduced with a low pass filter in between the void meter and the data acquisition system. The values of k and b are summarized in Table 6.4 to Table 6.6.

Table 6.2: Connection to data acquisition system (Channel A).

Electrode #	AUBURN channel	Analog channel	Slot
A1	1	0	1
A2	2	2	1
A3	3	4	1
A4	4	6	1
A5	5	8	1
A6	6	10	1
A7	7	12	1
A8	8	14	1
A9	9	0	3
A10	10	2	3
A11	11	4	3
A12	12	6	3

Table 6.3: Connection to data acquisition system (Channel B).

Electrode #	AUBURN channel	Analogical channel	Slot
B1	1	1	1
B2	2	3	1
B3	3	5	1
B4	4	7	1
B5	5	9	1
B6	6	11	1
B7	7	13	1
B8	8	15	1
B9	9	1	3
B10	10	3	3
B11	11	5	3
B12	12	7	3

Table 6.4: Conversion ratio of void gauges (Channel A).

Electrode #	Input (Volts)	Reading (Volts)	Input (Volts)	Reading (Volts)	Conversion Factor (k)	Offset Factor (b)
A1	0	0.0024	10.004	4.985	2.007065	-0.00482
A2	0	0.0024	10.004	4.976	2.010696	-0.00483
A3	0	0.0024	10.004	4.980	2.009081	-0.00482
A4	0	0.0024	10.004	5.015	1.995052	-0.00479
A5	0	0.0024	10.004	4.996	2.002683	-0.00481
A6	0	0.0024	10.004	4.972	2.012355	-0.00483
A7	0	0.0024	10.004	4.984	2.007508	-0.00482
A8	0	0.0024	10.004	4.979	2.009484	-0.00482
A9	0	0.0024	10.004	5.038	1.985940	-0.00477
A10	0	0.0024	10.004	4.965	2.015153	-0.00484
A11	0	0.0024	10.004	4.965	2.015153	-0.00484
A12	0	0.0024	10.004	4.999	2.001441	-0.00480

Table 6.5: Conversion ratio of void gauges (Channel B).

Electrode #	Input (Volts)	Reading (Volts)	Input (Volts)	Reading (Volts)	Conversion Factor (k)	Offset Factor (b)
A1	0	0.0024	10.004	5.028	1.989892	-0.00478
A2	0	0.0024	10.004	4.999	2.001441	-0.00480
A3	0	0.0024	10.004	5.013	1.995849	-0.00479
A4	0	0.0024	10.004	5.035	1.987163	-0.00477
A5	0	0.0024	10.004	4.999	2.001481	-0.00480
A6	0	0.0024	10.004	4.999	2.001481	-0.00480
A7	0	0.0024	10.004	4.999	2.001481	-0.00480
A8	0	0.0024	10.004	4.999	2.001481	-0.00480
A9	0	0.0024	10.004	4.974	2.011505	-0.00483
A10	0	0.0024	10.004	4.964	2.015559	-0.00484
A11	0	0.0024	10.004	4.999	2.001441	-0.00480
A12	0	0.0024	10.004	5.007	1.998242	-0.00480

Table 6.6: Conversion ratio of pressure transducers.

Pressure Transducer #	Input (Volts)	Reading (Volts)	Input (Volts)	Reading (Volts)	Conversion Factor (k)	Offset Factor (b)
c1	0	0.0024	4.9987	4.9988	1.00046	-0.0024
c2	0	0.0024	4.9990	4.9988	1.00052	-0.0024
c3	0	0.0024	4.9988	4.9988	1.00048	-0.0024
c4	0	0.0024	4.9823	4.9841	1.00012	-0.0024